Master of Science Thesis

# Application of Uncertainty Quantification to a Fluid-Structure Interaction Experiment

## Providing Accurate Insight in Uncertain Phenomena

**Dirk Jan Boon**

9 December 2011

Faculty of Aerospace Engineering · Delft University of Technology

# Application of Uncertainty Quantification to a Fluid-Structure Interaction Experiment

## Providing Accurate Insight in Uncertain Phenomena

Master of Science Thesis

For obtaining the degree of Master of Science in Aerospace Engineering at Delft University of Technology

Dirk Jan Boon

9 December 2011

Faculty of Aerospace Engineering · Delft University of Technology

Delft University of Technology

Delft University Of Technology
Department Of
Aerodynamics

The undersigned hereby certify that they have read and recommend to the Faculty of Aerospace Engineering for acceptance a thesis entitled **"Application of Uncertainty Quantification to a Fluid-Structure Interaction Experiment"** by **Dirk Jan Boon** in partial fulfillment of the requirements for the degree of **Master of Science**.

Dated: 9 December 2011

Head of department: _____
prof.dr.ir.drs. H. Bijl

Supervisor: _____
dr. R.P. Dwight

Reader: _____
ir. J.J.H.M Sterenborg

Reader: _____
dr.ir. A.H. van Zuijlen

Reader: _____
dr. R.G. Hanea

# Summary

Societies demand for sustainability is one of the main drivers for innovation in the wind energy industry. The increasing size of wind turbines implies increasingly flexible turbine blades. The flexibility of the blades induces the occurrence of fluid-structure interaction (FSI) phenomena. The simulation codes that are used for the design of wind turbines need to be validated with observational data. In the current research a FSI experiment of a wing equipped with a trailing edge flap is performed to provide validation data. Little data is available in literature of free motion FSI experiments. Therefore, a FSI experiment is performed with a freely moving wing equipped with a trailing edge flap.

The FSI experiment consists of two parts, one part is meant to provide the steady characteristics of the experimental setup and the other comprises the unsteady FSI measurements. Uncertainty quantification is applied to the steady part of the experiment to obtain uncertainty characteristics. Input uncertainty estimates are obtained from observational data or expert knowledge. The uncertain wing geometry is investigated by performing measurements and constructing a three-dimensional wing model. The three-dimensional wing geometry is parameterized using a free-form deformation tool. Sensitivity analysis is applied to the uncertain input variables and geometric parameters to obtain the influence on the lift and moment coefficient and the relative importance of the parameters.

An uncertainty analysis is performed by propagating the input uncertainties of the most important parameters through a computer model. The computer model is made up of a probabilistic collocation response surface of panel method simulations and a kriging surrogate of vortex lattice method simulations. Uncertainty characteristics are obtained for the lift and moment coefficient on the experimental input data points. Combining the uncertainty characteristics with the observational data provides useful input for the validation of computer codes.

Using the experimental observations uncertain or unknown inputs are estimated using Bayesian calibration. The calibration estimates yield the best fit of the simulation data to the observational data, given the quantified uncertainties. The calibration estimates are used to make predictions of drag coefficient data. A comparison is made between the calibrated drag coefficient predictions and experimental drag measurements.

# Acknowledgements

This thesis describes the results of my graduation project. The graduation project is the final step towards obtaining the master's degree in Aerospace Engineering. I spent the last year of my studies to perform and complete the project. Here I would like to thank the people that supported me to perform the tasks related to my project.

First of all I would like to thank Richard Dwight for his inspiring support. Without his enthusiastic guidance this thesis would not have been what it is now. I appreciated very much his never ending willingness to help and the interesting discussions we had about complex problems.

Furthermore I would like to thank Joost Sterenborg. He continuously made me aware of the importance of punctuality and thoroughness in science, and especially when performing experiments. He has proven to stay interested even when my research deviated from his field of experience and he provided very useful feedback on my work.

I will never forget the meetings I had with Hester Bijl. She often came up with useful ideas and provided perspectives on the research I had not thought off, for which I am very grateful. I would like to thank Sander van Zuijlen for the support he gave me using his extensive knowledge of simulations of fluid-structure interaction phenomena.

I would like to express my gratitude towards Nico, Erik and Frits that supported my work as the technical staff, and towards the fellow students in the basement for the chats and having lunch together. Finally I would like to thank Jerke for his enthusiasm to play either ping-pong or the organs of the Oude Kerk in Delft together and for the conversations we had.

Delft, The Netherlands — Dirk Jan Boon
9 December 2011

# Contents

# List of Figures

# List of Tables

# Chapter 1

# Introduction

The demand for sustainability has focused the attention of energy suppliers on renewable energy sources. Wind energy is a promising source of renewable energy. Wind energy is transformed into electrical power by wind turbines. Innovation in the field of wind energy is the main driver to come up with increasingly efficient, large and low weight wind turbine designs. Increasing flexibility of the wind turbine blades merges together with the increase in size. Flexible wind turbine blades give rise to the phenomenon of fluid-structure interaction (FSI).

## 1.1 Literature Review

Prior to this thesis a literature review is performed to investigate available research results in literature and reported by Boon [2011]. The literature review was focused on fluid-structure interaction experiments and uncertainty quantification analyses.

Numerous FSI experiments are reported in literature that study forced moving structure in a fluid. Pitching as well as plunging airfoil cases has been studied to understand the interaction phenomena and wake dynamics. However, not many experiments are reported that study freely moving structures, especially not with rigid wings. This underlines the need for a free motion experiment to understand the aerodynamics of freely moving wings.

Uncertainty quantification analyses have been applied in many fields of science, especially the sciences related to engineering. Uncertainties are generally studied using computer codes that simulate reality. For aerodynamic problem computational fluid dynamics (CFD) codes are often employed. Various uncertainty quantification methods have emerged to study uncertain phenomena by making use of simulation codes. Monte Carlo methods provide a simple and straightforward approach to uncertainty analysis. The use of Monte Carlo methods however is limited in aerodynamic applications due to the large amount of required code evaluations to obtain uncertainty characteristics.

An efficient approach to uncertainty analysis is provided by the probabilistic collocation (PC) method since it requires relatively few code evaluations. The probabilistic colloca-

tion method has been used in conjunction with CFD codes to study uncertain aerodynamic problems. Loeven [2010] has used PC to study uncertainties in aerodynamic characteristics due to uncertain geometries and uncertain flow quantities. Furthermore, the method is applied to transonic flows about airfoils by Chassaing & Lucor [2010].

Wikle & Berliner [2006] discuss another promising technique for uncertainty quantification, which is called kriging. Using kriging a surrogate can be constructed from outputs of an expensive simulation code. Uncertainty analyses are performed using Monte Carlo integration on the kriging surface. Furthermore, kriging has been incorporated in Bayesian inference techniques by Kennedy & O'Hagan [2001a]. They describe a Bayesian calibration approach to estimate unknown or uncertain parameters. Bayesian calibration provides parameter estimates that yield the best fit of simulation data to observational data, given an error structure.

Wang et al. [2009] provide a method for the validation of computer codes with respect to observational data. This method is also based on the construction of kriging surrogates. A code can be said to comply with experimental observations if the outputs are within confidence bounds that are obtained by the validation method.

## 1.2 Fluid-Structure Interaction Experiment

For the design of wind turbines computer simulation codes are extensively used. Advances in computer technology have made it possible to simulate aerodynamic systems increasingly accurately. Several computer codes have become available for the simulation of fluid-structure interaction systems. However, not many different experiments have been performed for the validation of these codes. Hardly any reports are available in literature of especially fluid-structure interaction experiments with freely moving structures. Therefore in the current research a fluid-structure interaction experiment with a freely moving structure is performed to provide validation data for simulation codes. Prior to the fluid-structure interaction experiment steady measurements are performed to obtain the characteristics of the system.

The experiment is performed using a three-dimensional wing equipped with a trailing edge flap. The trailing edge flap is deflected using servo engines that are located inside the wing. The deflecting flap induces the free motion of the wing structure. Chapter 2 provides a description of the experiment and a discussion of the results.

## 1.3 Uncertainty Quantification

Experiments are subject to statistical and systematic uncertainties. Statistical uncertainties are unknowns that differ each time the same experiment is run. Systematic uncertainties are caused by unknown sources that could be known in principle but are unknown in practice. Both types of uncertainties induce uncertainties in the experimental observations. Quantification of the uncertainties is required for the validation of computer codes with the experimental observations. The main aim of this thesis is described as follows:

> Obtain uncertainty characteristics of the experimental observations and investigate the sources of uncertainty using uncertainty quantification techniques.

Uncertainty quantification is the science of quantitative characterization and reduction of uncertainties. It provides information about how likely certain outcomes are if some aspects of the process are unknown or uncertain. Uncertainty quantification is applied to the current experiment by regarding parametric uncertainties, which are believed to be the main cause of the output uncertainties. In this first work uncertainty quantification is only applied to the steady measurements of the lift and moment. Inferences can be made on the uncertainty characteristics of the steady measurements to provide information for the fluid-structure interaction experiment.

The experimental uncertainties are studied by making use of computer simulation modeling. Two simulation codes are employed that are able to model the influence of the important inputs of the experiment and are cheap to run. Chapter 3 describes the simulation codes and the corrections applied to the simulation outcomes in order to compare them with the experimental observations.

A useful framework for uncertainty analysis is provided by Bayesian statistics. Chapter 4 elaborates on the principles of Bayesian statistics and describes a classification of the sources of uncertainties. Furthermore, mathematical methods are discussed that are used in uncertainty quantification.

The input uncertainties present in the experiment are divided into two groups, the geometric uncertainties and the experimental input uncertainties. The geometric uncertainties correspond to the three-dimensional wing geometry. The wing geometry is uncertain due to bad manufacturing standards. In order to obtain information about the uncertain wing geometry measurements are performed, see chapter 5. A three-dimensional model is obtained from the measurements of the wing geometry, which is still subject to uncertainties. The model of the uncertain wing geometry is parameterized using a free-form deformation tool, see chapter 6. Sensitivity analysis is applied to the parameterized geometry to obtain the sensitivity of the lift coefficient to geometric variations.

The second group of uncertainties are termed experimental input uncertainties. This group refers to all experimental input parameters except the wing geometry. The angle of attack and the flap angle are included in this group as well. Chapter 7 provides a characterization of the experimental input uncertainties. Estimates of the input uncertainties are obtained by using data or expert knowledge or both. A sensitivity analysis is performed on the input parameters to obtain their relative influence on the lift coefficient.

Having obtained the characteristics of the input uncertainties the output uncertainties are quantified by propagation of the input uncertainties through a computer model, as discussed in chapter 8. The uncertainty quantification results are compared with the observational data.

In chapter 9 the most important unknown or uncertain input parameters are estimated using a Bayesian inference technique called calibration. Calibration refers to estimating unknown or uncertain parameters that provide the best fit of simulations to observations. Having obtained the estimates for the unknown parameters predictions are performed for the drag coefficient, which is absent in the experimental results.

Finally conclusions and recommendations for future work are given in chapter 10.

# Chapter 2

# Wind Tunnel Experiment

Fluid-structure interaction phenomena play an important role in the design of wind turbines. The design of wind turbines is mainly performed employing Computational Fluid Dynamics (CFD) simulations. Experimental observations are required to validate the CFD codes. In this thesis a Fluid-Structure Interaction (FSI) experiment is reported, which is performed to provide validation data for simulation codes. Using uncertainty quantification methods the experimental errors are assessed and investigations are performed to increase understanding about the causes of uncertainty. Furthermore, information about the uncertainty characteristics of the observations is required to validate computer codes with the experimental results.

This chapter presents a description of the experiment and a discussion of the results of the steady part of the experiment. Section 2.1 describes the setup and conditions of the FSI wind tunnel experiment. As described in section 2.2, a steady case is performed prior to the actual FSI case to obtain the steady aerodynamic characteristics of the setup. Both the steady and the FSI case are described in this section. Because in this thesis uncertainty quantification is only applied to the steady case, only the results of this case are presented, see section 2.3.

## 2.1 Experimental Apparatus and Conditions

The experiment is performed in an open wind tunnel, termed the Open Jet Facility (OJF). The OJF and its operating conditions during the experiment are described in section 2.1.1. Section 2.1.2 describes the experimental setup. Measurements are performed using various measurement equipment, as discussed in section 2.1.3.

### 2.1.1 Open Jet Facility

The Open Jet Facility is an atmospheric low speed wind tunnel with an open jet entering the test section. A large fan powered by a 500 kilowatt electric engine is able to achieve

a maximum free stream velocity in the test section of about 35 meters per second. The air is rotated 180 degrees around the corners through a long diffuser and two rows of corner vanes. After passing a short diffuser the air enters the settling chamber. Here the turbulence and velocity fluctuations in the airflow are reduced by five fine-mesh screens. Via a contraction the air is blown into the test section through an open jet tunnel exit. At the end of the test section the air is cooled by an enormous cooling radiator. After being cooled the air passes corner vanes and is thereby guided back to the fan. A schematic representation of the wind tunnel is shown in Figure 2.1.

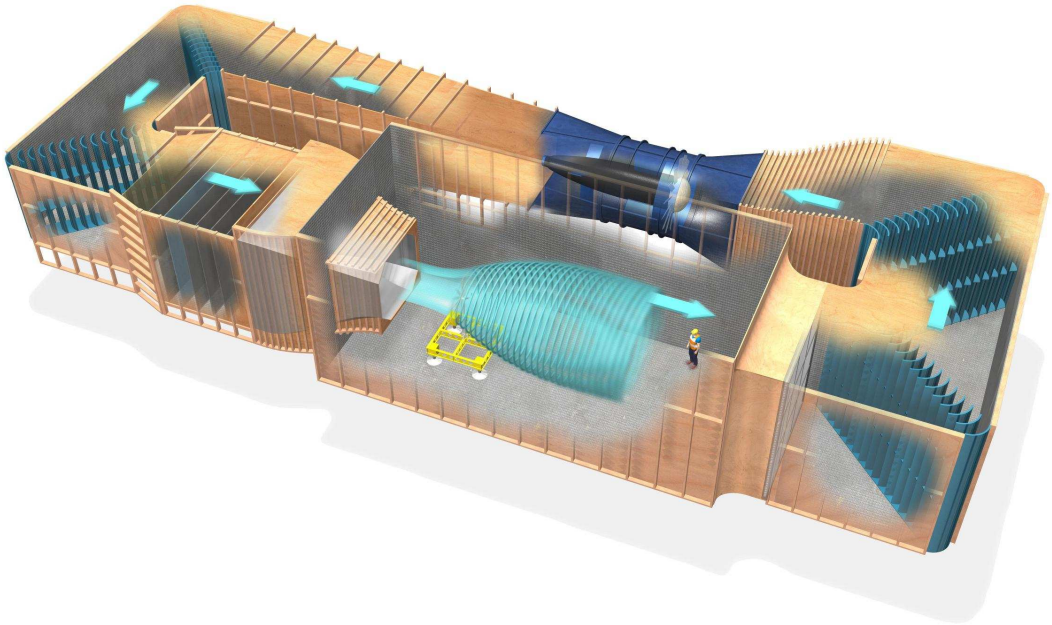

**Figure 2.1:** Schematic representation of the Open Jet Facility and the air flow.

The octagonally shaped tunnel exit has a width of 2.85 meters and a height of 2.85 meters. The wind tunnel test models are placed behind the tunnel exit in the large test section of 13 meters width and 8 meters height. The large dimensions of the test section enable to test large scale models that are used for example for wind energy research. The tunnel operates under atmospheric conditions. This experiment is performed at a free stream velocity of 21 m/s. The wind tunnel operating conditions are summarized in Table 2.1.

### 2.1.2 Wind Tunnel Test Model

The test model consists of a wing suspended to a structure and placed on a measurement table in the wind tunnel test section, see Figure 2.2. The wing characteristics are summarized in Table 2.2. The wing geometry is based on the DU 96-W-180 airfoil (or

| | mean | standard deviation |
|---|---|---|
| Free stream velocity $V$ [m/s] | 21.0 | 0.05 |
| pressure $p$ [hPa] | 1006.5 | 6.7 |
| temperature $T$ [°C] | 19.2 | 1.95 |
| density $\rho$ [kg/m$^3$] | 1.206 | 0.066 |
| kinematic viscosity $\nu$ [m$^2$/s] | $1.50 \cdot 10^{-5}$ | $4.6 \cdot 10^{-7}$ |
| Reynolds number Re [-] | $7.0 \cdot 10^5$ | $5.9 \cdot 10^4$ |
| Mach number Ma [-] | 0.06 | $1.6 \cdot 10^{-4}$ |

**Table 2.1:** Wind tunnel operating conditions during the experiment.

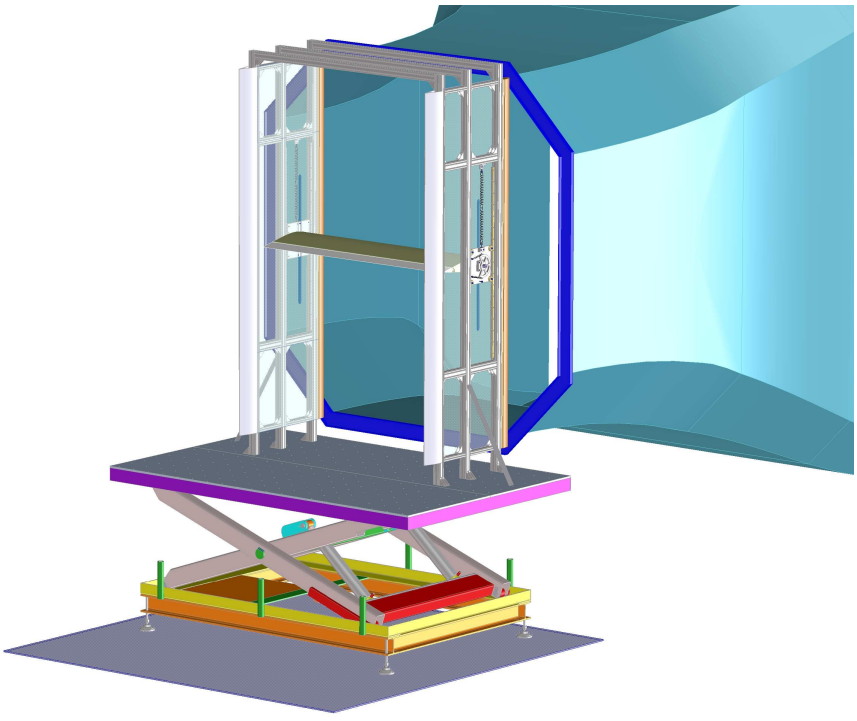

**Figure 2.2:** Sketch of the wind tunnel setup showing the tunnel exit with the structure placed on the measurement table behind the tunnel exit.

DU96W180 in short), which is designed at the Delft University of Technology as a wind turbine profile. The wing span $b$ is 1.8 m, the chord length $c$ is 0.5 m and the maximum thickness is 18% of the chord length. The wing is equipped with a trailing edge flap of 20% chord length, which is hinged at the pressure side of the wing. The flap is actuated by two servo engines, which are located inside the wing. The servo engines are controlled by putting them under a specific voltage. The wing is assumed to be rigid. The geometric deformations, being introduced by flap deflections, induce free vertical motion. Note that the internally located servo engines are the only forcing actuators; no external forcing is applied to the wing. Tripping wires are applied at $5\%c$ on the pressure side and $2\%c$ on the suction side measured from the leading edge to advance boundary layer transition. Because the effectiveness of the tripping wires has not been assessed for the current experiment, no exact data is available for the transition location.

| | |
|---|---|
| airfoil | DU 96-W-180 |
| chord $c$ | 0.5 m |
| maximum thickness | $18\%c$ |
| span $b$ | 1.8 m |
| material | carbon composite |
| high lift device | $20\%c$ TE flap |
| tripping wire thickness | 0.48 mm |

**Table 2.2:** Characteristics of the DU 96-W-180 airfoil.

The aerodynamic characteristics of the DU 96-W-180 profile are shown in Figure 2.3. These characteristics are obtained from a two-dimensional experiment, which is performed outside the context of this thesis. The maximum lift coefficient $c_{l_{max}}$ amounts to approximately 1.25 and occurs at a critical angle of attack $\alpha_{cr}$ around 10 degrees. The drop in lift and the increase of drag for $\alpha$ larger than $\alpha_{cr}$ indicate the stall region of the airfoil.

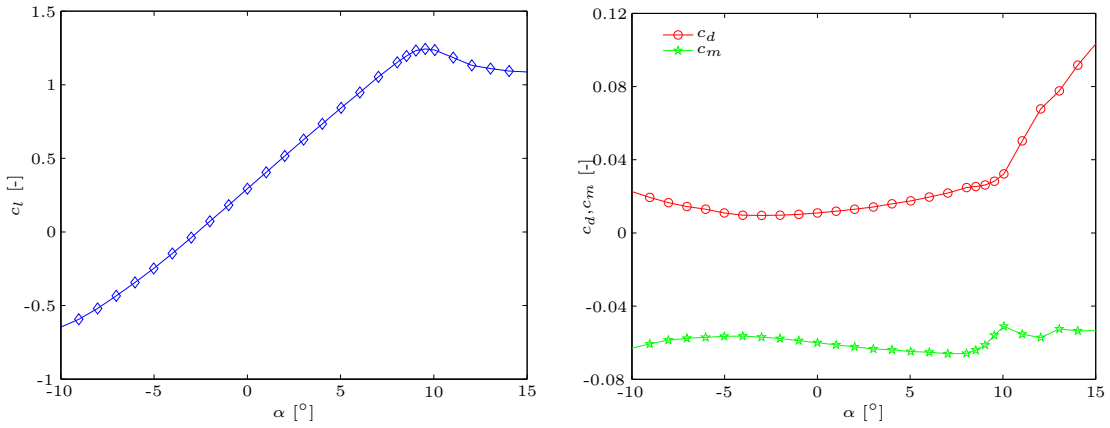


(a) Lift coefficient.

(b) Drag and moment coefficient.

**Figure 2.3:** Aerodynamic characteristics of the DU 96-W-180 airfoil ($\mathrm{Re} = 7 \cdot 10^5$).

A structure has been manufactured to support the wing and enable vertical motion. Figure 2.2 shows that the supporting structure consists of side walls and top beams, which are meant for structural stiffness. Each side wall structure is made into an aerodynami-

cally smooth shape by using a wooden leading edge shape, shielding plates at both sides and an aluminum trailing edge. The wing is attached via shafts to plates that are able to slide vertically inside the side wall structure, as shown in Figure 2.4a. The attaching shaft sticks through one of the side plates in a slit of 3 centimeter. Using rods the vertical motion can be constrained for the steady part of the experiment. The height of the wing above the measurement platform amounts to 1.75 m for the steady part. During the unsteady part of the experiment the sliding plates are suspended to the structure using springs to enable vertical motion of the wing. Figure 2.4b shows the connection of the rods and the springs to the sliding plate. In between the wing and the side walls a gap is present of approximately 4 mm.

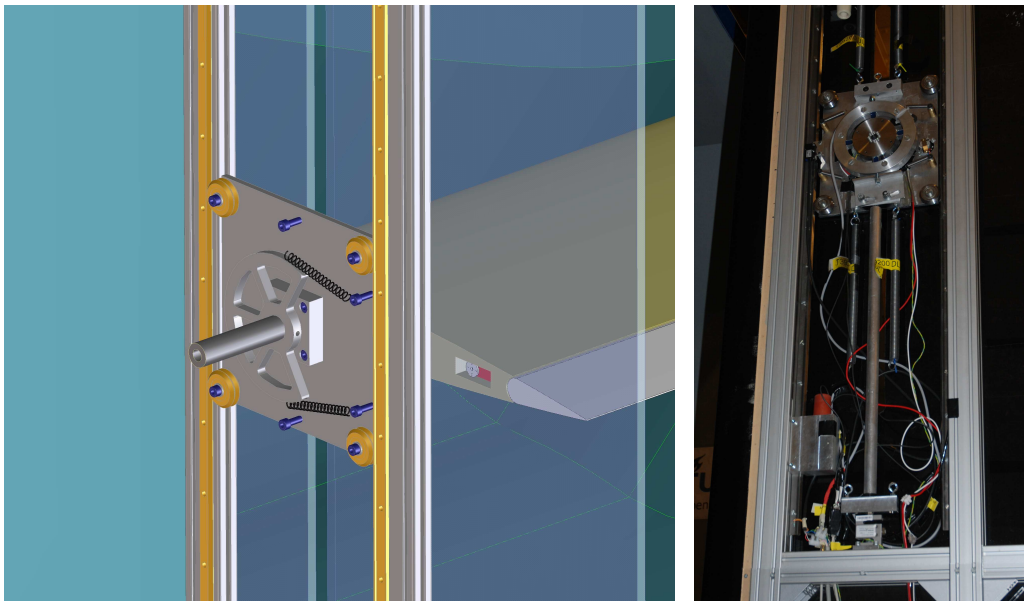

(a) Sketched detail of the attachment of the wing shaft to the sliding plate.

(b) Detailed picture of the sliding plate with the rod and spring attachments.

**Figure 2.4:** Attachment of the wing shaft to the sliding plates including the rod and spring connection between the load cells and the sliding plate.

### 2.1.3 Measurement Equipment

During the experiment various sensors measure the wind tunnel conditions, the attitude of the wing and the forces acting on the wing. In addition, flow field measurements are performed using Particle Image Velocimetry (PIV).

#### Measurement Sensors

The physical quantities related to the wind tunnel conditions, such as the pressure and the free stream velocity, are measured by sensors, which are installed in the wind tunnel.

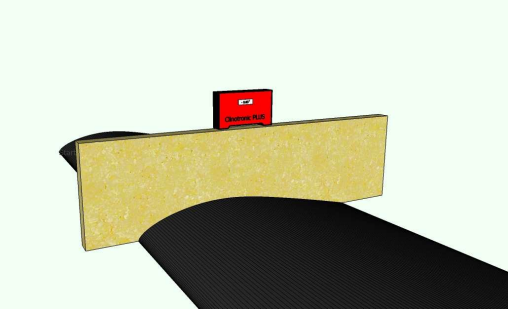

**Figure 2.5:** Measurement of the angle of attack by a Clinotronic PLUS measurement device using a wooden mold.

The main variables of the measurement setup are the angle of attack and flap angle. For the angle of attack the upward direction is defined as positive and for the flap angle the downward direction is defined as positive. The angle of attack is set manually by making use of a wooden mold that is made based on measurements of the geometry, see Figure 2.5. The measurements are performed using a coordinate measuring machine, as discussed in section 5.1. The angle is measured by a Clinotronic PLUS measurement device, which has an maximum error of 0.03 degrees. The flap angle control mechanism is calibrated using a little mold and the Clinotronic PLUS measurement device. The little mold was manufactured using the big mold as a reference. Once the flap angle calibration is performed the servo engines control inputs are determined.

The aerodynamic characteristics and attitude variables are measured using various sensors, as shown in Table 2.3. The lift force acting on the wing is measured by two types of sensors yielding redundant measurements. The aerodynamic forces acting on the wing are transferred to the load cells via either the connecting springs or the rods, depending on the experimental case. Furthermore, strain gauges are installed on the wing shafts to measure the lift and drag. The aerodynamic moment is measured using torque sensors that are attached to the wing shafts. The torque sensors are of type TS170 having an uncertainty of 0.2 Nm.

Prior to performing the experiment the angle sensors and the strain gages are calibrated. The load cells and the torque sensors are calibrated by the supplier prior to delivery and checked when setting up the experiment. For the strain gauges no error specifications are available. The strain gauge measurement error depends not only on the strain gauge itself, but also to the bond with the underlying material and the direction in which it is placed. Based on these considerations the strain gauge outputs are believed to be subject to severe measurement errors. Therefore, the strain gauge measurements will not be presented in this chapter.

The output of the sensors, except the wind tunnel sensors, is continuously logged at a rate of 2 kHz by the National Instruments program Labview. The servo engines are also controlled via Labview.

### Particle Image Velocimetry Equipment

A particle image velocimetry (PIV) measurement campaign is carried out to obtain a velocity vector field of the flow about the wing at mid span.

Using a fog generator smoke is released in the flow. The smoke is illuminated by a laser that produces a thin laser sheet at mid span. A camera takes pictures of the illuminated smoke particles that are in the thin laser sheet at mid span of the wing. At each instant

| | Supplier | type | measured quantity | maximum error |
|---|---|---|---|---|
| load cells | Feteris components BV | FLB3G | lift | 0.2 N |
| torque sensors | ME Meßsysteme GmbH | TS170 | 0.2 Nm | |
| strain gauges | HBM | 1-LY41-6/350A | lift, drag | n/a |
| potentiometers | Feteris components BV | LNB22 | angle of attack, flap angle | 0.1° |
| magnetic transducer | Feteris components BV | TM+MP200 | vertical wing position | 0.1 mm |

**Table 2.3:** Specifications of measurement equipment.

two pictures are taken separated in time with a very short interval. The traveled distance of particles in two subsequently taken pictures is determined by correlation functions. The traveled distance of the particles and the time interval are used to compute velocity vectors in the flow field.

Since the dimensions of the wing are relatively large for PIV measurements the entire area of interest is divided into 8 fields of view. In order to reduce experiment running time two cameras are employed taking pictures simultaneously. An overlap is present between the pictures of both cameras and between each field of view. The overlap is required to relate the various fields of view to each other and obtain a velocity vector field in the area of interest without gaps.

## 2.2 Experimental Test Cases

The current research experiment is a free motion fluid-structure interaction experiment. The full experiment is broken down into two test cases. In order to obtain the aerodynamic characteristics of the experimental setup, initially steady experiments for a range of angle of attack and flap angle are performed, as discussed in section 2.2.1. After having performed the steady measurements unsteady measurements are performed, as described in section 2.2.2. The unsteady case is the actual fluid-structure interaction part of the experiment.

### 2.2.1 Steady Case

Steady measurements are performed to obtain the aerodynamic characteristics of the measurement setup. In this case the wing is fixed to the lower load cells by means of rods to prevent movement.

The series of angles of attack and flap angles at which measurements are performed is presented in Table 2.4. A mistake is made for ID number 13 where a flap angle of -1 degree is used instead of a flap angle of 1 degree. The measurements with varying angle of attack are performed first. When these were finished the angle of attack was fixed during the remainder of the entire experiment. The angle of attack and flap angle were set according to the procedure described in section 2.1.3. For each measurement the angle of attack and flap angle were checked using the Clinotronic PLUS device.

| ID | 1 | 2 | 3 | 4 | 5 | 6 | 7 | 8 | 9 | 10 | 11 | 12 | 13 | 14 | 15 |
|---|---|---|---|---|---|---|---|---|---|---|---|---|---|---|---|
| $\alpha$ [°] | -6 | -4 | -2 | -1 | 1 | 2 | 4 | 6 | 0 | 0 | 0 | 0 | 0 | 0 | 0 |
| $\delta$ [°] | 0 | 0 | 0 | 0 | 0 | 0 | 0 | 0 | -4 | -2 | -1 | 0 | -1 | 2 | 4 |

**Table 2.4:** Angle of attack $\alpha$ and flap angle $\delta$ inputs for the steady case.

### 2.2.2 Fluid-Structure Interaction Case

The steady case is meant to provide the steady characteristics of the wind tunnel setup and to act as a reference for the unsteady case. The part of the experiment comprising of fluid-structure interaction measurements is termed the unsteady or FSI case. In the FSI case coupling between the structural deformation and the aerodynamic flow is present. The specialty of this experiment is that no external forcing is applied to the wing.

Structural deformation is introduced by flap angle deflections, which are controlled by the servo engines. The flap deflection follows harmonic oscillation cycles. The flow condition and structural deformation repeat after each cycle such that the aerodynamics are assumed to be periodic. The flap deflection angle $\delta$ is described by a harmonic function

$$\delta = A \sin(2\pi f t),$$

where $A$ is the amplitude, $f$ is the frequency and $t$ is the running variable time. Instead of making use of the frequency $f$ it is more common to use the non-dimensional reduced frequency $k$, which is related to $f$ via

$$k = \frac{\pi f c}{V},$$

where $c$ is the chord length and $V$ is the free stream velocity. The experiment is performed for reduced frequencies $k = 0.1, 0.2, 0.3$. PIV measurements are performed only at a reduced frequency of 0.1, which corresponds to a frequency $f = 1.34$ Hz. The FSI case is performed at zero angle of attack and 2 degrees amplitude flap deflection. The amplitude of the plunge motion amounts to approximately 5 mm.

Measurements are performed using the measurement sensors described in section 2.1.3. Furthermore, using PIV the entire two-dimensional flow field about the wing at mid span is obtained in terms of a velocity vector field. The assumption of quasi steadiness enables to apply phase averaging to the results. Phase averaging consists of averaging multiple measurements that are taken at the same phase but in different cycles. Using phase averaging the average characteristics are obtained and fluctuations are averaged out.

## 2.3 Results of the steady case

The outputs of the steady case as well as the unsteady case are obtained following the procedure described in section 2.2. In this thesis only the results of the steady case are used for uncertainty quantification due to the limited time resources and because inferences can be made from the uncertainties in the steady part for the unsteady part of the experiment. Therefore only the results of the steady case are presented and discussed

here. In this section the raw data are presented; no corrections have been applied to these data.

The steady measurements are performed at various angles of attack and flap angles according to Table 2.4. The lift coefficient curves for varying angle of attack and flap angle are shown in Figure 2.6. As expected, both curves show approximately linear behavior and an increasing lift coefficient for increasing angle of attack or flap angle. Note that the $C_L - \alpha$ curve is not exactly linear for $\alpha$ between -3 and 3 degrees. The derivative of the lift coefficient with respect to the angle of attack $C_{L_\alpha} \approx 3.97$ rad$^{-1}$ and the lift coefficient derivative with respect to the flap angle $C_{L_\delta} \approx 1.93$ rad$^{-1}$. The fact that $C_{L_\alpha}$ is approximately twice as large as $C_{L_\delta}$ means that a change in angle of attack is two times more effective for $C_L$ than a similar change in flap angle.

Figure 2.7 shows the moment coefficient for various angles of attack and flap angles. The $C_M - \alpha$ curve shows roughly constant behavior around $C_M \approx -0.06$. Figure 2.3 shows that the two-dimensional results lie in the same range. In Figure 2.7b the $C_M - \delta$ curve shows linear behavior. The moment coefficient derivative with respect to the flap angle $C_{M_\delta} \approx -0.50$ rad$^{-1}$. A negative $C_{M_\delta}$ means that an increase in the flap deflection angle yields an increase in the pitch down moment.

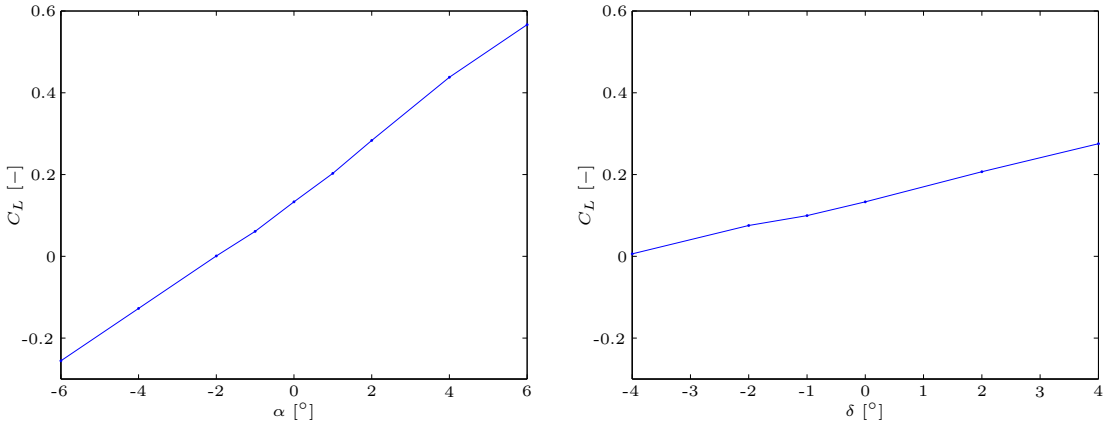


(a) $C_L - \alpha$ curve. (b) $C_L - \delta$ curve.

**Figure 2.6:** Experimental lift coefficient results shown separately for the angle of attack and flap angle ranges.

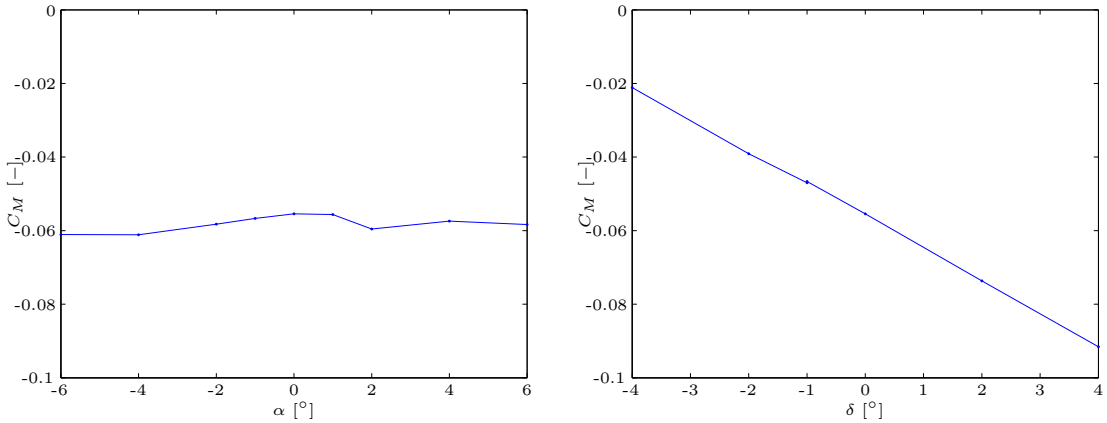


(a) $C_M - \alpha$ curve.

(b) $C_M - \delta$ curve.

**Figure 2.7:** Experimental moment coefficient results shown separately for the angle of attack and flap angle ranges.

# Chapter 3

# Simulation Methods

The fluid-structure interaction experiment is subject to various sources of uncertainty. Uncertainty quantification methods will be used to gain insight into the influence of uncertainties on the aerodynamic characteristics of the wind tunnel setup. Uncertainty quantification requires deterministic results of the aerodynamic characteristics, which are provided by simulation methods.

In this thesis two different simulation methods are selected to provide deterministic results. Section 3.1 describes the XFOIL panel method, which is used to perform two-dimensional simulations of the flow about the airfoil. Section 3.2 discusses the Tornado vortex lattice method, which is employed for including three-dimensional effects in the calculations. Computational Fluid Dynamics methods are not used because they are relatively expensive. In order to be able to compare between simulations and experimental results, corrections are applied to the simulations, as discussed in section 3.3.

## 3.1 XFOIL Panel Method

XFOIL is a panel method implementation developed by Drela [2011] for two-dimensional flow computations. Advantages of XFOIL are that it requires relatively less computational effort compared to common URANS codes and computations can be automated for performing uncertainty quantification analyses. Furthermore, the geometric variations in the airfoil can be taken into account by XFOIL since it uses relatively many surface panels compared to the VLM code employed in this thesis. The input consists of a coordinate file of the DU96W180 airfoil with 201 coordinate points.

### 3.1.1 General Concept

XFOIL is an enhanced panel method based flow solver that includes compressibility and viscous effects in the computations. The inviscid formulation of XFOIL is a linear-vorticity stream function panel method. For velocities up to sonic conditions a compressibility

correction is incorporated to correct for compressibility effects. Viscosity is taken into account in the region near the airfoil surface and in the wake by employing an integral boundary layer formulation. Options are included for either forced or free transition of the boundary layer from laminar to turbulent. The transition location is predicted employing the $e^N$ method. Furthermore, limited flow separation can be modeled by this flow solver.

### 3.1.2 XFOIL Settings

The XFOIL input conditions are chosen such that they reflect roughly the conditions during the wind tunnel experiment. The viscous formulation is employed to include boundary layer effects. Similar Reynolds and Mach numbers are used as in the experiment. In XFOIL the boundary layer computations can be modified by forcing transition and specifying the amplitude ratio $N_{crit}$ of the $e^N$ method. An amplitude ratio of 9 is employed that corresponds to an average turbulence level in wind tunnels according to Drela [2011].

According to section 2.1.2, in the experiment tripping wires are glued to the wing at $x_{tr,s} = 0.02c$ on the suction side and at $x_{tr,p} = 0.05c$ on the pressure side. The tripping locations at the suction and pressure side are referred to by $x_{tr,s}$ and $x_{tr,p}$ respectively. XFOIL computations are performed with tripping locations similar to the locations of the tripping wires in the experiment and the outputs are corrected according to section 3.3. In Figure 3.1b it is clear that the agreement between observational data and corrected XFOIL simulations for the moment coefficient is bad. The discrepancy between simulations and observations is believed to be caused mainly by model inadequacy of XFOIL and the corrections. The choice is made to introduces changes in the XFOIL simulations to improve on the moment coefficient results.

Since no checks are performed to assess the effectiveness of the tripping wires the transition location remains unknown. Therefore a XFOIL study is performed to find the tripping locations for which the XFOIL output agrees best with the experimental data. For various tripping locations the lift coefficient curves $c_l - \alpha$ and moment coefficient curves $c_m - \alpha$ are computed. After applying the corrections from section 3.3 these curves are compared with the experimental data. Figure 3.1 shows that the tripping location has considerable influence especially on the moment coefficient results. Visual inspection of the $c_m - \alpha$ curves yields that the curve corresponding to a tripping location of $0.60c$ agrees best with the measured moment data.

| tripping location | | transition location ($\alpha = 0$) | | simulation discrepancy | |
|---|---|---|---|---|---|
| $x_{tr,s}$ | $x_{tr,p}$ | $x_{tr,s}$ | $x_{tr,p}$ | $\overline{\epsilon_\Delta}(c_l)$ | $\overline{\epsilon_\Delta}(c_m)$ |
| 0.02 | 0.02 | 0.02 | 0.05 | 0.0579 | 0.0156 |
| 0.40 | 0.40 | 0.40 | 0.40 | 0.0842 | 0.0103 |
| 0.50 | 0.50 | 0.50 | 0.50 | 0.0886 | 0.0088 |
| 0.55 | 0.55 | 0.55 | 0.57 | 0.0891 | 0.0082 |
| 0.60 | 0.60 | 0.55 | 0.65 | 0.0876 | 0.0082 |
| 0.75 | 0.75 | 0.55 | 0.68 | 0.0843 | 0.0092 |
| 1.00 | 1.00 | 0.55 | 0.68 | 0.0839 | 0.0093 |

**Table 3.1:** Lift and moment coefficient simulation discrepancy of the XFOIL output with respect to the measurement data for different forced transition locations.

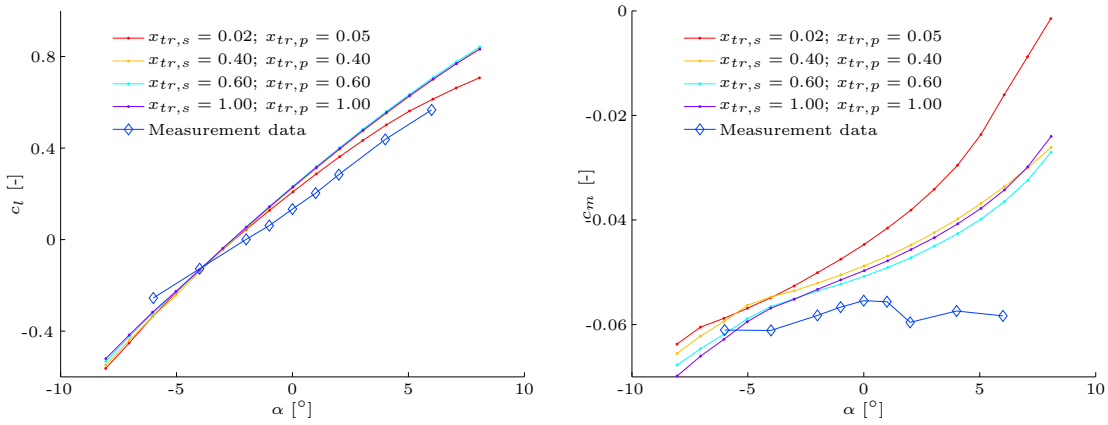


(a) $c_l - \alpha$ curves.

(b) $c_m - \alpha$ curves.

**Figure 3.1:** Corrected XFOIL results compared with measurement data. Simulations are performed to obtain the lift coefficient $c_m$ and moment coefficient $c_m$ for various tripping locations on the suction side ($x_{tr,s}$) and on the pressure side ($x_{tr,p}$).

Investigation of the discrepancy between simulation output and observations yields useful information for selecting a tripping location. The simulation discrepancy of the XFOIL output with respect to the measurement data is given by

$$\epsilon_\Delta (c_l) = \sqrt{\left(c_{l_{x_{tr}}} - c_{l_m}\right)^2},$$

where $c_{l_{x_{tr}}}$ the lift coefficient corresponding to a certain tripping location and $c_{l_m}$ the measurement data. The simulation discrepancy averaged over the angle of attack is presented in Table 3.1 together with the input tripping location and output transition location at zero angle of attack. The output transition location can differ from the input tripping location because the $e^N$ method is always active irrespective of the specification of a forced transition location. Table 3.1 shows that tripping locations of $0.55c$ and $0.60c$ yield the smallest moment coefficient simulation discrepancy. From these two input tripping locations the smallest lift coefficient simulation discrepancy is obtained for a tripping location of $0.60c$. Therefore, based on the simulation discrepancy results and the curve shapes a tripping location of $0.60c$ at both suction and pressure side is selected for XFOIL computations throughout this thesis.

A transition location of $0.60c$ is unlikely to occur in the experiment, since it means that the tripping wires are very ineffective. Therefore, the XFOIL tripping location will not correspond to a true physical quantity anymore, but rather to a value that yields the best agreement between simulations and observations. Another approach to decreasing the discrepancy in moment coefficient data would have been to use the experimental tripping locations as XFOIL inputs and instead improve on the corrections.

### 3.1.3 Grid Convergence Study

A grid convergence study is performed to determine the optimal amount of panels on the airfoil surface. Various grids are designed by choosing a range of number of panels

$N_{panels}$ from 100 to the XFOIL limit of 350. The resulting $c_l - \alpha$ curves and $c_m - \alpha$ curves are shown for the various grid sizes in Figure 3.2. Especially the curves of the moment coefficient show differences between the finest grid and the grid corresponding to 300 panels.

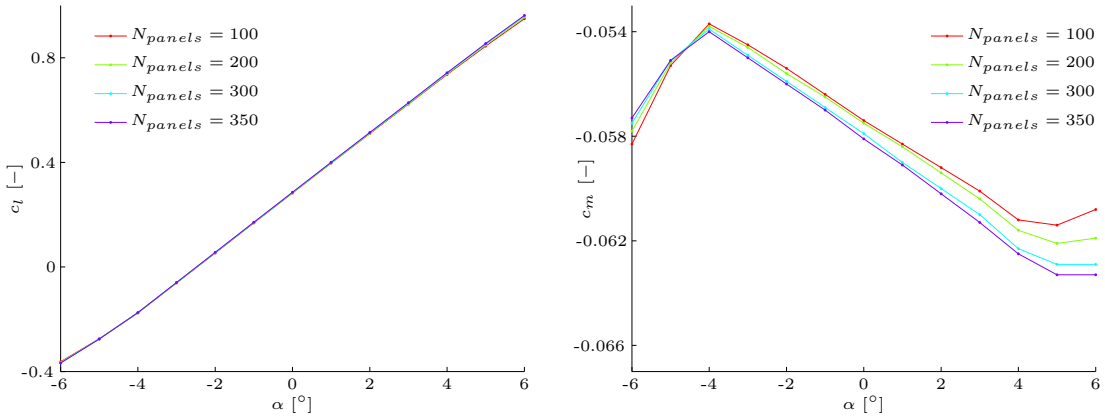


(a) $c_l - \alpha$ curve. (b) $c_m - \alpha$ curve.

**Figure 3.2:** Curves of the lift and moment coefficient for various grid size computed by XFOIL.

| | $N_{panels}$ [-] | $t$ [$s$] | $\overline{\epsilon}_{c_l}$ [-] | $\overline{\epsilon}_{c_m}$ [-] |
|---|---|---|---|---|
| Grid 1 | 100 | 0.11 | 0.0142 | 0.0161 |
| Grid 2 | 200 | 0.24 | 0.0046 | 0.0051 |
| Grid 3 | 300 | 0.92 | 0.0028 | 0.0031 |
| Grid 4 | 350 | 1.70 | n/a | n/a |

**Table 3.2:** XFOIL convergence study results summary. The computational effort is expressed in evaluation time $t$. The average discretization error $\overline{\epsilon}_{c_{l,m}}$ is computed using the finest grid as a reference.

More information is provided by the discretization error, which is computed using the finest grid solution as a reference. The discretization error of the lift coefficient $\epsilon_{c_l}$ is computed as

$$\epsilon_{c_l} = \frac{\sqrt{(c_{l_i} - \hat{c}_l)^2}}{|\hat{c}_l|},$$

where $c_{l_i}$ is the lift coefficient corresponding to grid $i$ and $\hat{c}_l$ is the lift coefficient computed for the finest grid. The same formula applies for computing the discretization error related to the moment coefficient. The discretization errors averaged over the angle of attack are shown in Figure 3.3. These graphs show a clear difference between the outputs of the finest grid and the grid corresponding to 300 panels. A summary of the convergence study results is presented in Table 3.2. In this table the computational effort is expressed in evaluation time $t$.

Based on the fact that differences between the grids corresponding to $N_{panels} = 300$ and $N_{panels} = 350$ are clearly present in the $c_m$ data, the finest grid with $N_{panels} = 350$

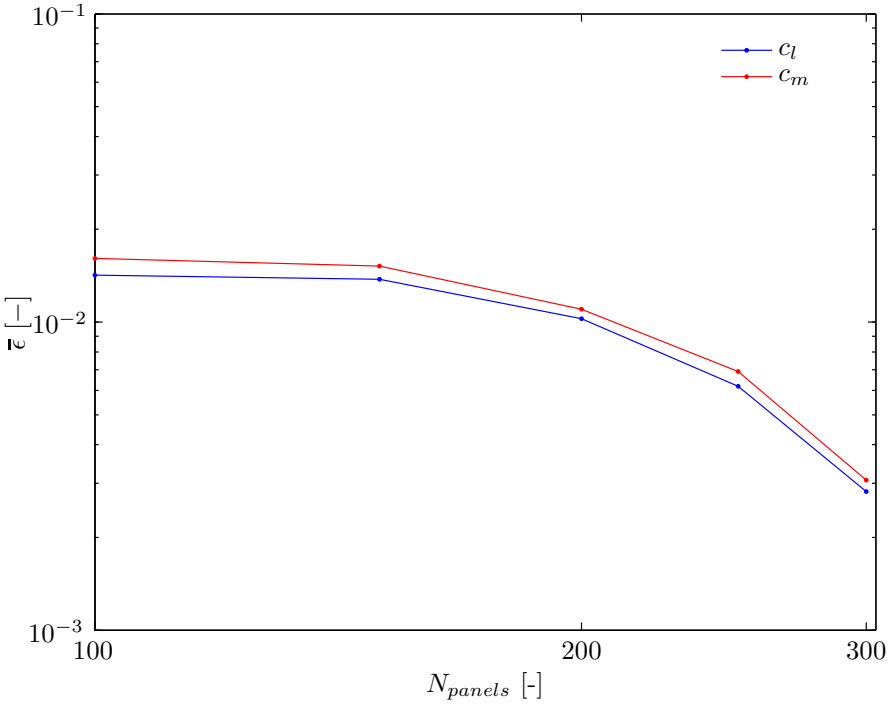


**Figure 3.3:** XFOIL computed discretization errors in $c_l$ and $c_m$ averaged over angle of attack for various grid size.

| | |
|---|---|
| Geometry | |
| Airfoil | DU96W180 |
| Number of panels $N_{panels}$ | 350 |
| Flow conditions | |
| Mode | viscous |
| Reynolds number Re | $7 \cdot 10^5$ |
| Mach number Ma | 0.06 |
| Boundary layer | |
| Tripping location | |
| suction side $x_{tr,s}$ | $0.60c$ |
| pressure side $x_{tr,p}$ | $0.60c$ |
| Amplitude ratio $N_{crit}$ | 9 |

**Table 3.3:** XFOIL input settings for the discretized geometry, flow conditions and boundary layer parameters.

is selected to be used throughout this thesis. The computation time of 1.7 seconds is reasonable even for the evaluation of large input matrices such as used in uncertainty quantification.

A summary of the XFOIL settings is presented in Table 3.3 including the flow conditions, boundary layer parameters and number of panels.

## 3.2 Tornado Vortex Lattice Method

Tornado is a MATLAB implementation of a Vortex Lattice Method (VLM) developed by Melin [2000] for three-dimensional flow computations. This code is employed in the current research because it enables to model the influence of input parameters that are related to the fact that the experimental setup is three-dimensional. Furthermore, computation runs are relatively cheap in terms of computation effort compared to for example URANS codes.

### 3.2.1 General Concept

The vortex lattice method is based on potential flow theory. Potential flow theory can be employed to perform computations for inviscid, irrotational and incompressible flows. Tornado provides an option for compressibility corrections to computations of high subsonic Mach number flows. Furthermore the method is limited to the linear part of the $C_L - \alpha$ curve, i.e. relatively small angle of attack. The vortex lattice method makes use of basic solutions to Laplace's equation, i.e. the equation that is central to potential flow theory, to build up the solution. The basic solution employed by Tornado for its three-dimensional computations is a horseshoe vortex. The geometry is divided into a finite amount of panels. A lattice of vortex lines originates from the panels and propagates into the wake. The strength of the vortices is computed using the zero normal velocity condition at the surfaces. The wing is treated as a thin airfoil at the chord line. The camber of the airfoil is taken into account by twisting the panel normal vectors according to the gradient of the camber.

Numerically the vortex lattice method revolves around the inversion of a large matrix to obtain the vortex strengths. The matrix inversion step requires a lot of computer memory for large matrices. The computer's memory therefore puts limits on the matrix size and thereby on the grid size and accuracy of the computations. Furthermore, intersections between vortex lines and collocation points can arise in the domain and cause computational problems. Since the tangential velocity of a vortex in its center is infinite, the contribution of an intersecting vortex in the collocation point will be infinite. The Tornado VLM implementation deals with this computational difficulty by omitting the contribution of intersecting or nearly intersecting vortex lines. Omission of certain vortex contributions introduces errors. Therefore during the design of the mesh it should be taken into account that preferably no intersecting vortex lines should be present.

The computations are performed using the DU96W180 profile being defined at 201 coordinates. The input velocity is 21 m/s and the density is 1.225 kg/m$^3$.

### 3.2.2 Grid Convergence Study

A simplified geometric model of the experimental wind tunnel setup is used for the Tornado computations, see Figure 3.4. The wing is modeled as a thin plate with adjusted panel normals according to the wing camber. The wing chord length amounts to 0.5 meters and the span to 1.8 meters. The walls are modeled as flat plates at each side of the wing with a height of 3 meters. Each wall is divided into two parts to model the slit where the wing shafts stick through. The space between the front and the back part of the walls amounts to 30 millimeters and runs entirely from the lower to the upper side. The widths of the front and back part are 0.265 and 0.73 meters respectively. The wing is positioned with respect to the walls such that the quarter chord point is in line with the middle line of the slits. Furthermore, the vertical position of the wing is aligned with half the height of the walls via the panel normals. Furthermore, changing the angle of attack and flap angle do not yield changes in the lattice, which is advantageous regarding the intersecting vortex lines.

The discretization error of the Tornado method is determined for various grid sizes. Taking into account the limitations of the method, as described in section 3.2.1, five grids are designed. The successive grids are obtained from scaling up the number of panels in the chord wise and span wise direction on each surface of the initially designed grid. Computations for each grid are performed for various angle of attack, i.e. $\alpha = -2, -1, 0, 1, 2°$.

The discretization error related to a grid is computed using the finest grid solution as a reference. The discretization error in the lift coefficient $\epsilon_{C_L}$ is computed as

$$\epsilon_{C_L} = \frac{\sqrt{\left(C_{L_i} - \hat{C}_L\right)^2}}{\left|\hat{C}_L\right|},$$

where $C_{L_i}$ is the lift coefficient for grid $i$ and $\hat{C}_L$ is the lift coefficient computed for the finest grid. The same formula applies for computing the discretization error related to the moment coefficient $C_M$. The average discretization error is obtained from averaging discretization error values that are obtained for various angles of attack. In Table 3.4 for each grid the number of panels $N_{panels}$, the computational effort expressed in evaluation time $t$ and the average discretization error $\overline{\epsilon}_{C_{L,M}}$ are presented.

| | $h_{wing}$ $[m]$ | $N_{panels}$ [-] | $t$ $[s]$ | $\overline{\epsilon}_{C_L}$ [-] | $\overline{\epsilon}_{C_M}$ [-] |
|---|---|---|---|---|---|
| Grid 1 | 0.1333 | 104 | 0.5 | 0.1198 | 0.1789 |
| Grid 2 | 0.0667 | 360 | 3.4 | 0.0289 | 0.0608 |
| Grid 3 | 0.0333 | 1440 | 56.3 | 0.0080 | 0.0198 |
| Grid 4 | 0.0222 | 3240 | 289.8 | 0.0039 | 0.0072 |
| Grid 5 | 0.0167 | 5440 | 976.9 | n/a | n/a |

**Table 3.4:** Grid study results of the Tornado vortex lattice method. For each grid the length of a wing panel in the chord wise direction $h_{wing}$, the total number of panels $N_{panels}$, the computational effort expressed in evaluation time $t$ and the lift and moment coefficient discretization errors $\overline{\epsilon}_{C_{L,M}}$ are presented.

The discretization error curves of the lift and moment coefficients are plotted versus the number of panels in Figure 3.5. The discretization error curves show convergence for

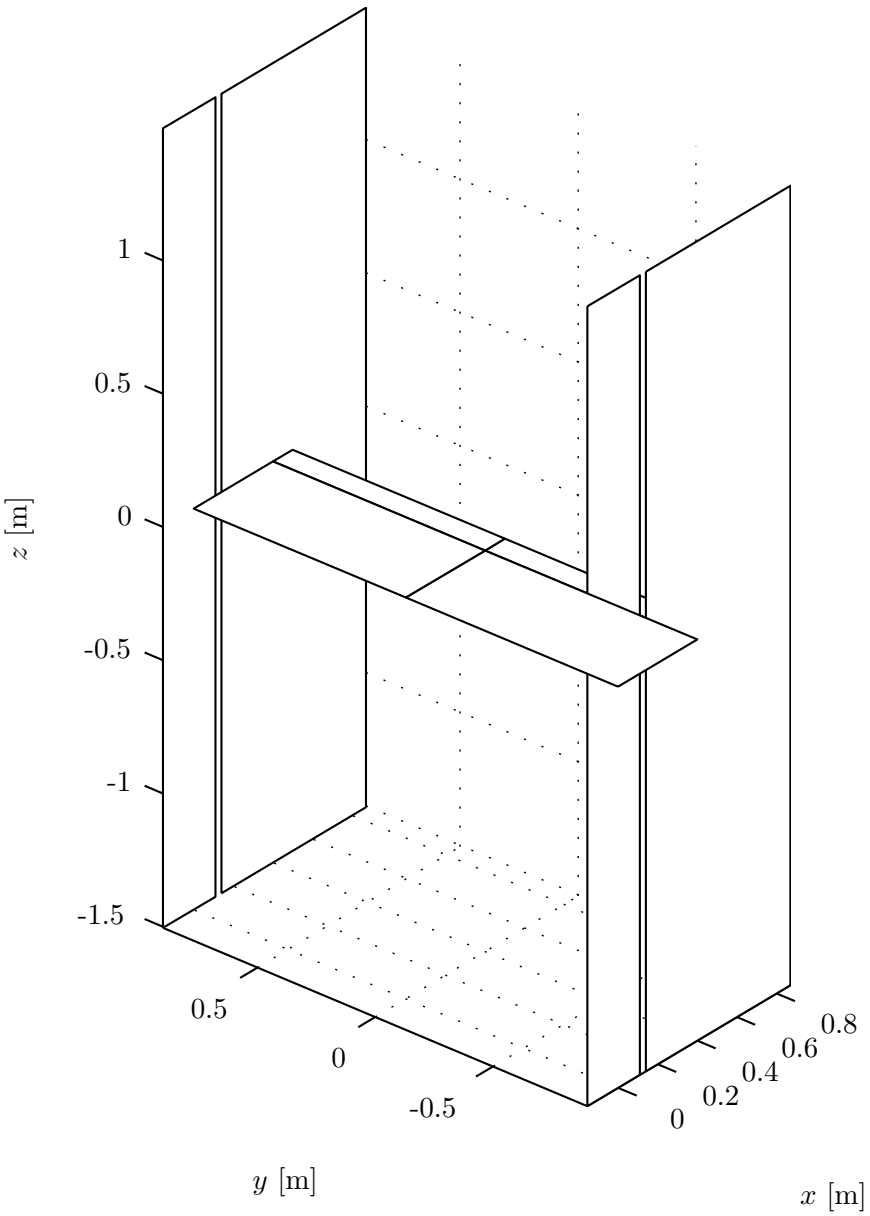


**Figure 3.4:** Simplified model of the wind tunnel setup used in the Tornado computations. The airflow direction is aligned with the $x$-axis and approaches the setup from the negative $x$-axis.

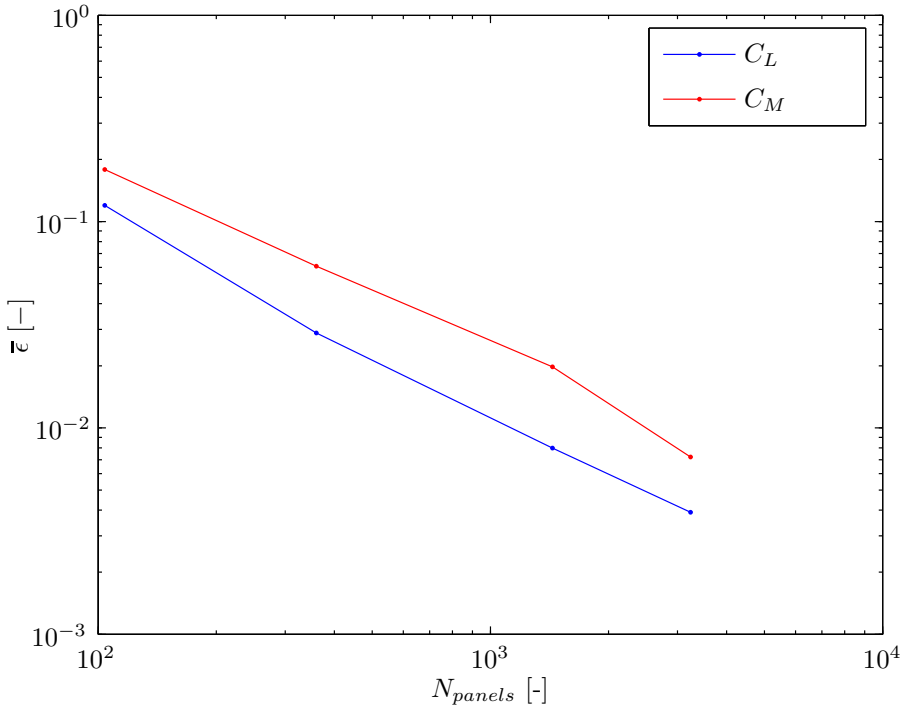


**Figure 3.5:** Tornado grid convergence study results expressed in the discretization error averaged over the angle of attack for the lift and moment coefficients.

increasing grid size. Based on the discretization errors for $C_L$ and $C_M$ and the wing panel size $h_{wing}$ the order of accuracy of Tornado is determined as 1.5.

Tornado computations will mainly be used for modeling the influence of the gap width. Since the gap width is a very small feature on millimeter level, a fine grid is required to model it accurately. Therefore, despite the fact that grid 4 yields small discretization errors and the fact that the computation time increases considerably for increasing grid size, grid 5 will be used throughout this thesis.

## 3.3 Corrections

In wind tunnel experiments, effects are present that are usually not taken into account in simulations. Corrections can be applied in order to be able to compare between wind tunnel experiments and simulations. In this thesis the choice is made to correct the simulation output data and leave the experimental output data unaltered. This approach is convenient for performing uncertainty quantification when aspects of the corrections are included.

Three corrections are applied to the simulation output data in a specific order. First, section 3.3.1 discusses that the two-dimensional XFOIL computations are corrected for three-dimensional effects, which are caused by the presence of a gap between the wing and the side walls. Secondly, open wind tunnel corrections are applied to correct for streamline curvature, see section 3.3.2. Finally a correction is made for the chord length discrepancy,

which is deducted from geometry measurements, as described in section 3.3.3.

### 3.3.1 Gap Correction

The correction for the three-dimensional effects takes only into account the presence of the gap between wing and side walls. The presence of a gap introduces wing tip vortices. Based on the assumption that the wing tip vortices are the main three-dimensional features in the flow only a gap correction is applied to account for three-dimensional effects. The influence of the side walls and the presence of a slit in the side walls are assumed to have minor influence on the flow.

The wing tip vortices cause a decrease in effective angle of attack and an increase of drag by introducing induced drag. The gap correction is computed using the inviscid vortex lattice method Tornado. The gap correction is applied to two-dimensional viscous XFOIL computations. This approach is based on the assumption that viscosity has minor effect on the corrections.

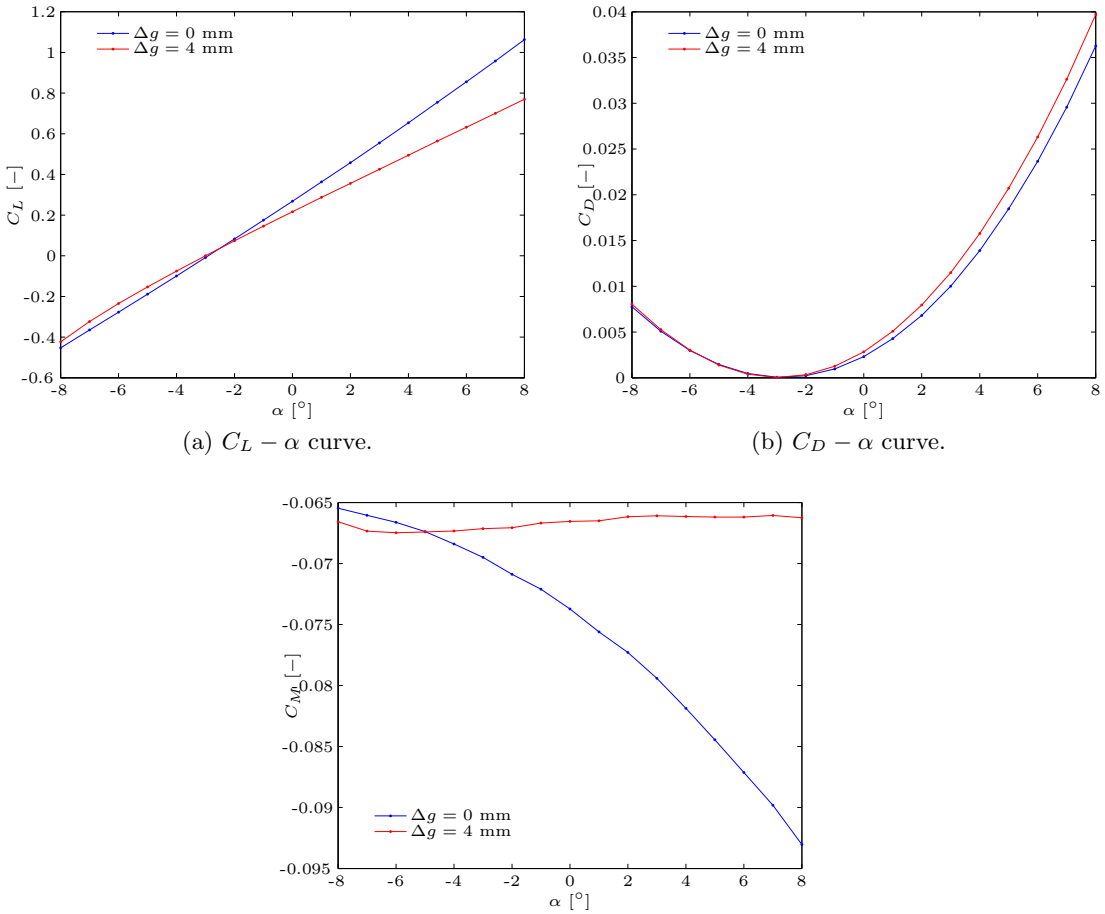


(a) $C_L - \alpha$ curve.

(b) $C_D - \alpha$ curve.

(c) $C_M - \alpha$ curve.

**Figure 3.6:** Lift, drag and moment coefficient curves computed by Tornado for zero and non zero gap size.

Computations are performed using Tornado at zero gap size ($\Delta g = 0$ mm) and nonzero gap size ($\Delta g = 4$ mm). Since the gap is very small the finest grid, i.e. grid number 5, is used to model the small features accurately. Figure 3.6 shows the $C_L - \alpha$, $C_D - \alpha$ and $C_M - \alpha$ curves for zero and non-zero gap size. Practically the correction consists of a discrepancy term that is added to the XFOIL output. The lift coefficient discrepancy is computed as

$$\delta C_L = C_L\left(\alpha, \Delta g = 4\text{mm}\right) - C_L\left(\alpha, \Delta g = 0\text{mm}\right),$$

where $C_L\left(\alpha, \Delta g\right)$ is the lift coefficient as a function of angle of attack $\alpha$ and gap size $\Delta g$. Dropping the argument $\alpha$ the lift coefficient discrepancy can be written as a function of the zero gap size lift coefficient $\delta C_L\left(C_{L_{\Delta g=0}}\right)$. A similar procedure is followed to obtain the drag coefficient discrepancy $\delta C_D\left(C_{L_{\Delta g=0}}\right)$ and the moment coefficient discrepancy $\delta C_M\left(C_{L_{\Delta g=0}}\right)$ as a function of the zero gap size lift coefficient. In order to obtain analytic functions polynomial fitting is applied to the discrepancy data with order 5. The resulting functions for the discrepancy terms are given by

$$\begin{aligned}
\delta C_L\left(C_{L_{\Delta g=0}}\right) &= 10^{-2}\cdot\Big(-9.3C^5_{L_{\Delta g=0}} + 22.8C^4_{L_{\Delta g=0}} - 20.7C^3_{L_{\Delta g=0}} + 16.2C^2_{L_{\Delta g=0}} \\
&\quad +19.0C_{L_{\Delta g=0}} - 0.8\Big), \\
\delta C_M\left(C_{L_{\Delta g=0}}\right) &= 10^{-3}\cdot\Big(5.2C^5_{L_{\Delta g=0}} - 11.9C^4_{L_{\Delta g=0}} + 9.3C^3_{L_{\Delta g=0}} - 9.6C^2_{L_{\Delta g=0}} \\
&\quad -15.6C_{L_{\Delta g=0}} - 2.5\Big), \\
\delta C_D\left(C_{L_{\Delta g=0}}\right) &= 10^{-4}\cdot\Big(-14.0C^5_{L_{\Delta g=0}} + 27.0C^4_{L_{\Delta g=0}} + 4.5C^3_{L_{\Delta g=0}} - 40.1C^2_{L_{\Delta g=0}} \\
&\quad -9.4C_{L_{\Delta g=0}} + 0.05\Big).
\end{aligned}$$

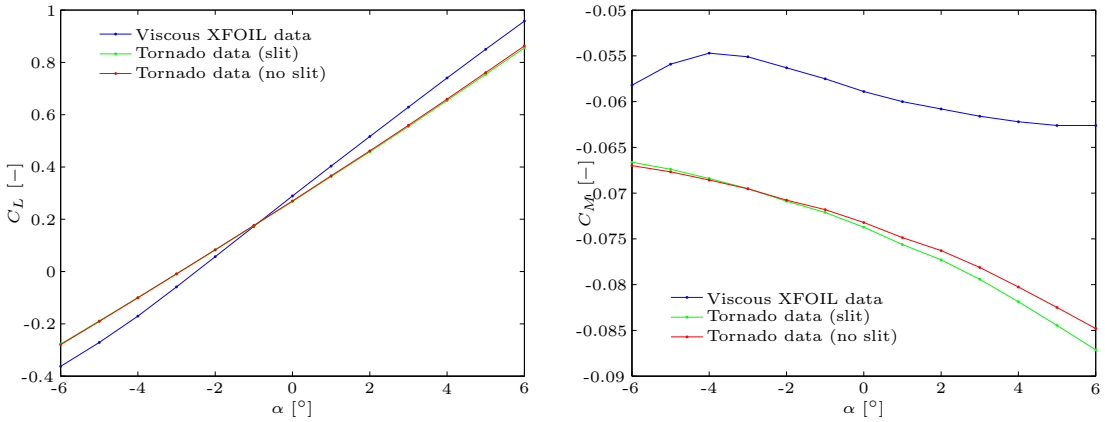


(a) Lift coefficient data.

(b) Moment coefficient data.

**Figure 3.7:** Comparison of inviscid Tornado computations with and without slit at zero gap size and two-dimensional viscous XFOIL computations.

Instead of the Tornado $C_{L_{\Delta g=0}}$ the two-dimensional viscous XFOIL $c_l$ is used as an input for the discrepancy term. This is based on the assumption that the zero gap size lift coefficient computed by Tornado compares reasonably well with the viscous two-dimensional

lift coefficient computed by XFOIL. A justification of this assumption is obtained from a comparison of Tornado computations with XFOIL computations. In Figure 3.7 uncorrected XFOIL simulations are presented together with Tornado computations at zero gap size for cases that a slit is present and absent in the side walls. The maximum difference amounts to 0.1 in $C_L$ for large angle of attack. For angles of attack around zero the difference is very small. The uncertainty analysis is meant to provide uncertainty characteristics that can be used to make inferences for the fluid-structure interaction experiment. The fluid-structure interaction experiment is performed at zero angle of attack. Therefore, the difference between the curves is acceptable.

Finally the corrected lift, drag and moment coefficient are obtained from

$$\begin{aligned} C_{L_g} &= c_l + \delta C_L\left(c_l\right), \\ C_{D_g} &= c_d + \delta C_D\left(c_l\right), \\ C_{M_g} &= c_m + \delta C_M\left(c_l\right), \end{aligned}$$

where $C_{L_g}$, $C_{D_g}$ and $C_{M_g}$ are the coefficients corrected for the gap. The coefficient discrepancy terms as a function of the XFOIL $c_l$ are denoted by $\delta C_L\left(c_l\right)$, $\delta C_D\left(c_l\right)$ and $\delta C_M\left(c_l\right)$.

For the lift coefficient the assumption is made that the Tornado outputs for zero gap width computations correspond approximately to the two-dimensional XFOIL results. For the moment coefficient data this assumption is problematic. Figure 3.7b shows large discrepancies between XFOIL and Tornado computations. The XFOIL simulations agree with the moment coefficient data obtained from a two-dimensional experiment, see Figure 2.3b. The introduction of a slit in the side walls increases the discrepancy. The fact that the moment coefficient curve computed by Tornado shows considerable differences with two-dimensional results introduces probably model inadequacy errors.

### 3.3.2 Wind Tunnel Corrections

Wind tunnel flows differ from aerodynamic flows encountered by aircraft in real flight. Brooks et al. [1984] developed a method to correct for flow effects of open jet wind tunnels. The two-dimensional open wind tunnel corrections treat the phenomenon of streamline curvature. The method is based on the assumption of a constant (ambient) pressure jet flow boundary. Furthermore, stream wise buoyancy and flow blocking of the model and the wake are considered negligible since the air stream is free to expand in a normal manner. Instead of correcting the experimental data the corrections are applied in a reverse sense to the simulations in this thesis.

The streamline curvature corrections affect the drag and moment coefficient and the slope of the $C_L - \alpha$ curve. The lift coefficient for simulation outputs $C_{L_g}$ is equal to the wind tunnel result $C_{L_t}$

$$C_{L_t} = C_{L_g},$$

where the subscript $t$ refers to wind tunnel conditions. Note that this does not mean that the lift curve remains unchanged, since corrections for the angle of attack yield changes

in the lift curve. The corrected wind tunnel drag and moment coefficient are given by

$$\begin{aligned} C_{D_t} &= C_{D_g} - \left( -\frac{\sqrt{3\sigma}}{\pi} C_{L_t} \right) C_{L_t} \\ C_{M_t} &= C_{M_g} + \frac{\sigma}{2} C_{L_t}, \end{aligned}$$

where $\sigma = \frac{\pi^2}{48} \left( \frac{c}{h_t} \right)^2$, $c$ refers to the airfoil chord length and $h_t$ to the tunnel height. The lift curve slope is affected by correcting the angle of attack as

$$\alpha_t = \alpha + \frac{\sqrt{3\sigma}}{\pi} C_{L_t} + \frac{2\sigma}{\pi} C_{L_t} + \frac{\sigma}{\pi} \left( 4 C_{M_t} \right).$$

The application of these corrections to the gap corrected simulation data yields the equivalent wind tunnel values of the simulation outputs.

### 3.3.3 Chord Length Correction

The chord length of the DU96W180 wing is designed to be 500 millimeter. However, manufacturing of the flap and the hinge connections to the wing have introduced discrepancies between the DU96W180 geometry and the actual geometry. Careful investigation of the CMM and Photogrammetry measurements, which are described in chapter 5, reveals that the average chord length of the wing amounts to 505 millimeter, with an uncertainty of less than 1 millimeter. The normalization of the experimental data is based on a chord length of 500 millimeter, according to the design. To account for this discrepancy the computational results of the aerodynamic coefficients will be multiplied with a correction factor of 1.01. The chord length discrepancy is introduced as a correction because it is an uncertain variable and it differs from the design value.

# Chapter 4

# Uncertainty Quantification Methodology

Uncertainty quantification provides means to understand the reasons for the failure to reproduce the experimental results with simulations. Uncertainties exist at the side of the experiment and at the side of the simulation model. In this thesis uncertainty quantification is used to obtain the uncertainty characteristics of the experimental observations. Complementing the experimental results with uncertainty characteristics provides a strong basis for computer code validation.

Experimental observations as well as the simulations are subject to various errors. A clear distinction between various sources of error is required for the understanding of the reasons of uncertainties. A classification of the various sources of error is given in section 4.1. The framework for uncertainty quantification is described in section 4.2.

In this thesis various methods are employed for uncertainty quantification. The kriging method and the related cokriging method are interpolation methods, which are described in section 4.3. Section 4.4 discusses the probabilistic collocation method, which is used for interpolation, uncertainty analysis and sensitivity analysis. Finally in section 4.5 the Markov chain Monte Carlo method is explained, which is widely used for Bayesian inference.

## 4.1 Classification of Errors

Computer codes virtually never provide results that are equal to experimental observations. The discrepancies between code outputs and experimental observations are caused by various sources of error. A clear classification of the sources of errors is indispensable for the understanding of the reasons of uncertainty. Kennedy & O'Hagan [2001a] provide a widely adopted classification of errors according to their source.

**Parametric uncertainty** Due to a lack of knowledge there can be uncertainty about some code inputs, such as the angle of attack or the wind velocity. Parametric uncertainty implies uncertainty on code outputs including true randomness in system parameters, even for a deterministic model.

**Model inadequacy** No model is an exact representation of reality, and modeling assumptions may lead to greater or lesser error in results. Model inadequacy refers to the difference between the model output at true values of input parameters and reality. Since the real system may itself exhibit physical randomness, inadequacy is defined as the difference between the true mean value of the real process and the code output at true input values.

**Discretization error** The numerical error resulting from solving a model described in Partial Differential Equations (PDEs) on a discrete mesh is referred to as the discretization error. The discretization error is a function of the numerical scheme and is a very important source of error when solving PDEs. The discretization error can be reduced by refining the mesh, which normally increases the computational costs.

**Residual variability** Computer codes are supposed to predict the value of some real process under conditions specified by the inputs. In practice, the outputs may not always take the same value for the same inputs. This variability may be caused by the fact that the process itself is stochastic, or due to the fact that more conditions need to be specified. Furthermore, in this error also finite-precision arithmetic is taken into account.

**Observation error** The difference between the true value of a physical quantity and its experimentally measured value is referred to as the observation error. When making use of experimental data we should allow for the possibility of measurement errors. In case measurement errors are unbiased they are termed observational noise.

The influence of the first three sources of error can generally be estimated using a simulation code or comparison simulation outputs with experimental observations. The observation error needs to be determined or estimated when performing experiments. On the basis of the error estimates the code can be said to correctly represent reality to a specified confidence. Confidence levels are provided by uncertainty quantification using the error estimates.

## 4.2 Bayesian Inference

In aerodynamics, complex computer codes are usually employed to perform uncertainty quantification. Bayesian statistics provides a useful framework to successfully obtain uncertainty characteristics with reasonable computation effort. The uncertainty quantification methods discussed in this chapter are based on a Bayesian framework or can be incorporated into Bayesian inference.

Bayesian inference boils down to combining prior knowledge and observations for posterior inference. Wikle & Berliner [2006] explain the concept of Bayesian inference in a framework consisting of three steps. The first step is to formulate a full probability

model that comprises a joint probability distribution of all observable and unobservable components of interest, e.g. data, process and parameters. The second step is to find the conditional distribution of the unobservable quantities given the observed data by applying Bayes' theorem. The last step is to evaluate the ability of the model to adequately characterize the processes of interest.

Bayesian inference is mathematically described by Bayes' theorem

$$p(x|y) = \frac{p(y|x)p(x)}{p(y)}, \tag{4.1}$$

where $p$ refers to a probability distribution, $x$ are the unobservable quantities of interest and $y$ the observed data. The four components of the formula have their own specific meaning. The data distribution $p(y|x)$ refers to the probability distribution of the data, given the unobservable quantities. The prior distribution $p(x)$ quantifies the a priori knowledge of the unobservable quantities. The marginal distribution $p(y) = \int p(y|x)p(x)dx$ is also known as the prior predictive distribution. It can be solved analytically for a very limited number of cases since the integral gets easily too complicated. It is mainly a normalization term that is often left out. Finally, the posterior distribution $p(x|y)$ is the update of the prior knowledge about the unobservable quantities $p(x)$ given the actual observational data $y$. In case the normalization term is left out in Bayes' formula it is described by

$$p(x|y) \propto p(y|x)p(x). \tag{4.2}$$

This formula states that the posterior distribution is proportional to the data distribution multiplied by the prior distribution. Bayes' formula expresses the essence of Bayesian statistics as a framework that combines prior knowledge and observations to make inferences about uncertain processes.

## 4.3 Kriging

Kriging is a technique employing Gaussian processes for the interpolation of outputs of simulations or experiments. Since many functions are generally very complex and expensive, Gaussian processes are used to model the outputs. Kriging provides predictions of a process at unevaluated inputs and corresponding kriging uncertainty measures. Prior knowledge can be included in the interpolation process by specifying a mean and covariance function. The kriging approach employed here is assembled from work of Wikle & Berliner [2006], Kennedy & O'Hagan [2000] and Forrester et al. [2007]. Starting from the more basic universal kriging method in section 4.3.1 the more complicated cokriging method will be explained in section 4.3.2. A simple example of kriging applied to an analytic function reveals the capabilities of cokriging, see section 4.3.3.

### 4.3.1 Universal Kriging

Universal kriging is an interpolation method that is applicable to one data source. It differs from other kriging methods, such as ordinary kriging, in that the mean is a function of the covariates. The description employed here is chosen such that it can easily be extended to cokriging.

### Mathematical Framework

Suppose we have a process $\eta$ that can be an experiment or a simulation code. At a set of $n$ design input data $D = \{x_1, \ldots, x_n\}$ the process is evaluated resulting in $n$ observations $z$. The prediction of the process at untried inputs $x$ can be modeled by a Gaussian process with mean function

$$m(x) = h(x)^T \beta + t(x)^T V^{-1}(z - H\beta), \tag{4.3}$$

where $h$ is a vector of regression functions and $\beta$ a vector of corresponding regression parameters. The regression parameters and matrix $H$ are given by

$$\beta = \left(H^T V^{-1} H\right)^{-1} H^T V^{-1} z, \qquad H = \begin{pmatrix} h(x_1)^T \\ \vdots \\ h(x_n)^T \end{pmatrix}.$$

The second part of Equation (4.3) consists of a weighted sum of the difference between data and estimated mean where $t(x)$ is the covariance between data and untried inputs given by

$$t(x)^T = \sigma^2 A\left(x, D\right)$$

Furthermore, $V$ is the data covariance matrix expressed by

$$V = \sigma^2 A\left(D, D\right) + \epsilon I_n,$$

where $\sigma^2$ is the data standard deviation, or spread of the data around the kriging mean, and $\epsilon$ the process output uncertainty. Since $V$ is a symmetric positive definite matrix a Cholesky decomposition is applied to reduce computation time. The matrix of correlations between two points in the input data set $D$, with $i, j$ element, is given by

$$A\left(x_i, x_j\right) = c\left(x_i, x_j\right),$$

where

$$c\left(x, x'\right) = \exp\left\{-\frac{1}{2b^2}\left(x - x'\right)^T \left(x - x'\right)\right\}.$$

The correlation length $b$ defines the degree of influence one data point has on another data point. The prediction covariance function can be written as

$$\begin{aligned} \operatorname{cov}\left(x, x'\right) \;=\; & \left(\sigma^2 c\left(x, x'\right) + \epsilon I_n\right) - t(x)^T V^{-1} t(x) \\ & + \left(h(x) - H^T V^{-1} t(x)\right)^T \left(H^T V^{-1} H\right)^{-1} \left(h(x) - H^T V^{-1} t(x)\right). \end{aligned} \tag{4.4}$$

For $x = x'$ the prediction covariance function, Equation (4.4), gives an estimate of the uncertainty on the prediction of the process $\eta$ at untried inputs $x$.

### Estimation of Hyperparameters

The two parameters that need to be chosen are the correlation length $b$ and the data standard deviation $\sigma^2$. These parameters are called hyperparameters. Forrester et al.

[2007] shows that a closed form expression can be obtained to determine the data standard deviation from a maximum likelihood estimate (MLE) as

$$\sigma^2 = \frac{(z - H\beta)^T \left[A\left(D, D\right) + \epsilon I_n\right](z - H\beta)}{n},$$

where $n$ is the number of elements in the data vector $z$. The $b$ hyperparameters can be estimated from maximizing the distribution of the data conditional on the hyperparameters, which is given by

$$\begin{aligned} p\left(z|b, \sigma^2\right) &= \frac{1}{(2\pi)^{k/2}\left|\sigma^2 A\left(D, D\right) + \epsilon I_n\right|^{1/2}} \cdot \\ &\quad \exp\left(-\frac{1}{2}(z - \beta 1_n)^T \left[\sigma^2 A\left(D, D\right) + \epsilon I_n\right]^{-1}(z - \beta 1_n)\right). \end{aligned} \tag{4.5}$$

This distribution function is obtained using Bayes' formula and taking weak priors for the hyperparameters. Taking the logarithm of Equation (4.5) it can be shown that we should minimize

$$\log\left|\sigma^2 A\left(D, D\right) + \epsilon I_n\right| + (z - \beta 1_n)^T \left[\sigma^2 A\left(D, D\right) + \epsilon I_n\right]^{-1}(z - \beta 1_n) \tag{4.6}$$

to choose $b$. After having determined the hyperparameters predictions can be made using Equation (4.3) and prediction uncertainty estimates are obtained from Equation (4.4).

### 4.3.2 Cokriging

Cokriging is a variant of kriging that enables to combine various sources of data for accurate prediction. A clear description of the method is given in Kennedy & O'Hagan [2000]. In the context of this research only two sources of data are considered. However, the method can easily be extended to multiple data sources. Very often in aerodynamic simulations various codes modeling the same physical process are available, each one having its own level of fidelity. Low fidelity codes are usually cheap to run whereas high fidelity codes are often complex and expensive to run. Combining many data from a low fidelity code and few data from a high fidelity code can result in fast predictions of the process with a higher accuracy then the low fidelity source. Although cokriging is very similar to kriging the full equations will be given here for notational clearness.

#### Autoregressive Model

For each data set $t = 1, 2$, let $D_t$ be the design set consisting of the $n_t$ input points $x_1^{(t)}, \ldots, x_{n_t}^{(t)}$. The output data of each set $z_t^T = \left(z_t\left(x_1^{(t)}\right), \ldots, z_t\left(x_{n_t}^{(t)}\right)\right)$ are combined into the total output data vector $z^T = \left(z_1^T, z_2^T\right)$. The object of inference is the high fidelity process conditional on all the data, i.e. $[z_2|z]$.

Using a kind of Markov property to relate the two data sets, the following assumption about the low fidelity process $z_1$ and the high fidelity process $z_2$ is made

$$\operatorname{cov}\left\{z_2(x), z_1(x')|z_1(x)\right\} = 0$$

for all $x' \neq x$. This assumption implies that given the point $z_1(x)$ no more can be learned about $z_2(x)$ from any other output $z_1(x')$ for all $x' \neq x$. In other words, $z_1$ provides information about $z_2(x)$ only at the same input $x$. Based on the Markov assumption and the notion of stationarity of $z_t(x)$ over the $x$ space for each $t$, an autoregressive model is introduced as

$$z_2(x) = \rho_1 z_1(x) + \delta_2(x), \tag{4.7}$$

where $\rho_1$ is a kind of regression parameter and the discrepancy term $\delta_2$ is independent of the low fidelity process $z_1$. The discrepancy term $\delta_2$ is modeled as a stationary Gaussian process, conditional on the hyperparameters $\beta_2$ and $\sigma_2^2$, with mean $h^T\beta_2$, where $h$ is a vector of regression functions, and covariance function $c_2(x, x') = \text{cov}\{\delta_2(x), \delta_2(x')\}$. The low fidelity process also is modeled as a stationary Gaussian process, conditional on hyperparameters $\beta_1$ and $\sigma_1^2$, and independent of $\delta_2$. For each data set a covariance function is assumed of the form

$$c_t(x, x') = \sigma_t^2 \exp\left\{-\sum_i \frac{1}{2b_{ti}^2}\left(x_i - x_i'\right)^2\right\},$$

where $b_{ti}$ is the correlation distance corresponding to the level $t$ code and to the $i^{\text{th}}$ input variable.

The autoregressive model, Equation (4.7), employs linear regression to predict the output of a system at unevaluated input points based on available outputs.

### Prediction of High Fidelity Process

The probability distribution of the high fidelity data conditional on all the data and the hyperparameters $[z_2|z, \phi]$ is modeled as a Gaussian process. The parameters $\beta$ can be integrated out analytically, but the collection of hyperparameters consisting of $\phi = \left(\sigma_1^2, \sigma_2^2, b_1, b_2, \rho_1\right)$ needs to be specifically estimated. The mean function of the distribution of the high fidelity process is given by

$$m(x) = h'(x)^T\beta + t(x)^T V^{-1}(z - H\beta), \tag{4.8}$$

where

$$h'(x)^T = \left(\rho_1 h(x)^T, h(x)^T\right), \qquad H = \begin{pmatrix} h\left(x_1^{(1)}\right)^T & 0 \\ \vdots & \vdots \\ h\left(x_{n_1}^{(1)}\right)^T & 0 \\ \rho_1 h\left(x_1^{(2)}\right)^T & h\left(x_1^{(2)}\right)^T \\ \vdots & \vdots \\ \rho_1 h\left(x_{n_2}^{(2)}\right)^T & h\left(x_{n_2}^{(2)}\right)^T \end{pmatrix},$$

$$\beta = (\beta_1, \beta_2)^T = \left(H^T V^{-1} H\right)^{-1} H^T V^{-1} z,$$

$$t(x)^T = \mathrm{cov}\left\{z_2(x), z^T\right\} = \left(\rho_1\sigma_1^2 A_1\left(\{x\}, D_1\right), \rho_1^2\sigma_1^2 A_1\left(\{x\}, D_2\right) + \sigma_2^2 A_2\left(\{x\}, D_2\right)\right),$$

The data covariance matrix $V$ is given by

$$V = \begin{pmatrix} \sigma_1^2 A_1\left(D_1, D_1\right) + \epsilon_1 I_{n_1} & \rho_1\sigma_1^2 A_1\left(D_1, D_2\right) \\ \rho_1\sigma_1^2 A_1\left(D_2, D_1\right) & \rho_1^2\sigma_1^2 A_1\left(D_2, D_2\right) + \sigma_2^2 A_2\left(D_2, D_2\right) + \epsilon_2 I_{n_2} \end{pmatrix}.$$

The measurement uncertainty $\epsilon_t$ is put on the diagonal of the data covariance matrix $V$. In order to reduce computation time Cholesky decomposition is applied to the data covariance matrix. The element $i, j$ of the matrix of correlations $A_t\left(D_k, D_l\right)$ between data sets $D_k$ and $D_l$ is given by

$$A_t\left(x_i^{(k)}, x_j^{(l)}\right) = \exp\left\{-\sum_m \frac{1}{2b_{tm}^2}\left(x_{im}^{(k)} - x_{jm}^{(l)}\right)^2\right\}$$

for all $x_i^{(k)} \in D_k$ and $x_j^{(l)} \in D_l$. The covariance function for $[z_2(x)|z, \phi]$ is given by

$$\begin{aligned} \mathrm{cov}\left(x, x'\right) &= \left(\rho_1^2\left(c_1\left(x, x'\right) + \epsilon_1 I_{n_1}\right) + \left(c_2\left(x, x'\right) + \epsilon_2 I_{n_2}\right)\right) - t(x)^T V^{-1} t(x') \\ &\quad + \left(h'(x) - H^T V^{-1} t(x)\right)^T \left(H^T V^{-1} H\right)^{-1} \left(h'(x') - H^T V^{-1} t(x')\right), \end{aligned} \tag{4.9}$$

where $\epsilon_t$ is the output uncertainty for each data set and

$$c_t(x, x') = \sigma_t^2 \exp\left\{-\sum_i \frac{1}{2b_{ti}^2}\left(x_i - x_i'\right)^2\right\}.$$

**Estimation of Hyperparameters**

The hyperparameters $\phi$ can be estimated in a Bayesian way by assuming priors and estimating the posterior or by numerical optimization using the data distribution. The distribution of the data conditional on the hyperparameters $\phi$ can be written as the product

$$p(z|\phi) = p\left(z_2|z_1, \rho_1, b_2, \sigma_2^2\right) p\left(z_1|b_1, \sigma_1^2\right). \tag{4.10}$$

From the Markov property, as discussed earlier, it follows that the hyperparameters $\left(b_1, \sigma_1^2\right)$ can be estimated separately from $\left(\rho_1, b_2, \sigma_2^2\right)$ by maximizing each term in the product (4.10). Using the same derivation as followed for Equation (4.6) it can be shown that $b_1$ can be estimated by minimizing

$$\log\left|\sigma_1^2 A_1\left(D_1, D_1\right) + \epsilon_1 I_{n_1}\right| + \left(z_1 - \beta_1 H_{11}\right)^T \left[\sigma_1^2 A_1\left(D_1, D_1\right) + \epsilon_1 I_{n_1}\right]^{-1} \left(z_1 - \beta_1 H_{11}\right),$$

and $\sigma_1^2$ can be obtained from a MLE as

$$\sigma_1^2 = \frac{\left(z_1 - \beta_1 H_{11}\right)^T \left[A\left(D_1, D_1\right) + \epsilon_1 I_{n_1}\right]\left(z_1 - \beta_1 H_{11}\right)}{n_1}.$$

The hyperparameters of the high fidelity dataset $\rho_1, b_2, \sigma_2^2$ are estimated using $z_2$ and $z_1$ data because the Markov property implies that the parameters depend on both datasets. The hyperparameters $\rho_1, b_2$ are chosen to minimize

$$\log\left|\sigma_2^2 A_2\left(D_2, D_2\right) + \epsilon_2 I_{n_2}\right| + \left(d_2 - \beta_2 H_{22}\right)^T \left[\sigma_2^2 A_2\left(D_2, D_2\right) + \epsilon_2 I_{n_2}\right]^{-1} \left(d_2 - \beta_2 H_{22}\right),$$

and $\sigma_2^2$ is obtained from a MLE as

$$\sigma_2^2 = \frac{(d_2 - \beta_2 H_{22})^T \left[A_2 \left(D_2, D_2\right) + \epsilon_2 I_{n_2}\right] (z_2 - \beta_2 H_{22})}{n_2}.$$

In these equations the difference between the outputs of both datasets is given by $d_2 = z_2 - \rho_1 z_1 \left(D_2\right)$, where $z_1 \left(D_2\right)$ denotes the vector of outputs from $z_1$ at input dataset $D_2$. $z_1 \left(D_2\right)$ can be obtained from either evaluating process $z_1$ or predicting the values using kriging. Furthermore, $H_{ii}$ is the $ii^{\text{th}}$ part of matrix $H$ given by

$$H_{ii} = \left(h\left(x_1^{(i)}\right), \ldots, h\left(x_{n_i}^{(i)}\right)\right)^T.$$

Once the hyperparameters are found, cokriging predictions can be performed to obtain interpolated values.

### 4.3.3 Simple Cokriging Example

The capabilities of cokriging compared to kriging can be shown by a simple example. Cokriging is performed on an analytic function $y = f(x)$ given by

$$f\left(x\right) = x \cos\left(\frac{1}{2}x\right) - \sin\left(2x\right).$$

This function is employed to generate the low fidelity data $D_{lf}$ and high fidelity data $D_{hf}$. Low fidelity data is obtained from function $f\left(x\right)$ by adding a discrepancy term $\delta\left(x\right) = 3 - \frac{1}{2}x$ and introducing noise with a standard deviation $\sigma_{lf}$. The distribution for the low fidelity data can be written as

$$D_{lf} \sim N\left(f\left(x\right) + \delta\left(x\right), \sigma_{lf}\right), \qquad \sigma_{lf} = 0.3$$

where $N\left(\cdot, \cdot\right)$ refers to a normal distribution. High fidelity data is obtained from function $f\left(x\right)$ by introducing noise with a standard deviation $\sigma_{hf}$ as

$$D_{hf} \sim N\left(f\left(x\right), \sigma_{hf}\right), \qquad \sigma_{hf} = 0.01.$$

Usually high fidelity model evaluations are expensive, therefore few high fidelity data is available. Since low fidelity models are usually cheap to evaluate many low fidelity data is available. Kriging is applied using only the high fidelity data and cokriging using both the low fidelity dataset and the high fidelity dataset. The results are presented in Figure 4.1. Figure 4.1a shows clearly that kriging using the high fidelity data yields predictions that do not follow the original function $f\left(x\right)$. However, applying cokriging to the noisy low fidelity data and the accurate but few high fidelity data improves the prediction considerably, see Figure 4.1b. The cokriging prediction follows very accurately the analytic function $f\left(x\right)$. This simple example shows clearly the capabilities of the cokriging method by using few expensive high fidelity data and many cheap low fidelity data to obtain accurate predictions.

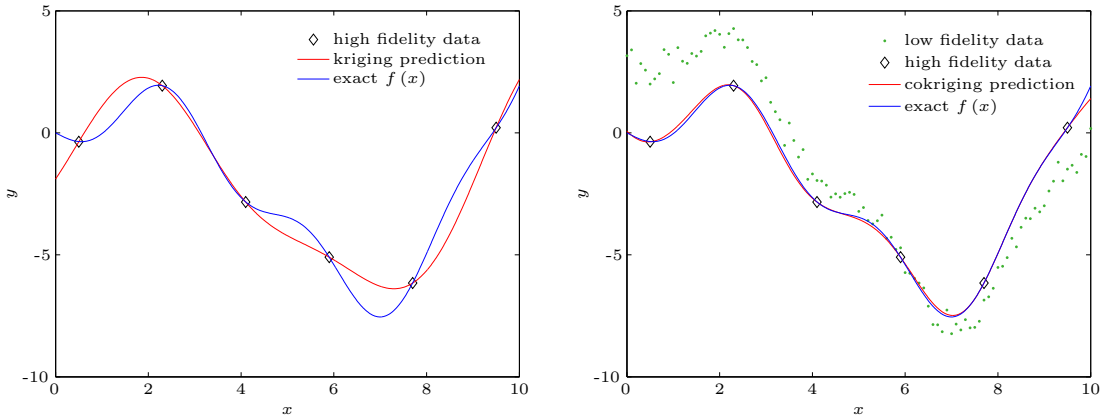


(a) Kriging of high fidelity data.

(b) Cokriging of low fidelity and high fidelity data.

**Figure 4.1:** Comparison of the application of kriging and cokriging to a simple analytic function.

## 4.4 Probabilistic Collocation

The probabilistic collocation (PC) method is a non-intrusive Polynomial Chaos method that can be used for the propagation of uncertainties. The PC method employs polynomial chaos expansions to model the solution of each output variable depending on the uncertain inputs. Polynomial chaos expansions are constructed based on Lagrange polynomials. The Lagrange interpolating polynomials pass through collocation points, which correspond to the Gauss quadrature points. The Gauss quadrature points are based on the probability distributions of the uncertain parameters. Exact solutions are obtained by performing deterministic runs at the collocations points. The result of PC is an approximating distribution function of the solution. Approximations of the mean and variance as well as sensitivity measures can be obtained by integration of the solution. The PC approach used here is mainly taken from work of Loeven & Bijl [2008] and Loeven [2010].

### 4.4.1 Polynomial Chaos Expansion

The solution is modeled using polynomial chaos expansions by

$$u(\boldsymbol{x},\omega) \approx \sum_{i=1}^{N_p} u_i(\boldsymbol{x})\, L_i(\boldsymbol{\xi}(\omega)), \tag{4.11}$$

where the solution $u(\boldsymbol{x},\omega)$ is a function of inputs $\boldsymbol{x}$ and the random event $\omega \in \Omega$, and $N_p$ is the number of collocation points. Furthermore, $u_i(\boldsymbol{x})$ is the solution $u(\boldsymbol{x},\omega)$ at collocation point $\omega_i$ obtained by a deterministic run, $L_i$ is the Lagrange interpolating polynomial chaos corresponding to the collocation point $\omega_i$ and $\boldsymbol{\xi}$ is the multidimensional random basis $\boldsymbol{\xi} = \{\xi^1, \ldots, \xi^n\}$ for $n$ uncertain parameters. The Lagrange interpolating polynomial is a function in terms of the random variable $\boldsymbol{\xi}(\omega)$, which is chosen to be

uniformly distributed, i.e. $\boldsymbol{\xi}(\omega) = U(-1,1)$, such that the uncertain input parameter $\boldsymbol{a}(\omega)$ is a linear transformation of $\boldsymbol{\xi}(\omega)$. The Lagrange polynomial chaoses are given by

$$L_i\left(\boldsymbol{\xi}\left(\omega\right)\right) = \prod_{j=1, j\neq i}^{N_p} \frac{\boldsymbol{\xi}\left(\omega\right) - \boldsymbol{\xi}\left(\omega_j\right)}{\boldsymbol{\xi}\left(\omega_i\right) - \boldsymbol{\xi}\left(\omega_j\right)}, \tag{4.12}$$

with $L_i\left(\boldsymbol{\xi}\left(\omega_j\right)\right) = \delta_{ij}$. The Lagrange interpolating polynomial chaos $L_i\left(\boldsymbol{\xi}\left(\omega\right)\right)$ passes through the $N_p$ collocation points. The collocation points correspond to the Gauss quadrature points used to integrate the function $u\left(\boldsymbol{x}, \omega\right)$ in the $\omega$ domain.

### 4.4.2 Collocation Points

The collocation points are computed for each uncertain parameter $\xi^j, j = 1, \ldots, n$ separately in one-dimensional space. The collocation points for multiple uncertain parameters are obtained from tensor products of one-dimensional collocation points. For notational convenience the index $j$ will be dropped from here on. The total number of collocation points $N_p$ for $n$ uncertain parameters becomes $N_p = (p+1)^n$ for an order $p$ PC approximation. At each collocation point a deterministic solve is required, implying $N_p$ solves.

The method to find suitable collocation points and corresponding weights makes use of the Golub-Welsch algorithm, which is developed by Golub & Welsch [1969]. This algorithm requires the recurrence coefficients of polynomials that are orthogonal with respect to the weighting function $w\left(\xi\right)$ of the integration. The recurrence coefficients are computed using the discretized Stieltjes procedure.

Orthogonal polynomials with respect to the weighting function of the element are constructed in each element using the recurrence relation

$$\begin{aligned} \Psi_0\left(\xi\right) &= 0, \qquad \Psi_1\left(\xi\right) = 1, \\ \Psi_{i+1}\left(\xi\right) &= \left(\xi - \alpha_i\right)\Psi_i\left(\xi\right) - \beta_i \Psi_{i-1}, \qquad i = 2, \ldots, N_p. \end{aligned} \tag{4.13}$$

The recurrence coefficients $\alpha_i$ and $\beta_i$ are determined by the weighting function $w\left(\xi\right)$ and $\left\{\Psi\left(\xi\right)\right\}_{i=1}^{N_p}$ is a set of orthogonal polynomials with $\Psi_i\left(\xi\right) = \left(\xi\right)^i + \mathcal{O}\left(\left(\xi\right)^{i-1}\right)$, $i = 1, \ldots, N_p$. The recurrence coefficients are computed as

$$\alpha_i = \frac{\left(\xi\Psi_i, \Psi_i\right)}{\left(\Psi_i, \Psi_i\right)} \qquad i = 1, \ldots, N_p, \tag{4.14}$$

$$\beta_i = \frac{\left(\Psi_i, \Psi_i\right)}{\left(\Psi_{i-1}, \Psi_{i-1}\right)} \qquad i = 2, \ldots, N_p, \tag{4.15}$$

where $(\cdot, \cdot)$ denotes an inner product defined by

$$\left(f\left(\xi\right), g\left(\xi\right)\right) = \int f\left(\xi\right) g\left(\xi\right) w\left(\xi\right) d\xi. \tag{4.16}$$

The obtained recurrence coefficients form the inputs of the Golub-Welsch algorithm to compute the collocation points $\xi_i$ and corresponding weights $w_i$. From the recurrence

coefficients a Jacobi matrix is constructed as

$$J = \begin{bmatrix} \alpha_1 & \sqrt{\beta_2} & & & \phi \\ \sqrt{\beta_2} & \alpha_2 & \sqrt{\beta_3} & & \\ & \ddots & \ddots & \ddots & \\ & & \sqrt{\beta_{N_p-1}} & \alpha_{N_p-1} & \sqrt{\beta_{N_p}} \\ \phi & & & \sqrt{\beta_{N_p}} & \alpha_{N_p} \end{bmatrix}. \tag{4.17}$$

The collocation points $\xi_i$, $i = 1, \ldots, N_p$ are the eigenvalues of the Jacobi matrix $J$. The weights are found by $w_i = \beta_1 v_{1,i}^2$, $i = 1, \ldots, N_p$, where $v_{1,i}$ is the first component of the normalized eigenvector corresponding to eigenvalue $\xi_i$. The collocation points $\xi_i$ are mapped from the $\xi$-domain to the $\omega$-domain using the probability distribution of $\xi$ as

$$\omega_i = F_\xi\left(\xi_i\right), \qquad i = 1, \ldots, N_p.$$

For multiple uncertain parameters the collocation points are obtained using tensor products of the one-dimensional vectors containing the collocation points of each $\omega$. The corresponding weights are found by using tensor products similar as for the collocation points. After applying the tensor products a $N_p \times n$-matrix can be made of the collocation points, where each row $i$ corresponds to collocation point $\omega_i$, and a $N_p$-vector of weights $w_i$. Note that now a new ordering is adopted such that the index $i$ refers to a different ordering.

### 4.4.3 Uncertainty Analysis

The main output of interest is the expansion of the solution in the $\omega$ domain. The PC expansion of the random variable $u$ is written as

$$u\left(\boldsymbol{x}, \omega\right) \approx \sum_{i=1}^{N_p} u_i\left(\boldsymbol{x}\right) L_i\left(\boldsymbol{\xi}\left(\omega\right)\right), \tag{4.18}$$

where $u_i\left(\boldsymbol{x}\right)$ is the output at collocation point $\omega_i$ and obtained from a deterministic computation. The output variable $u$ can for example be the lift coefficient or the drag, which are random variables due to uncertain input variables such as the angle of attack or the flap angle. The mean and variance of the solution are found by

$$\begin{aligned} \mu_u &= \sum_{i=1}^{N_p} u_i(\boldsymbol{x}) w_i, \\ \sigma_u^2 &= \sum_{i=1}^{N_p} (u_i(\boldsymbol{x}))^2 w_i - \left( \sum_{i=1}^{N_p} u_i(\boldsymbol{x}) w_i \right)^2. \end{aligned}$$

where $w_i$ are the weights corresponding to the collocation points $\omega_i$. When multiple uncertain parameters are included, the mean and variance indicate the total combined effect of all uncertain parameters.

### 4.4.4 Sensitivity Analysis

Probabilistic collocation offers possibilities for sensitivity analysis of an output variable to the various uncertain input parameters. The procedure described here makes use of independent distributions on the input parameters, or marginalized distributions in case of dependent input parameters. Sensitivity analysis can be used to select the most important parameters out of the complete set of uncertain parameters. The efficiency of PC uncertainty analyses can be greatly increased when reducing the amount of uncertain parameters to only the most important ones.

The sensitivity derivative is defined as the partial derivative of the solution $u(\boldsymbol{x}, \omega)$ with respect to the uncertain parameter $a(\omega)$. The approximation of the derivative is obtained from differentiation of the polynomial chaos expansions of the solution, Equation (4.18), with respect to $\xi(\omega)$ yielding

$$\frac{\partial u\left(\boldsymbol{x}\right)}{\partial \xi} \approx \sum_{i=1}^{N_p} u_i\left(\boldsymbol{x}\right) \frac{\partial L_i\left(\xi\left(\omega\right)\right)}{\partial \xi},$$

where $N_p = p+1$, $p$ is the order of the approximation. For a second order approximation, i.e. $N_p = 3$, the partial derivative can be written as

$$\begin{aligned}
\frac{\partial u(\boldsymbol{x})}{\partial \xi} \quad = \quad & u_1(\boldsymbol{x}) \left\{ \frac{\xi\left(\omega_2\right) - \xi\left(\omega_3\right)}{\left(\xi\left(\omega_1\right) - \xi\left(\omega_2\right)\right)\left(\xi\left(\omega_1\right) - \xi\left(\omega_3\right)\right)} \right\} + \\
& u_2(\boldsymbol{x}) \left\{ \frac{2\xi\left(\omega_2\right) - \xi\left(\omega_1\right) - \xi\left(\omega_3\right)}{\left(\xi\left(\omega_2\right) - \xi\left(\omega_1\right)\right)\left(\xi\left(\omega_2\right) - \xi\left(\omega_3\right)\right)} \right\} + \\
& u_3(\boldsymbol{x}) \left\{ \frac{\xi\left(\omega_2\right) - \xi\left(\omega_1\right)}{\left(\xi\left(\omega_3\right) - \xi\left(\omega_1\right)\right)\left(\xi\left(\omega_3\right) - \xi\left(\omega_2\right)\right)} \right\},
\end{aligned}$$

where $u_i(\boldsymbol{x})$ indicates the $i^{\text{th}}$ collocation point for uncertain parameter $a$ or random variable $\xi$. The uncertain parameter $a$ is related to the random variable $\xi$ via a linear transformation as

$$a = A_a \xi + B_a, \tag{4.19}$$

with constants $A_a$ and $B_a$. Using Equation (4.19) the sensitivity derivative of the solution with respect to uncertain parameter $a$ can be written as

$$\frac{\partial u(\boldsymbol{x})}{\partial a} = \frac{\partial u(\boldsymbol{x})}{\partial \xi}\frac{\partial \xi}{\partial a} = \frac{1}{A_a}\frac{\partial u(\boldsymbol{x})}{\partial \xi}.$$

A comparison between the sensitivity derivatives for the most important uncertain parameters can be made using the scaled sensitivity derivative. The scaled derivative is obtained by multiplying the derivative of the solution with respect to parameter $a$ with the corresponding standard deviation $\sigma_a$. Since only independent input parameters will be regarded during the sensitivity analysis combined sensitivity derivatives will not be given. The scaled sensitivity derivative $\widehat{\frac{\partial u}{\partial a}}$ is given by

$$\widehat{\frac{\partial u}{\partial a}} = \sigma_a \frac{\partial u}{\partial a}.$$

The most important parameters can easily be determined by selecting the largest scaled derivatives. Note that the scaled derivative refers to linear influences of the input parameters on the output variables. The possibility exists that a parameter has a small scaled derivative but a large influence due to quadratic effects.

### 4.4.5 PC Approximation Convergence Study

Before performing a full probabilistic collocation study, a convergence study is needed to determine the desired order of approximation $p$. The convergence study consists of computing the approximation error for various orders of approximation and choosing an appropriate approximation order using the resulting error outputs.

The approximation error is estimated with respect to a high order approximation. The estimated error of the approximated variable $u$ for a $p^{\text{th}}$ order approximation is computed by

$$\epsilon_u = \frac{\sqrt{\sum_{i=1}^{N_{pa}} w_i \left(\hat{u}_i - u_i^{p_a}\right)^2}}{\sum_{i=1}^{N_{pa}} w_i u_i^{p_a}}, \tag{4.20}$$

where $N_{p_a}$ is the number of collocation points, $u_i^{p_a}$ are the results of deterministic solves for the variable at the collocation points, all corresponding to a $(p_a)^{\text{th}}$ order approximation. The $\hat{u}_i$ are the approximated values at the collocation points of the $(p_a)^{\text{th}}$ order approximation using a $p^{\text{th}}$ order approximation. Usually the accurate approximation of order $p_a$ is one order higher than the highest order approximation for which the error is estimated.

## 4.5 Markov Chain Monte Carlo Method

Monte Carlo methods are a class of widely applied integration methods. The Markov chain Monte Carlo (McMC) method is an extension to the basic Monte Carlo method. McMC combines advanced sampling techniques with the relatively simple Monte Carlo principle. This method is especially useful for Bayesian inference techniques to explore complex posterior distributions.

### 4.5.1 Monte Carlo Principle

For complex multivariate functions it is often difficult to obtain a direct expression of the response as a function of the output. Monte Carlo methods especially can be used to explore the output distribution of a complex function. Monte Carlo methods depend on a large number of function evaluations over a range of inputs. A detailed discussion of Monte Carlo methods is given in Liang et al. [2010]. The basics of the method can be summarized in a four step approach:

1. The domain of interest of the complex function inputs is defined and probability distributions are specified on the input variables.

2. A large number of input sets is generated from the probability distribution by a computer based random generator.

3. Deterministic runs of the complex function are made at the input sets to obtain realizations at the randomly chosen points from the input space.

4. The outputs of the function realizations are collected and inferences can be made on the outputs. As an example, a response surface can be fitted to the outputs or inferences about the probability distribution can be made, depending on the application.

The fact that a large number of computer code realizations is required for Monte Carlo methods limits the applicability to relatively low cost computer codes. Extensions of the basic Monte Carlo method are available to increase efficiency and applicability of the method.

### 4.5.2 Markov Chains and the Metropolis Hastings Algorithm

The basic Monte Carlo approach generally requires a large number of realizations to approximate a complex output distribution. In order to reduce computation time and increase efficiency more sophisticated sampling methods can be used. Markov chains can be employed to obtain increased efficiency by sampling from the posterior distribution instead of a chosen input distribution.

Markov chain Monte Carlo methods employ the Markov property to construct a Markov chain by sampling from probability distributions. The Markov property implies that given a present state, the future state only depends on the present state and is independent of all past states. A Markov chain is a sequence of random variables constructed using the Markov property.

A two-step approach to construct reversible Markov chains is proposed by Metropolis et al. [1953] and generalized by Hastings [1970]. The first step of this algorithm consists of specifying a proposal distribution with probability density function $q(y|x)$. In Metropolis' approach this proposal distribution has to be symmetric, but Hastings generalized the method to include asymmetric proposal distributions. Starting from a chosen initial distribution the subsequent samples $y$ are drawn from the proposal distribution $q(y|x)$. In the second step the draws from $q(y|x)$ are either accepted or rejected using the output of the posterior distribution $f$, such that the resulting Markov chain is reversible. The acceptance ratio is defined as

$$\alpha(x_t, y) = \min\left\{1, \frac{f(y)q(x_t|y)}{f(x_t)q(y|x_t)}\right\}. \tag{4.21}$$

The new sample $x_{t+1}$ is set to $y$ with probability $\alpha(x_t, y)$, and $x_{t+1} = x_t$ with the remaining probability $1 - \alpha(x_t, y)$. Practically this means that the acceptance ratio is compared to a sample $U$ that is drawn from the uniform $(0, 1)$ distribution. If $U \leq \alpha(x_t, y)$ the future sample is set to $x_{t+1} = y$, otherwise the future sample is set to the present sample, i.e. $x_{t+1} = x_t$.

In practical applications the data vector is large and the output of posterior distributions is often very small. In order to stay within the computational range of MATLAB in this thesis the logarithm of the posterior distribution is used. When working with the logarithm of the posterior distribution, the Metropolis Hastings ratio, Equation (4.21), changes to

$$\alpha(x_t, y) = \min\left\{1, \exp\left[(\log f(y) + \log q(x_t|y)) - (\log f(x_t) + \log q(y|x_t))\right]\right\}. \tag{4.22}$$

The initial distribution will often not be part of the stationary target distribution. In order to make inferences about the target distribution, the first part of the Markov chain has to be discarded since it is not part of the equilibrium distribution. Discarding the portion of the chain that is not part of the stationary target distribution is called burn in. Determination of the burn in size is usually done by expert knowledge or by examining the current results of the Markov chain. A straightforward approach is to plot the curves of the variables in the chain and determine the stage where the samples are part of a stationary distribution.

# Chapter 5

# Model of the Wing Geometry

Uncertainty quantification deals with propagating input uncertainty distributions through a simulator to obtain output uncertainty characteristics. Prior to the uncertainty quantification the input uncertainty distributions need to be defined. Many input variables are present in the experiment. The wing geometry is believed to be one of the major influential uncertain inputs.

Due to inaccurate manufacturing practices the wing geometry deviates from the design profile DU96W180. The feeling is that the geometric variations introduce discrepancies between experimental observations and simulations of the DU96W180 profile. In order to increase understanding about the influence of geometric deviations from the design geometry, measurements of the wing are performed and a three-dimensional model is obtained.

Initially geometric measurements are performed by a Coordinate Measuring Machine (CMM) as discussed in section 5.1. Due to improper use of the measuring equipment large uncertainties are introduced in these measurements. In order to improve on the CMM results, additional measurements are performed using a photogrammetry technique, see section 5.2. Section 5.3 describes that by combining information from both data sources using cokriging, accurate knowledge is obtained about the geometry of the wing.

## 5.1 CMM Geometry Measurements

Geometric measurements are initially performed using a Coordinate Measuring Machine to obtain seven two-dimensional profiles at various spanwise locations. Section 5.1.1 discusses the measurement procedure followed. Considerable work has been done to the raw measurements to obtain useful geometric data. Section 5.1.2 describes the transformation that is applied to the data and section 5.1.3 discusses the errors present in the CMM data.

### 5.1.1 Measurement Procedure

Geometrical measurements are performed using a Coordinate Measuring Machine of type Mitutoyo BH706, see Figure 5.1. The wing is laid down on a granite measuring table and clamped in order to prevent movement. A downward pointing probe scans the airfoil with a ball at the end that touches the surface. The diameter of the touching ball is 10.961 mm. The probe is attached to an arm that can move both horizontally and vertically. The arm is moved along the airfoil surface by manual action. The measurement unit on itself provides a resolution of 0.005 mm and an accuracy of 0.01 mm. However, the most important errors are caused by movement of the wing and flap and by the fact that the pressure and suction side of the wing are measured separately. These errors are in the order of a millimeter.

### 5.1.2 Transformation of the CMM Measurements


**Figure 5.1:** Coordinate Measuring Machine Mitutoyo BH706.

At seven spanwise locations a profile is measured in the chordwise direction. For each measurement point the location of the center of the ball is recorded. Usually CAD software corrects the data for the ball radius. However, due to improper functioning of the CMM software the measurements are not corrected for the ball radius. Therefore the ball radius correction is performed within MATLAB by translating the coordinate data over a distance equal to the ball radius in the direction normal to the surface. For each coordinate point the angle is computed using consecutive data points in the chordwise direction. Due to the fact that the data resolution is higher than the accuracy, the data is noisy. In order to obtain a smoothly varying angle the data are smoothed prior to calculating the correction angle. Except for coordinates near the airfoil leading edge and trailing edge the ball radius corrections yield a profile that corresponds to the DU96W180 profile. Because of the fact that the angle varies a lot near the leading and trailing edge, the smoothing introduces errors in these regions.

The separately obtained measurements of the suction and pressure side lack a common reference. The profiles of the suction and pressure side need to be combined to obtain full two-dimensional profiles. Assuming that the thickness of the measured profiles is equal to the thickness of the DU96W180 profile, the suction and pressure sides are combined. The

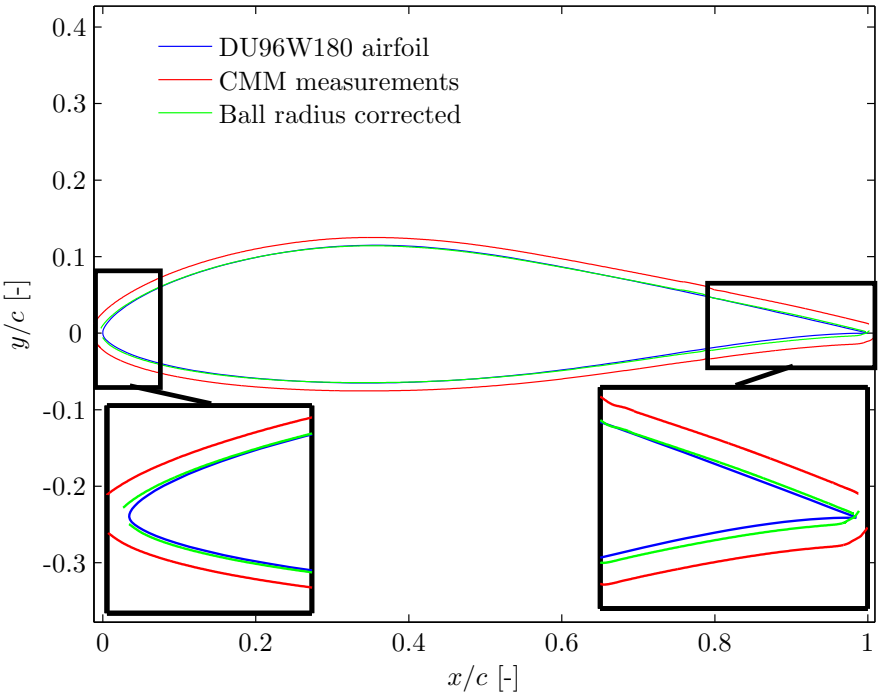


**Figure 5.2:** Comparison of the geometrical measurement of the Coordinate Measuring Machine with the DU96W180 profile. The raw data and the corrected data are shown separately.

measurement data are scaled, translated and rotated such that the measured profiles lie as good as possible on top of the DU96W180 profile. The scaling is performed by using the ratio of chord lines of the measurements and the DU96W180 profile. Careful inspection of the measurement data has shown that the chord line of the measurements amounts to 505 mm. The translation distance and rotation angle are computed by using numerical minimization of the total distance between the measurements and the DU96W180 profile. Translations and rotations are applied to the profiles of the suction and pressure side separately. The results of the ball radius correction, the scaling, translation and rotation are shown in Figure 5.2 together with the DU96W180 profile. The discrepancy between the measurements and the DU96W180 profile are largest in the leading edge and trailing edge region.

### 5.1.3 Measurement Errors

As stated above, uncertainties are introduced in the measurements by possible movement of the wing and the flap. The most important error however is introduced by the fact that the suction and pressure sides of the wing are measured separately. The assumption of equal thickness between measured profiles and DU96W180 profile introduces considerable uncertainty in the geometrical data. Furthermore, the accuracy at the leading and trailing edge is limited because it is difficult to attach the probe to and from the surface. Based on careful inspection of the results, the uncertainty of the CMM measurements is estimated as 0.25 mm.

## 5.2 Photogrammetry Measurements

Since the CMM measurements are subject to large errors additional measurements are performed using a technique called photogrammetry. The measurement procedure is explained in section 5.2.1 and the measurement errors are discussed in section 5.2.2. The photogrammetry results are mapped in such a way that they are easily comparable with the coordinates of the DU96W180 profile, see section 5.2.3.

### 5.2.1 Measurement Procedure

Photogrammetry makes use of two-dimensional pictures to reconstruct the three-dimensional geometry of an object. The camera used during the measurements is a Nicon D90 and the software used for the analysis is Photomodeler Scanner v6.2. Prior to taking the pictures, the wing is marked with many yellow markers that can easily be recognized on pictures, see Figure 5.3. In order to be able to identify common markers between pictures taken from the pressure and suction side, marker lines are put in front of the leading edge and behind the trailing edge. These additional marker lines enable to relate coordinates from the pressure side accurately to coordinates from the suction side. In total 44 pictures were required to be able to reconstruct the geometry by this technique.

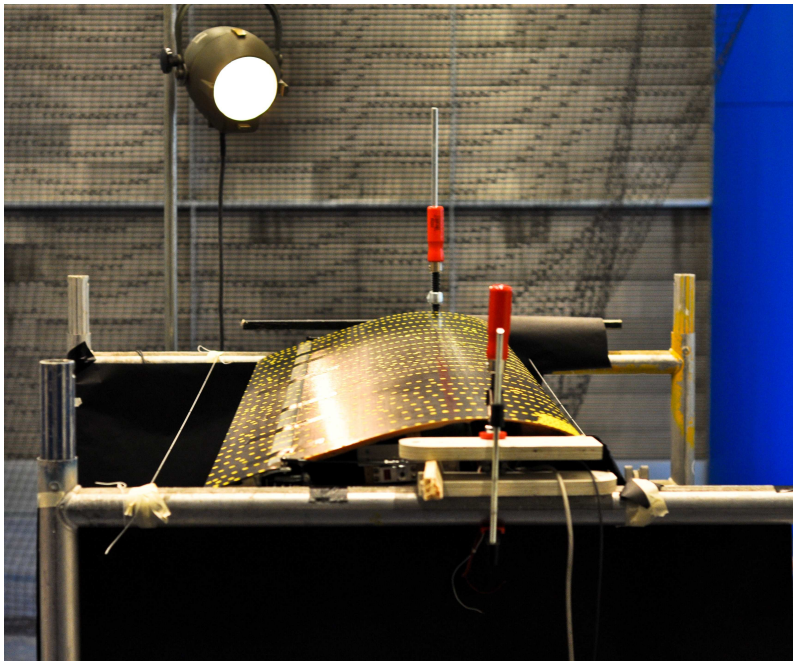

**Figure 5.3:** Wing object marked with stickers for photogrammetry.

The procedure to perform photogrammetry can be broken down into four steps. The first step of the technique consists of the determination of the internal orientation of the camera through calibration. The internal orientation is described by parameters such as the focal length and lens distortion coefficients. During the second step the external orientation is determined by manually pointing 6 identical points on different pictures.

The identical points need to be common to at least two different pictures. This results in the position and rotation of the camera for every picture with respect to the object. The relationship between coordinates in the pictures and object coordinates is obtained from the internal and external orientation by making use of collinearity equations. The third step is called feature detection and consists of automatic detection of the markers. The last step comprises matching of corresponding markers to each other. This process is called feature matching. The features that are matched are finally assembled to reconstruct the three-dimensional object.

### 5.2.2 Measurement Errors

The main uncertainty of the measurements originates from inaccuracy in the determination of the internal and external orientation. This uncertainty becomes clear in the feature detection and matching process, i.e. relating the various marker points in pictures to each other and constructing three-dimensional coordinates. The process of identifying the midpoints of the markers is believed to be relatively accurate. Additional to the three-dimensional coordinates the program outputs the largest residual and the root mean square of the residual for each coordinate point. The marking residual is the difference between the projection of the calculated three-dimensional coordinate of a point on a picture and the actual position of the point in the picture. The measurement uncertainty is calculated as the sum of the average largest residual and the average root mean square of the residual of all points. After conversion from pixels to millimeters the uncertainty amounts to 0.17 mm.

### 5.2.3 Mapping of the Photogrammetry Results

The result of the photogrammetry measurements is a cloud of coordinates in three-dimensional space. In order to compare it with the DU96W180 profile, the data need to be scaled, translated and rotated. Because the wing is a structured object, principal component analysis (PCA) is employed to determine the principal axes of the object. PCA refers to a mathematical procedure that uses an orthogonal transformation to convert a set of observations of possibly correlated variables into a set of values of uncorrelated variables called principal components. The principles of the PCA procedure have initially been developed by Pearson [1901]. The wing is rotated using the coefficients of the principal component analysis and manual fine tuning afterwards. The translation towards the two-dimensional DU96W180 airfoil and a small rotation around the spanwise axis is performed using numerical minimization of the distance between coordinates of the DU96W180 airfoil and coordinates of the measured airfoil in two dimensions. During this minimization the flap region is excluded to obtain a proper fit of the pressure and suction side of the wing to the coordinates of the DU96W180 airfoil in this region. The result is shown in Figure 5.4 together with the DU96W180 airfoil. Note that especially in the flap region the measurements show that there is an offset in flap angle. Furthermore the profile is thicker in the flap region than the DU96W180 profile. This effect is also visible in the CMM measurement shown in Figure 5.2. Since only mapping is applied to the photogrammetry results, no additional error is introduced by the mapping step.

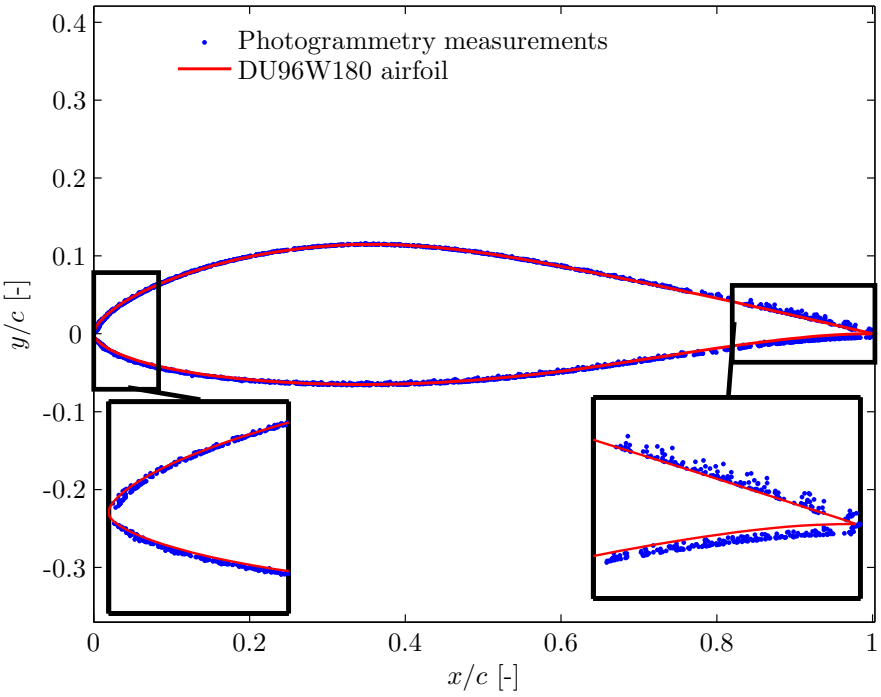


**Figure 5.4:** Comparison of the photogrammetry measurements with the DU96W180 profile in two dimensions.

## 5.3 Wing model

The CMM and photogrammetry measurements of the geometry are combined to obtain an accurate geometric model of the wing using cokriging, see section 4.3.2. The CMM measurements act as a low fidelity data source and the photogrammetry measurements as a high fidelity data source. The uncertainty of each data set is taken into account. The measurement data from both measurements are combined and shown in Figure 5.5.

### 5.3.1 Kriging profiles

Applying cokriging to the data in Cartesian coordinates would yield two problems. One problem is that cokriging has difficulty with handling large gradients, which are present at the leading edge. Another problem is that for each coordinate along the chord line there is a point on the upper and on the lower surface of the airfoil. This means that cokriging should be done on the upper and lower surface separately. Therefore, a coordinate transformation is employed to circumvent these problems. The coordinate transformation consists of scaling and transformation to polar coordinates. Scaling is performed by multiplying the coordinate running in the airfoil thickness direction with a factor of 6 such that the airfoil shape approximates a circle. This shape is transformed into polar coordinates yielding a three-dimensional surface with the angle $\theta$, radius $r$ and spanwise $z$ coordinates. This surface is suitable for cokriging since there are no high gradients present and for each $\theta$ and $z$ coordinate point there is only one unique $r$ coordinate on

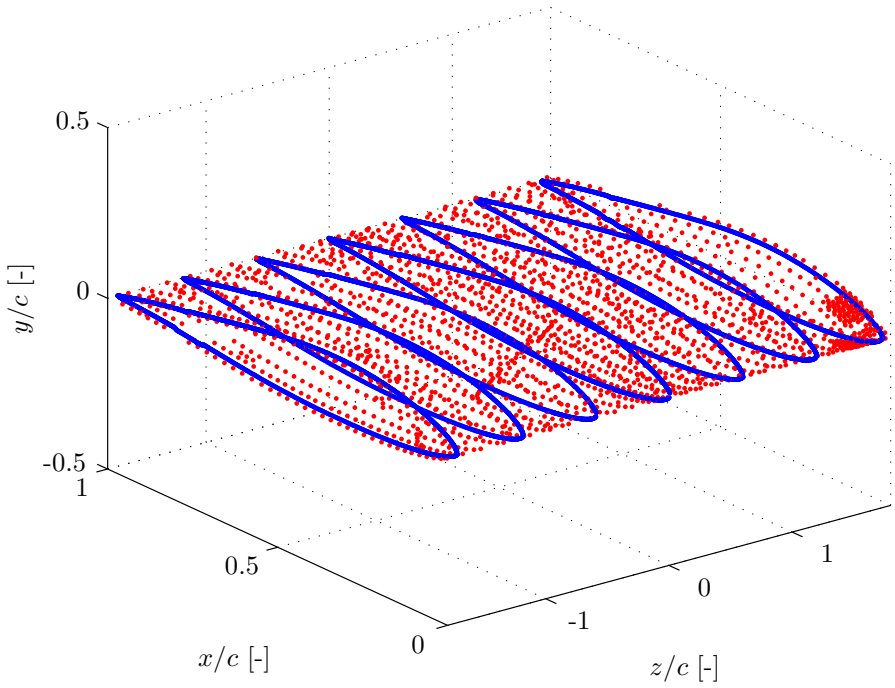


**Figure 5.5:** CMM measurement data (blue dots) and photogrammetry measurement data (red dots) of the three-dimensional wing geometry.

the surface.

Cokriging is applied to the surface in polar coordinates employing the DU96W180 profile as the mean function $h(x)$ in equations (4.3) and (4.8) of section 4.3.2. In order to be able to compare easily with the design geometry, the three-dimensional wing geometry is modeled as 35 two-dimensional profiles in the spanwise or $z$-coordinate direction with $z$ coordinates $z_i = -1.7, -1.6, \ldots, 1.7$, see Figure 5.6. The $\theta$ coordinates for these profiles are obtained from the DU96W180 profile. For each two-dimensional profile an uncertainty covariance matrix is available that represents the uncertainty resulting from the cokriging prediction. Each of these profiles can be used as an input for XFOIL to perform aerodynamic computations.

### 5.3.2 Mean 2D Profile Distribution

In order to compare the measured wing geometry well with the DU96W180 profile the three-dimensional wing needs to be transformed into a two-dimensional airfoil distribution. A straightforward and simple approach is to use Monte Carlo approximation. At 35 locations, which are distributed along the wingspan, a sufficiently large amount of samples is generated from the cokriging Gaussian model to represent the airfoil distribution. The amount of samples is determined by investigating the error between the mean and variance of the airfoil distribution and the sample mean and variance of the generated profiles. Taking into account computational limits the amount of samples is determined as 2500.

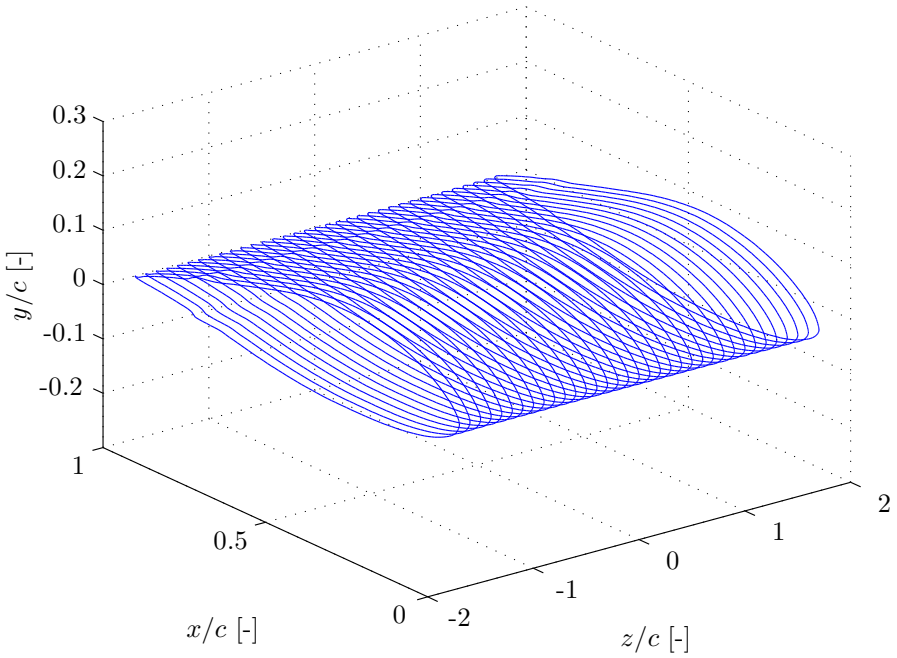


**Figure 5.6:** Airfoil profiles resulting from cokriging of the CMM and photogrammetry data.

At the 35 spanwise locations 2500 random airfoil samples are generated and the sample mean and covariance matrix are obtained from the collection of $35 \times 2500$ samples in total. In this way an average airfoil profile is obtained and a covariance matrix that represents both the cokriging uncertainty at the 35 spanwise locations and the geometric variation along the wing span.

A comparison of the DU96W180 profile and the mean 2D profile is shown in Figure 5.7. The leading edge region and the flap region clearly show discrepancies between the two profiles. Figure 5.8 shows the mean 2D profile including the total geometric uncertainty. The geometric uncertainty is computed by taking the square root of the diagonal of the covariance matrix. At the suction side the geometric uncertainty is relatively large in the middle and flap region. At the pressure side the geometric uncertainty is largest in the middle region. The fact that the uncertainty is large in these regions is mainly due to spanwise variations, which are now included in the geometric variance. The maximum distance between coordinates of the DU96W180 profile and the mean 2D profile amounts to 4.6 mm and is found in the flap region on the pressure side. Furthermore the largest geometric uncertainty amounts to 0.95 mm and is found in the middle of the pressure side of the airfoil.

The transformation from the three-dimensional wing, which is described in 35 two-dimensional profiles along the wing span, to a two-dimensional distribution might be problematic. The lift coefficient of the three-dimensional wing might be different from the lift coefficient of the two-dimensional mean profile. In order to assess this problem a comparison is made between the $c_l - \alpha$ curve of the mean profile and the $c_l - \alpha$ curves of the 35 profiles. Since the geometry has only an influence on the XFOIL outputs and not directly on the corrections, no corrections are applied to these data. The sample mean

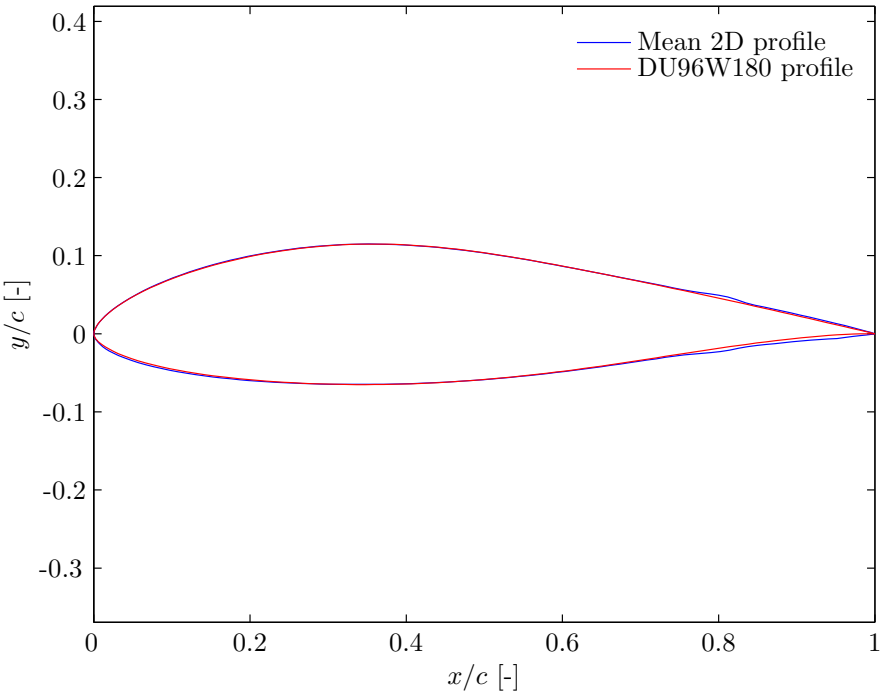


**Figure 5.7:** Comparison of the mean 2D profile and the DU96W180 profile.

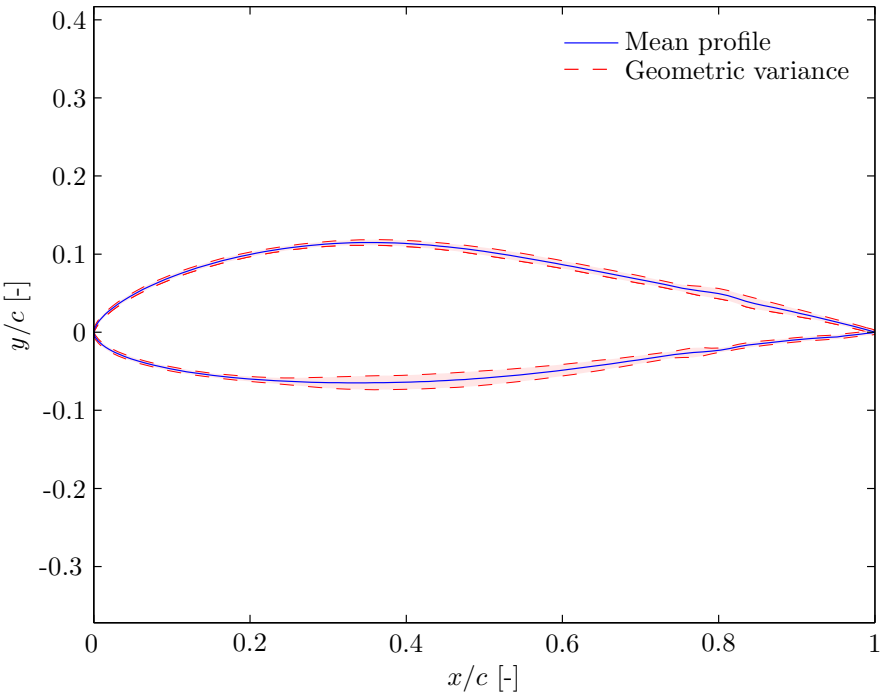


**Figure 5.8:** The mean two-dimensional profile shown together with its geometrical uncertainty. The uncertainty interval corresponds to the standard deviation multiplied with a factor of 10.

and variance are computed from the $c_l - \alpha$ curves of the 35 airfoil profiles. Figure 5.9 shows that there is a reasonably good agreement between the two curves. This indicates that it is reasonable to use the mean airfoil profile as a two-dimensional approximation of the three-dimensional wing.

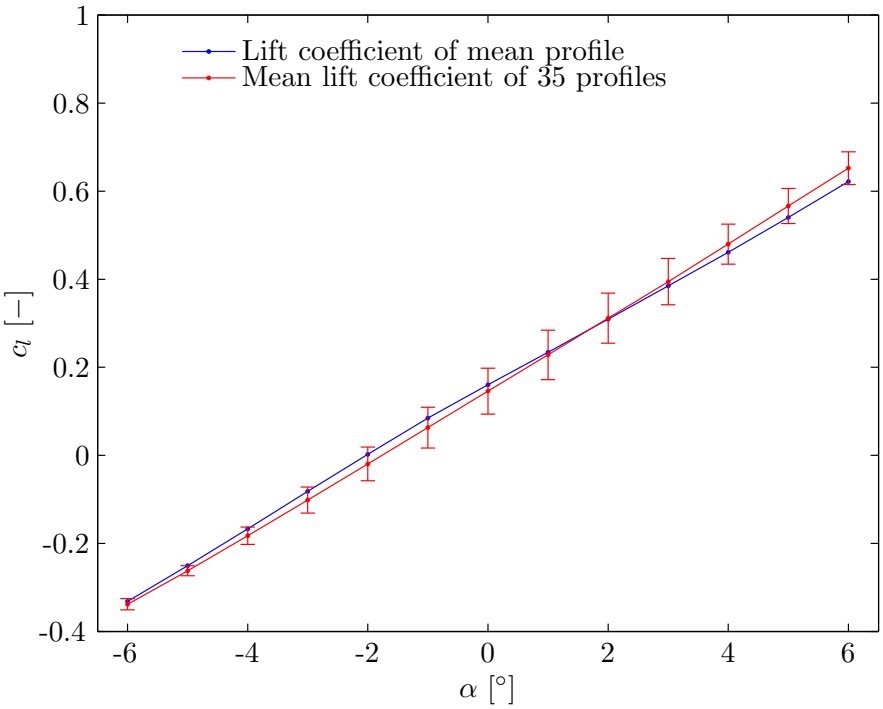


**Figure 5.9:** Comparison between the uncorrected lift coefficients of the mean two-dimensional airfoil profile and the three-dimensional wing. The blue line indicates the $c_l - \alpha$ curve of the mean profile. The red line indicates the mean of the lift coefficients of the 35 profiles; the bars indicate the standard deviation.

# Chapter 6

# Uncertain Wing Geometry

The three-dimensional model of the wing geometry shows deviations from the design airfoil DU96W180. The influence of the uncertain wing geometry is investigated in this chapter. A breakdown of the actions applied to obtain uncertainty information about the geometry is presented in a flow diagram in Figure 6.1.

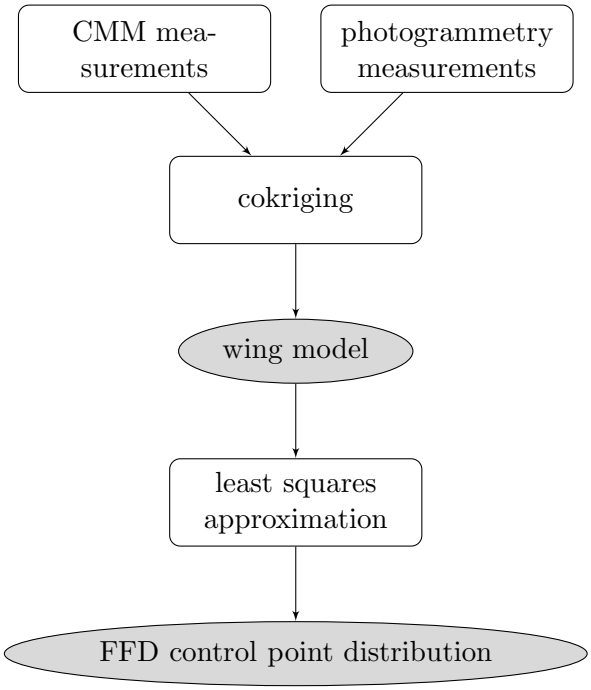


**Figure 6.1:** Flow diagram of the geometry measurements data analysis.

In order to be able to investigate the influence of the wing geometry on the aerodynamic characteristics, it is necessary to parameterize the wing geometry. As discussed in section 6.1, a free-form deformation (FFD) tool is employed to provide a parameterization

with a limited number of parameters. Transformation of the geometric deviations into a probability distribution on the control points, i.e. the FFD parameters, is performed using a least squares approach, as described in section 6.2. Using the probability distribution on the control points, the sensitivity of the lift coefficient with respect to each control point is computed, see section 6.3.

## 6.1 Free-Form Deformation

For uncertainty quantification purposes the amount of variables needs to be reduced considerably. The number of variables of the cokriging model of the wing amounts to $35 \times 201 = 7035$ coordinate points. The amount of variables is greatly reduced by employing a free-from deformation tool, according to Duvigneau [2006] and Sederberg & Parry [1986]. The FFD technique employs a parameterization of the wing and uses thereby considerably less variables.

### 6.1.1 Deformation Principles

The FFD technique allows the deformation of an object in 2D or 3D space, regardless of its geometrical description. In this research the FFD is applied to a two-dimensional profile for simulation and uncertainty analysis purposes. A quadrilateral lattice is built around the object to be deformed. The FFD action can be represented by the movement of control points, which are located on the sides of the lattice. By moving the control points, the object inside the lattice is deformed. A local coordinate system $(\xi, \eta)$ is defined in the lattice with $(\xi, \eta) \in [0,1] \times [0,1]$. The deformation step consists of computing the displacement $\Delta q$ of each point $q$ inside the lattice as defined by the second-order Bézier tensor product

$$\Delta q = \sum_{i=0}^{n_i} \sum_{j=0}^{n_j} B_i^{n_i}(\xi_q)\, B_j^{n_j}(\eta_q)\, \Delta P_{ij}, \tag{6.1}$$

where $B_i^{n_i}$ and $B_j^{n_j}$ are the Bernstein polynomials of order $n_{i,j}$ defined by

$$B_p^n(t) = C_n^p t^p (1-t)^{n-p}.$$

The $(\xi_q, \eta_q)$ coordinates in Equation (6.1) are the FFD coordinates of the point $q$, which result from describing the object in lattice coordinates. The weighting coefficients $\Delta P_{ij}$, i.e. the control points displacements, are the driving variables that induce the deformation. The weighting coefficients can be arranged in a vector as

$$\begin{aligned} \Delta P^T &= [\Delta P_{ij}]_{i=1,\ldots,n_i;j=1,\ldots,n_j} \in \Re^{(n_i+1)\times(n_j+1)} \\ &= \left[\Delta P_{00}, \Delta P_{01}, \ldots, \Delta P_{n_i n_j}\right]. \end{aligned}$$

The Bernstein polynomial terms are arranged in a matrix $B$ where each row $B_q$, corresponding to a coordinate point $q$, is given by

$$\begin{aligned} B_q &= \left[B_i^{n_i}(\xi_q)\, B_j^{n_j}(\eta_q)\right]_{i=1,\ldots,n_i;j=1,\ldots,n_j} \in \Re^{(n_i+1)\times(n_j+1)} \\ &= \left[B_0^{n_i}(\xi_q)\, B_0^{n_j}(\eta_q), B_0^{n_i}(\xi_q)\, B_1^{n_j}(\eta_q), \ldots, B_{n_i}^{n_i}(\xi_q)\, B_{n_j}^{n_j}(\eta_q)\right]. \end{aligned}$$

Now the second-order Bézier tensor product, Equation (6.1), can be expressed as a simple matrix product to replace the double summation as

$$\Delta q = B \Delta P. \tag{6.2}$$

The $B$ matrix only depends on the original geometry of the object and the number of control points. A graphical representation of the two-dimensional FFD applied to the profile is shown in Figure 6.2.

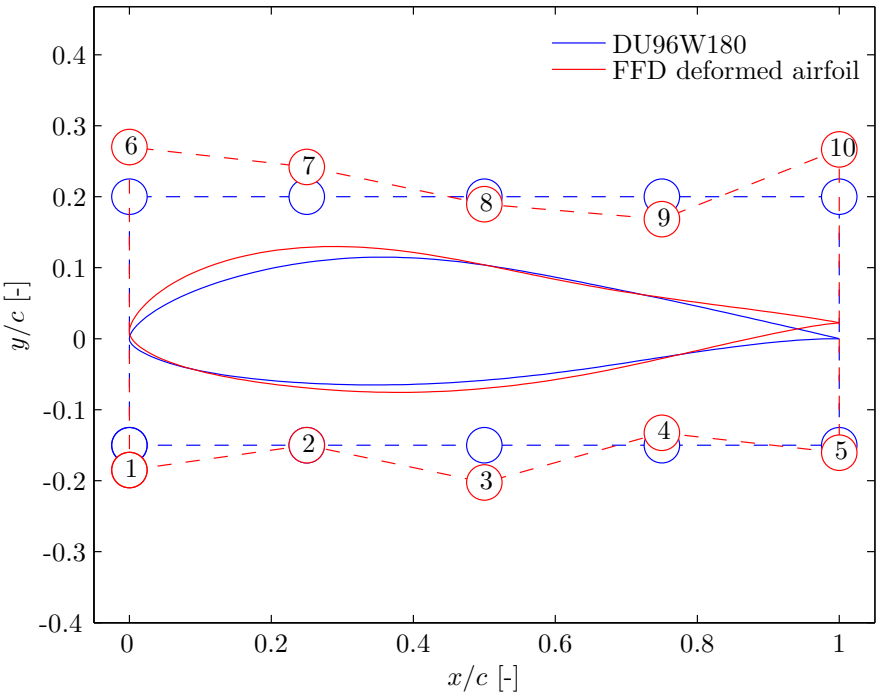


**Figure 6.2:** Free-form deformation of airfoil DU96W180.

### 6.1.2 Determination of the Optimal FFD Control Points

The optimal amount of FFD control points is a compromise between accuracy and computational feasibility. The more control points the FFD has, the better it can represent the measured airfoil. However, the amount of control points is limited since the computation time of the uncertainty analysis using probabilistic collocation increases exponentially with the amount of variables. The ability of the FFD to represent the mean 2D profile, as described in section 5.3, is evaluated using a least squares approximation. The least squares approximation of the weighting coefficients vector $\Delta P|_{lsq}$ on the control points for a given geometry $\Delta q$ is given by

$$\Delta P|_{lsq} = \left(B^T B\right)^{-1} B^T \Delta q.$$

The sum of the least squares residuals is used as an indication of the ability of the FFD to represent a certain geometry. The sum of squared residuals $\Sigma_{res}$ is computed as

$$\Sigma_{res} = \sum \left(\Delta q - B \left(B^T B\right)^{-1} B^T \Delta q\right)^2.$$

$\Sigma_{res}$ is computed for a range of increasing number of control points and shown in Figure 6.3. Initially the residual decreases rapidly but the decrease levels off after 10 control points. Presenting the residual curve on a logarithmic scale in Figure 6.3b shows that the residual goes to zero asymptotically with a decrease of roughly order 1. In the special case that the amount of FFD control points is equal to the amount of coordinates of the profile the least squares approach can be replaced by a matrix inversion and the residual will be zero. Furthermore, taking into account the computation time required for uncertainty analysis, 10 FFD control points are chosen.

The required time to obtain a first order probabilistic collocation approximation of XFOIL simulations for the uncertainty analysis would be

$$T_{PC} = (P+1)^{N_{CP}} \cdot N_d \cdot T_{XFOIL} = (1+1)^{10} \cdot 15 \cdot 1.7 = 7.3\text{h},$$

where $P$ is the PC approximation order and $N_{CP}$ is the number of FFD control points. $N_d$ is the amount of design data points at which the uncertainty is computed, see section 2.2.1, and $T_{XFOIL}$ is the XFOIL evaluation time for $N_{panels} = 350$ according to Table 3.2.

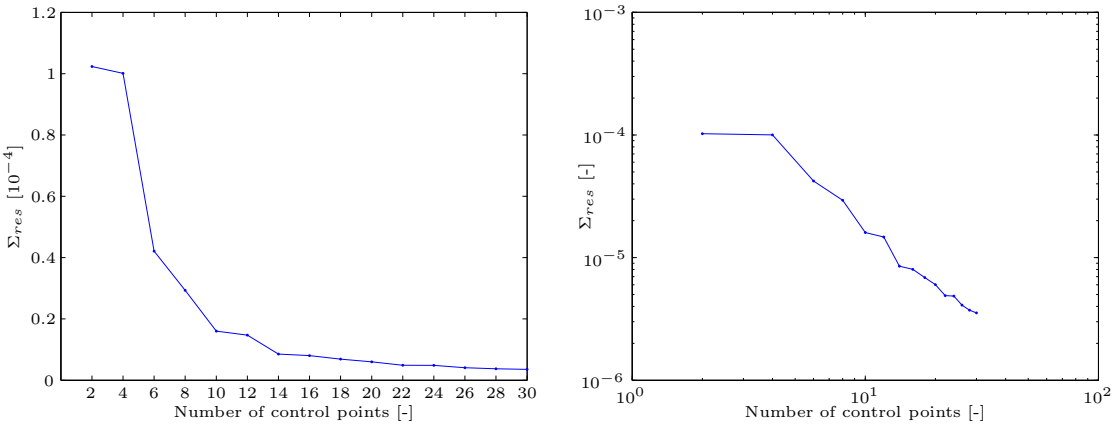


(a) Normal scale.

(b) Logarithmic scale.

**Figure 6.3:** The sum of squared residuals expresses the ability of the FFD tool to represent a given geometry given a certain amount of FFD control points.

## 6.2 FFD Control Weight Distribution

The transformation from a three-dimensional airfoil distribution to a distribution on the FFD control points can be performed in various ways. Although the FFD actually comprises a linear matrix equation it is impossible to use a change of variable approach because the FFD computation, and especially the $B$ matrix in Equation (6.2), is not invertible. Therefore, a least squares approach is applied to solve the overdetermined problem and obtain a distribution of the FFD control weights that represents the uncertain wing geometry.

### 6.2.1 Classification of Profiles

In order to improve understanding of the analysis, clarity in the terminology is enhanced by listing the various profiles that occur in this thesis.

**DU96W180 profile** The wing is manufactured according to the design airfoil of type DU96W180. This design profile is termed DU96W180 profile.

**Kriging profiles** Using cokriging the CMM and Photogrammetry measurements are combined and a three-dimensional wing model is obtained. The three-dimensional wing model is described in 35 two-dimensional profiles along the span of the wing, see section 5.3.1. The 35 two-dimensional profiles obtained with cokriging are called the kriging profiles.

**MC profiles collection** From each of the 35 kriging profiles 2500 airfoil samples are generated by a random generator. The collection of the 2500 samples of all the 35 kriging profiles is called the MC profiles collection.

**Mean 2D profile distribution** The sample mean and covariance are computed for the MC profiles collection of 87500 samples. The resulting profile distribution is termed the mean 2D profile distribution, see section 5.3.2.

**LS profile distribution** Using a least squares approach the FFD control weights are computed corresponding to each sample in the MC profiles collection. This yields 87500 FFD control weights samples. Using the FFD for each FFD control weights sample a corresponding profile can be computed yielding 87500 least squares profiles. Taking the sample mean and covariance of all the 87500 least squares profiles results in the least squares profile distribution, or in short LS profile distribution.

### 6.2.2 Least Squares Approach

The free-form deformation tool consists of two steps. The first step comprises computation of the Bézier polynomials that depend only on the original geometry. The second step, i.e. the deformation step, consists of computing a linear matrix product. During this step the Bézier polynomials do not change. The deformation step can be inverted to find the optimal FFD control weights according to a certain profile by employing a least squares approach. A similar approach is employed here as in the computation of the mean 2D profile distribution, see section 5.3.2, to transform the three-dimensional wing into a two-dimensional distribution.

The least squares approximation of the FFD control weights $\Delta P|_{lsq}$ to a given profile $\Delta q$ is given by

$$\Delta P|_{lsq} = \left(B^T B\right)^{-1} B^T \Delta q, \tag{6.3}$$

where $B$ is the FFD matrix as described in section 6.1. The uncertainty of the wing is propagated to the FFD control points using a Monte Carlo approach. For each of the samples of the MC profiles collection, the least squares approximation of the FFD control weights is obtained using Equation (6.3). A multivariate normal distribution is assumed for the FFD control weights. Taking the sample mean and covariance of all the 87500 FFD

weighting coefficient vectors yields the FFD control weights distribution characteristics. The FFD control weights distribution includes the cokriging uncertainty of each of the kriging profiles as well as the geometrical variation of the wing along the span. The 87500 FFD weighting coefficient vectors are used to compute 87500 corresponding profiles by employing the FFD tool. The sample mean and covariance of these profiles yield the least squares (LS) profile distribution.

### 6.2.3 Least Squares Approximation Results

The least squares approach has provided the sample mean and covariance of the FFD control points representing the geometric uncertainty. Figure 6.4 shows the mean and standard deviations of the control point distribution. The numbering of the control points corresponds to the numbering given in Figure 6.2. The standard deviations are obtained from the covariance matrix by taking the square root of the diagonal elements. The largest standard deviations are found in the middle of the pressure surface ($CP_3$) and at the trailing edge of the suction surface ($CP_{10}$).

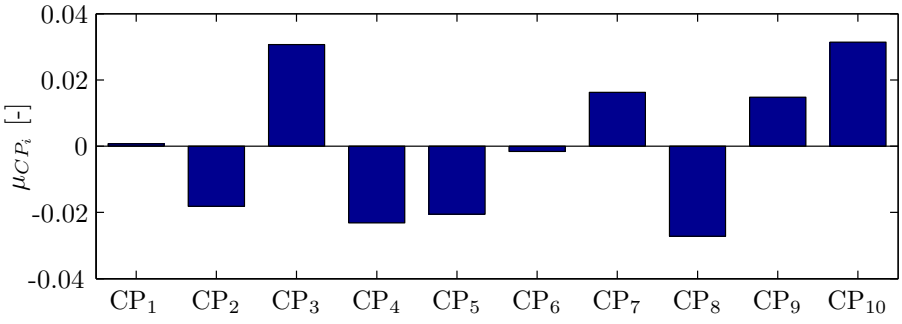


(a) Mean.

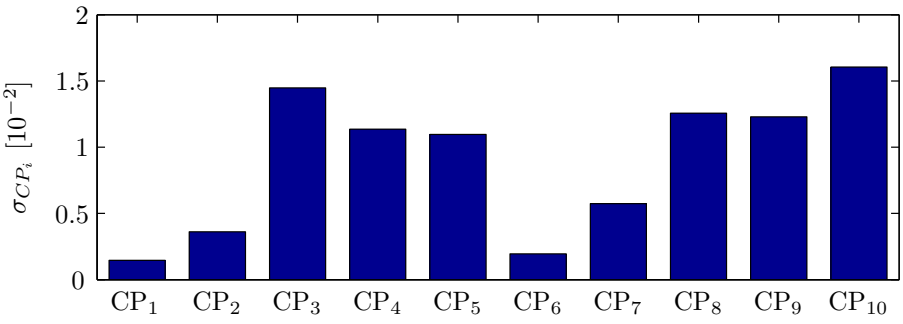


(b) Standard deviation.

**Figure 6.4:** Mean and standard deviations of the FFD control points distribution.

The control points distribution results are investigated by comparing the LS profile distribution with the mean 2D profile distribution. The mean profiles of both distributions are shown in Figure 6.5. Differences between the profiles are hardly visible since the mean 2D profile lies mainly on top of the LS profile. The maximum difference between the profiles in the $y$ direction, i.e. perpendicular to the chordwise direction, amounts to 0.48 mm and occurs at the suction side where the flap is attached to the wing. This difference is mainly

caused by the fact that the FFD cannot represent very sudden variations in the geometry. The mean difference in the $y$ direction between the profiles amounts to 0.06 mm.

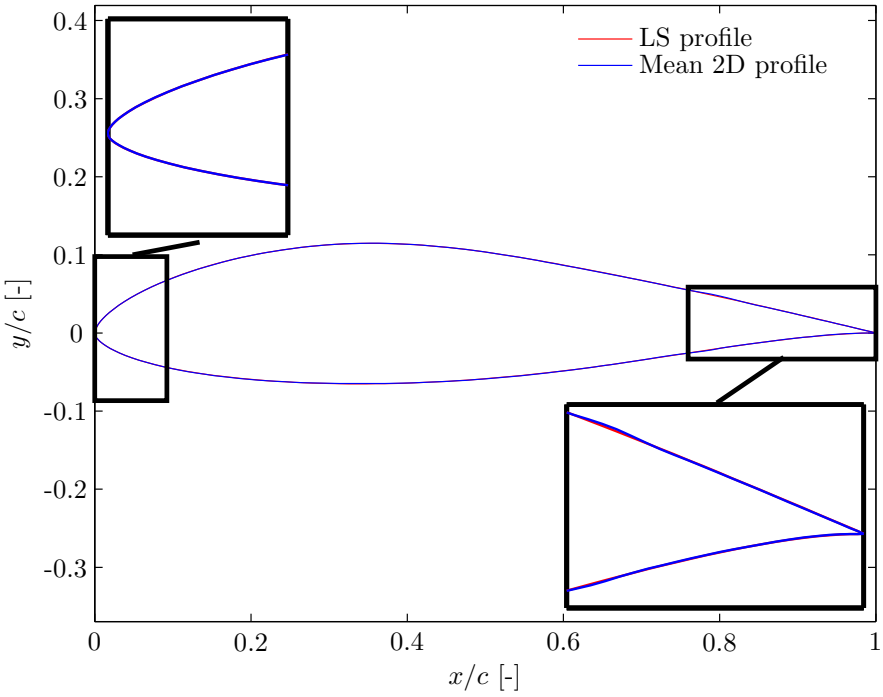


**Figure 6.5:** Airfoil profiles corresponding to the mean of the least squares profiles distribution and the mean 2D profile.

A comparison of the geometric standard deviations of the mean 2D profile distribution and the LS profile distribution is shown in Figure 6.6. Although the standard deviation is overall slightly underestimated, the curve shapes show reasonable resemblance. Also from these graphs it is clear that the FFD cannot represent small variations. The mean and maximum difference between both profiles in the $y$-direction are 0.05 mm and 0.5 mm respectively. Increasing the amount of FFD control points can solve this issue.

It can be concluded that the mean of the control point distribution shows that geometric deviations from the design geometry are small near the leading edge and large in the middle chord region and near the trailing edge. The standard deviations of the control point distribution indicate that geometric variations along the wing span are large in the middle chord region and near the trailing edge.

## 6.3 Sensitivity Analysis

The sensitivity of the lift coefficient to the FFD control points is investigated using a probabilistic collocation based sensitivity analysis, according to section 4.4.4. The XFOIL panel code is employed to perform the required deterministic simulations. The XFOIL input settings are according to Table 3.3. The simulation results are corrected for three-dimensional effects and wind tunnel effects according to section 3.3.

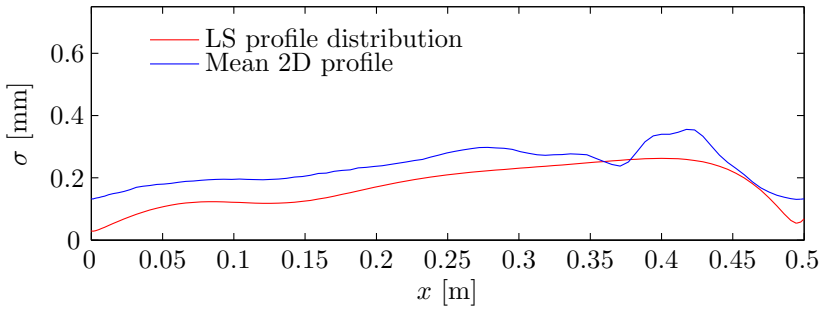


(a) Suction side.

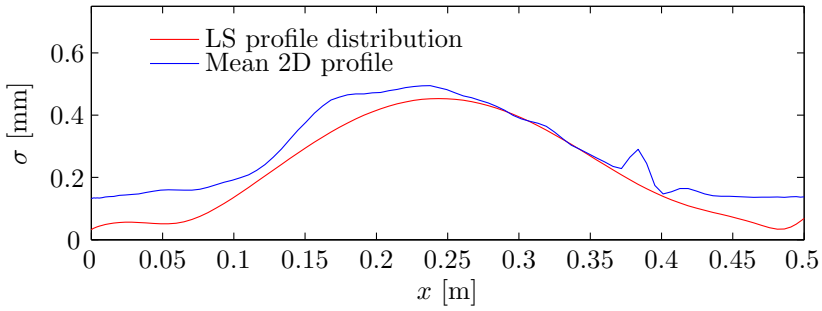


(b) Pressure side.

**Figure 6.6:** Comparison of the standard deviation of the mean 2D profile distribution and the LS profile distribution.

A PC sensitivity analysis is performed using three collocation points for the computation of the derivatives. The sensitivity derivative of the lift coefficient with respect to parameter $a$ is given by $c_{l_a} = \frac{\partial c_l}{\partial a}$. The sensitivity information can be combined with the standard deviation by defining the scaled sensitivity derivative as

$$\hat{c}_{l_a} = \left( \sigma_a \frac{\partial c_l}{\partial a} \right),$$

where $\sigma_a$ is the standard deviation of parameter $a$. The scaled sensitivity provides information about the relative influence of a parameter on the output for parameter comparison purposes.

The sensitivity derivatives of the lift coefficient with respect to the FFD control points are shown in Figure 6.7. The numbering of the control points corresponds to the numbers shown in Figure 6.2. The lift coefficient is most sensitive to geometrical variations near the trailing edge. The scaled sensitivity derivatives are used to determine the relative importance of the FFD coordinates. It is clear that due to the small standard deviation and sensitivity derivatives of the control points at the leading edge the scaled sensitivity derivatives are small. It might be necessary to exclude uncertain variables in the uncertainty analysis due to computational reasons. In that case the first parameters to be discarded are the control points near the leading edge since they are least influential.

The scaled sensitivity derivatives of the moment coefficient indicate as well that the control points in the flap region are most influential, see Figure 6.8. Control points number 2

and 7 are least influential since they are located closest to the aerodynamic center, which is the location at which the moment is applied.

In conclusion it can be said that the largest geometric variations occur in the most influential part of the geometry, i.e. the flap region, according to the sensitivity derivatives.

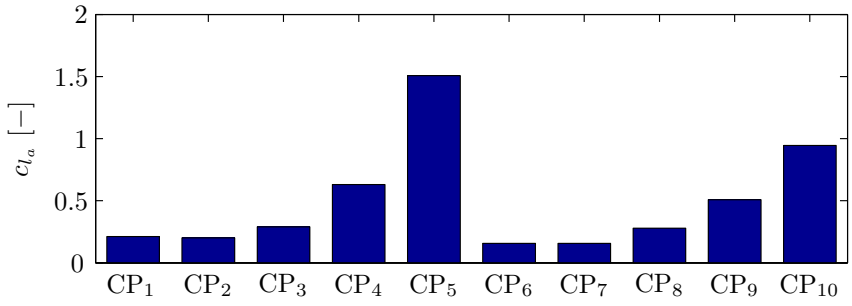


(a) Unscaled sensitivity derivatives.

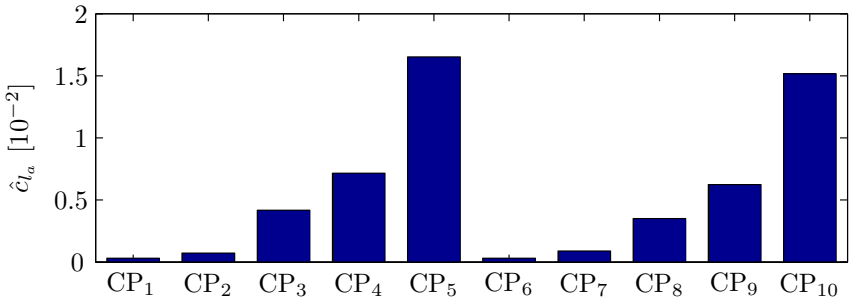


(b) Scaled sensitivity derivatives.

**Figure 6.7:** Sensitivity derivatives of the lift coefficient with respect to the FFD control points.

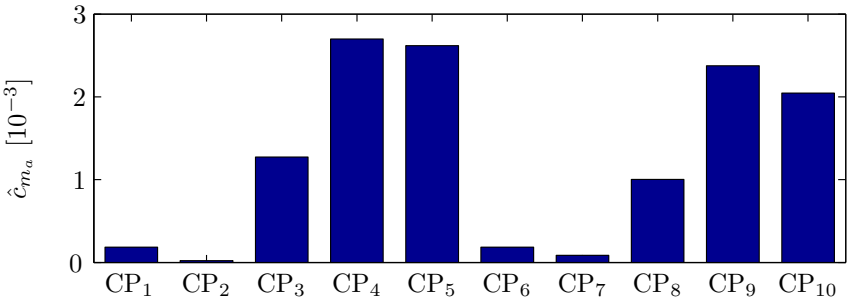


**Figure 6.8:** Scaled sensitivity derivatives of the moment coefficient with respect to the FFD control points.

# Chapter 7

# Uncertain Experimental Parameters

The uncertain wing geometry includes only part of the uncertain inputs. Various other input uncertainties are present in the experiment for which uncertainty distributions need to be defined. A distinction is already made between geometric uncertainties and experimental input uncertainties. The experimental input uncertainties will be investigated in this chapter to obtain uncertainty distributions of all major input parameters for the uncertainty analysis.

The experimental input uncertainties are classified and quantified in section 7.1, yielding uncertainty distributions for the inputs. Given the distributions of the uncertain input parameters, a sensitivity analysis is performed, see section 7.2.

## 7.1 Determination of Input Uncertainties

Many variables are present in the experiment as performed according to chapter 2. One can distinguish between variables related to the tunnel conditions, which are termed tunnel variables, and variables related to the specific measurement setup, which are termed experimental setup variables. Tunnel variables are for example the free stream velocity, the pressure or the density. Examples of the experimental setup variables are the angle of attack, the flap angle, the wing position in the open jet stream and the width of the gap between the wing and the side walls.

Based on experience and employing qualitative reasoning a choice is made of the most important variables. Since there is a quadratic relationship between the aerodynamic forces and the velocity, the free stream velocity $V$ is chosen as the most important tunnel variable. In many aerodynamic experiments the aerodynamic characteristics are determined as a function of angle of attack and flap angle since these variables are very influential. Therefore, from the experimental setup parameters the angle of attack $\alpha$ and flap angle $\delta$ are chosen for the uncertainty analysis. The presence of a gap between the wing and the side walls introduces wing tip vortices. Since the wing tip vortices are regarded as the

most important three-dimensional effects the gap width $\Delta g$ is included for the uncertainty analysis as well.

The results of sensitivity and uncertainty analyses are of course highly dependent on the input uncertainties. Therefore the input uncertainties need to be determined carefully. Preferably the uncertainties are computed based on available data. In case of lack of data an educated guess is made.

Independent normal distributions are assumed for the input variables angle of attack $\alpha$, flap angle $\delta$, free stream velocity $V$ and gap width $\Delta g$. In case various uncertainties are related to one input variable the errors can be combined. Let $X$ and $Y$ be two independent random variables that are normally distributed as

$$\begin{aligned} X &\sim N\left(\mu_X, \sigma_X^2\right), \\ Y &\sim N\left(\mu_Y, \sigma_Y^2\right). \end{aligned}$$

In that case the sum of both variables is distributed as

$$X + Y \sim N\left(\mu_X + \mu_Y, \sigma_X^2 + \sigma_Y^2\right).$$

In case only the maximum error is known a conservative approach is employed in that the maximum error is regarded as the standard deviation of a normal distribution.

### 7.1.1 Angle of Attack

For the determination of the uncertainty in angle of attack, only geometric effects are taken into account. The uncertainty in the angle of attack with respect to the streamlines (i.e. the effective angle of attack) is accounted for by wind tunnel corrections. These corrections take into account the deflection of streamlines due to the open jet exit. The geometric uncertainty can be broken down into two contributions, one caused by platform instability and the other caused by mold inaccuracy. It is assumed that there is a constant systematic error present, which is invariant of the angle of attack. This systematic error introduces a discrepancy in the angles of attack. The angle of attack discrepancy is denoted by the random variable $\Delta\alpha$.

The contribution that is related to platform instability is determined during the experiment. The platform or measurement table on which the structure and the wing are positioned moves slightly when forces are applied. The uncertainty in the inclination of the platform is determined by measuring the inclination angle before, during and after an experimental run. Readings are collected during multiple experimental runs and the uncertainty is determined as 0.07 degrees. The angle measurements are performed using a Clinotronic PLUS measurement device with a measurement error of less than 0.03 degrees. Using a conservative approach these maximum errors are treated as standard deviations of normal distributions. The total uncertainty in angle of attack caused by platform instability amounts to $\sqrt{0.07^2 + 0.03^2} = 0.076$ degrees.

The uncertainty related to mold inaccuracy is difficult to determine. The wooden mold is manufactured based on CMM measurements of the wing profile. The mold fits the wing nicely in the middle chord region, i.e. $0.1c < x < 0.8c$, where $c$ is the chord length and $x$ is the chordwise coordinate. However, near the leading edge and in the flap

region the mold does not fit the wing profile very well. Based on these considerations an uncertainty of 0.25 degrees is estimated. During the experiment the wing angle of attack is set by measuring the angle of the mold using the Clinotronic PLUS measurement device described above. The sum of the mold inaccuracy and the measurement error amounts to a total uncertainty of $\sqrt{0.25^2 + 0.03^2} = 0.252$ degrees related to the mold.

Adding up the two contributions of uncertainty yields a total uncertainty in the angle of attack of

$$\sigma_\alpha = \sqrt{0.076^2 + 0.252^2} = 0.263^\circ.$$

### 7.1.2 Flap Deflection Angle

The flap deflection angle is defined as the angle between the airfoil chord and the flap chord. Three uncertainty contributions can be distinguished in the flap angle uncertainty. Statistical as well as systematic errors contribute to the total flap angle uncertainty. Since the systematic error is assumed to be invariant of the flap angle it introduces a constant discrepancy in the angle of attack. The flap angle discrepancy is denoted by the random variable $\Delta\delta$.

The most important uncertainty contribution originates from the fact that the mold is rather inaccurate in the flap region. Using the photogrammetry measurements, as described in section 5.2, the flap angle offset for the airfoil clamped in the mold is determined. Using numerical optimization the total sum of the distance between the coordinates of the 2D design profile and the photogrammetry measurements in 2D is minimized by varying the position of the measured wing. Performing this optimization for the region of the wing in front of the flap yields that the chord lines of the design profile and the measured profile lie approximately on top of each other. Including now a deflecting flap in the design profile, the optimum flap angle is computed again by using numerical minimization of the sum of distances between measurements and design profile in the flap region. The resulting flap deflection angle is found to be 0.58 degrees.

The flap is kept in position by two servo engines that are attached to the wing and move the flap via levers. The flap deflection angle is controlled by applying a voltage to the servo engines. The amount of voltage required for a desired angle is determined via a calibration. The calibration is performed by measuring the flap angle by the Clinotronic PLUS angle measurement device and the voltage on the servo engines. The uncertainty related to the calibration originates therefore mainly from the measurement error and amounts to 0.03 degrees.

The third contribution of uncertainty in flap deflection angle is caused by the actuation system. There is no uncertainty present that stems from the influence of the flap weight and lift force on the servo engines, since the servo engines are strong enough to counteract these forces. However, the mechanical free play in the actuation system, which is mainly caused by the connection of the lever to the engines and the flap, introduces flap angle uncertainty. The free play introduces uncertainty because of the changing forces on the flap. This uncertainty contribution is determined by comparing the set input flap angle with the flap angle that is measured during experimental runs. It amounts to an uncertainty of 0.07 degrees. This time the flap angle is measured using a built-in device that is calibrated simultaneously with the calibration of the servo engines. The error of the

measurement device is less than two digits and shows therefore not up in the uncertainty angle of this contribution.

The total uncertainty in the flap angle is caused by mold inaccuracy, calibration error and mechanical free play. The sum of these contributions amounts to a total flap deflection angle uncertainty of

$$\sigma_\delta = \sqrt{0.58^2 + 0.03^2 + 0.07^2} = 0.585°.$$

This is the value for the parametric variability of the flap deflection angle used as an input for uncertainty analysis.

### 7.1.3 Free Stream Velocity

During the experiment the free stream velocity in the test section is controlled by the RPM of the fan that accelerates the air in the wind tunnel. Small fluctuations in the velocity are measured by a pitot tube located at the tunnel exit. The inaccuracy of the pitot tube in $m/s$ amounts to less than two digits. Measurements of the wind speed are recorded for each experimental run. Analyzing the recorded wind speed measurements shows that the wind speed has a standard deviation of 0.05 m/s, see Table 2.1.

### 7.1.4 Gap Width

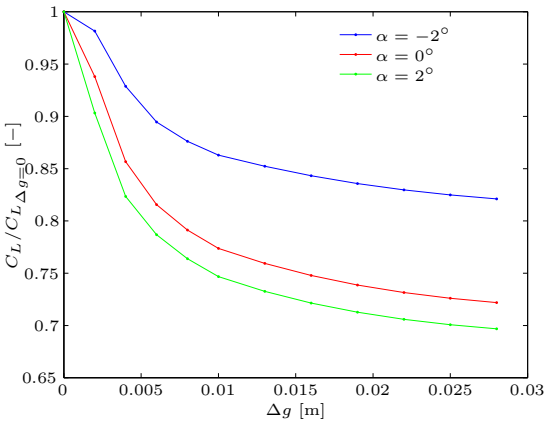


**Figure 7.1:** Influence of the gap size $\Delta g$ on the lift coefficient, normalized with the $C_L$ at zero gap size for various angle of attack.

The wing is suspended to a structure between two side walls that diminish 3D flow effects. In between the wing and the side walls a small gap of approximately 4 mm is present. Although the fact that the structure and the connection of the wing to the structure is rigid, the exact gap width is not exactly measured during the experiment. Furthermore, based on the irregularity of the wing sides the gap size uncertainty is estimated at 1 mm.

The presence of a gap introduces three-dimensional effects in the flow. Vortices are formed around the wing tips. The reduction in lift coefficient for increasing gap size is presented in Figure 7.1 for various angles of attack. The curves are based on Tornado computations for varying gap width and angle of attack. For increasing gap width the lift coefficient decreases due to the formation of wing tip vortices. The most severe decrease in lift coefficient occurs for increasing the gap width from 0 to 10 mm. For large gap widths the lift coefficient will approach a constant value since the gap width is large enough for the full development of the wing tip vortices. Furthermore, for increasing angle of attack the influence of the gap size on the lift coefficient increases.

The probability distributions of the uncertain input variables are fully determined by the mean and standard deviation. A summary of the characteristics of the normal distributions of the uncertain experimental input parameters is given in Table 7.1. These uncertainty distributions are the inputs for the uncertainty analysis to obtain output uncertainty distributions.

| | Contributions | Total | Mean |
|---|---|---|---|
| Angle of attack $\Delta\alpha$ | | 0.263° | 0° |
| Mold | 0.252° | | |
| Platform | 0.076° | | |
| Flap angle $\Delta\delta$ | | 0.585° | 0° |
| Mold | 0.58° | | |
| Calibration | 0.03° | | |
| Mechanical free play | 0.07° | | |
| Wind speed $V$ | | 0.05 m/s | 21 m/s |
| Gap width $\Delta g$ | | 1 mm | 4 mm |

**Table 7.1:** Breakdown of the estimated standard deviations of the uncertain experimental inputs.

## 7.2 Sensitivity Analysis

Using the probabilistic collocation method the uncertainty distributions on the angle of attack, flap angle, wind speed and gap size are propagated. A deterministic code is used to obtain solutions at the collocation points of the PC approximation.

### 7.2.1 Deterministic Code

The numerical code employed to obtain the aerodynamic characteristics is the Tornado vortex lattice method code, see section 3.2. The choice for this code is based on time limitations and on the fact that three-dimensional effects need to be included for the gap width. From Table 3.4 the finest grid, i.e. grid number 5, is chosen for the sensitivity analysis because a very fine grid is required to perform accurate computations for very small variations in gap width.

In order to be able to compare with the experimental results, a normalization is employed that is slightly different from the regularly used normalization. The lift, drag and moment coefficients are obtained from normalizing the aerodynamic quantities with a fixed wind speed of 21 m/s. The lift coefficient is computed as

$$\begin{aligned} C_L &= \frac{L}{\frac{1}{2}\rho V^2 S}, \\ &= \frac{L}{\frac{1}{2}\cdot 1.225 \cdot 21^2 \cdot (1.8 \cdot 0.5)}, \end{aligned}$$

where $\rho$ is the density, $V$ is the wind speed and $S$ is the wing area. The wind tunnel corrections and chord length correction are applied to the coefficients according to sec-

tion 3.3. This approach is similar to the way the aerodynamic coefficients are computed during the experiment.

### 7.2.2 Sensitivity Derivatives

A sensitivity analysis is performed according to the method described in section 4.4.4, using three collocation points to compute the derivative. The unscaled sensitivity derivative $C_{L_a} = \frac{\partial C_L}{\partial a}$ as well as the scaled sensitivity derivative $\hat{C}_{L_a} = \left(\sigma_a \frac{\partial C_L}{\partial a}\right)$ is computed. The computation is based on the uncertainty distributions of the input variables, meaning that the derivative is computed at the location of the mean of the distributions. The results are presented in Table 7.2.

| | $\sigma_a$ | $C_{L_a}$ | $C_{M_a}$ | $\hat{C}_{L_a}$ [-] | $\hat{C}_{M_a}$ [-] |
|---|---|---|---|---|---|
| $\Delta\alpha$ | 0.263° | 0.094 /° | -0.534·$10^{-3}$ /° | 0.0246 | 0.14·$10^{-3}$ |
| $\Delta\delta$ | 0.585° | 0.051 /° | -11.2·$10^{-3}$ /° | 0.0297 | 6.58·$10^{-3}$ |
| $V$ | 0.05 m/s | 0.026 /(m/s) | -6.95·$10^{-3}$ /(m/s) | 0.0013 | 0.35·$10^{-3}$ |
| $\Delta g$ | 0.001 m | -3.603 /m | 0.465 /m | 0.0036 | 0.47·$10^{-3}$ |

**Table 7.2:** Sensitivity analysis results for the experimental parameters showing the standard deviation $\sigma_a$ of the input parameters, the unscaled sensitivity derivative $C_{L,M_a}$ and the scaled sensitivity derivative $\hat{C}_{L,M_a}$.

Investigation of the unscaled derivatives shows that the lift coefficient is roughly twice as sensitive to variations in the angle of attack than to variations in the flap angle. The sensitivity to variations in gap width is very large due to the fact that the decrease in lift coefficient is large for a gap width ranging from 0 to 10 mm, see Figure 7.1. The sensitivity of the lift coefficient to velocity variations is smallest from the four sensitivity derivatives. The sensitivity results for the moment coefficient show different behavior. The unscaled derivatives show that also the moment coefficient is very sensitive to the gap width. Furthermore, the moment coefficient is sensitive to flap angle variations but very insensitive to variations in angle of attack and free stream velocity.

Using Figure 7.2 a comparison of the scaled sensitivity derivatives is performed. The lift coefficient sensitivity derivatives show that out of the four uncertain experimental input parameters, the angle of attack and the flap angle are clearly the most influential parameters. The influence of the angle of attack is almost similar to the influence of the flap angle. The effect of the wind speed is almost negligible with respect to the influence of $\Delta\alpha$ and $\Delta\delta$. The sensitivity of the lift coefficient with respect to the gap size is also small with respect to the angle of attack and flap angle, although its influence is larger than the influence of the velocity. Note that the mean gap width is very influential for the sensitivity derivative of the gap width, as can be seen from Figure 7.1. The scaled sensitivity derivatives of the moment coefficient show the same behavior, except for the angle of attack discrepancy, see Figure 7.2b. It is clear that the moment coefficient is extremely insensitive to variations in angle of attack.

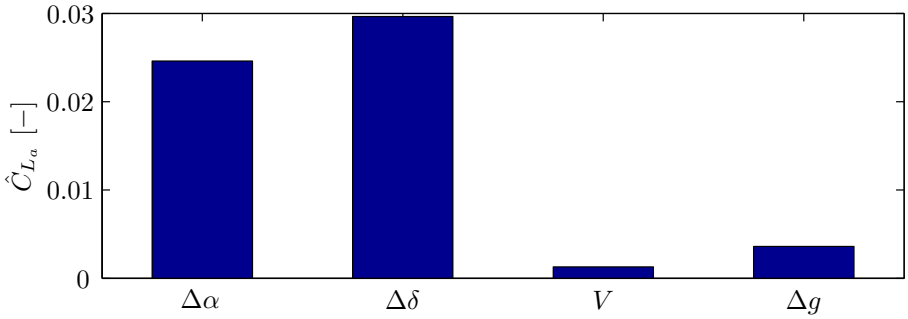


(a) Lift coefficient.

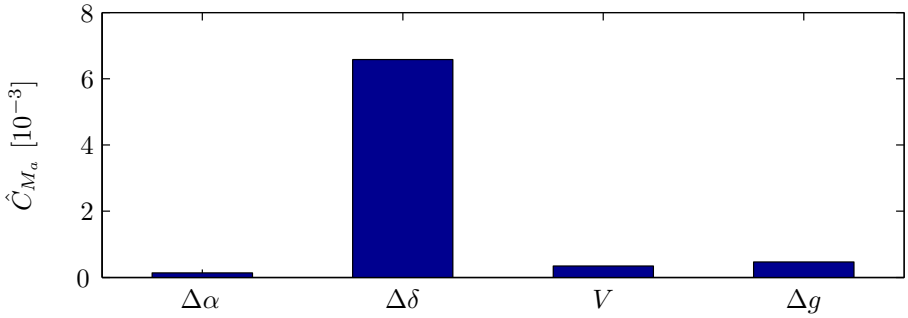


(b) Moment coefficient.

**Figure 7.2:** Sensitivity of the lift and moment coefficient to angle of attack discrepancy $\Delta\alpha$, flap angle discrepancy $\Delta\delta$, wind speed $V$ and gap size $\Delta g$.

# Chapter 8

# Uncertainty Analysis

Having obtained the uncertainty distributions of the input parameters, the output uncertainties can be estimated using uncertainty analysis. Uncertainty analysis deals with propagating input distributions through a model to obtain uncertainty distributions on the outputs. The output uncertainties provide observation fidelity information for the validation of computer codes.

In order to reduce the amount of variables included in the uncertainty analysis, the sensitivity derivatives of the geometric and experimental input parameters are compared and the most influential parameters are selected, see section 8.1. In the uncertainty analysis XFOIL and Tornado computations are combined to obtain the aerodynamic outputs. The rather complicated integration of both codes and the uncertainty analysis approach are described in section 8.2. The resulting output uncertainties are presented and discussed in section 8.3.

## 8.1 Determination of Important Parameters

The results of the sensitivity analyses of the geometric parameters and experimental parameters, which are presented in sections 6.3 and 7.2 respectively, indicate that some uncertain input parameters have a relatively small influence on the lift coefficient compared to other parameters. The most important parameters can easily be determined by comparing the scaled sensitivity derivatives of all uncertain parameters. The scaled sensitivity derivatives of all parameters are shown together in Figure 8.1. The least important parameters are determined as the velocity $V$ from the experimental parameters and the FFD coordinates $CP_1$, $CP_2$, $CP_6$ and $CP_7$ from the geometric parameters. The remaining uncertain parameters that will be used for the uncertainty analysis are the angle of attack discrepancy $\Delta\alpha$, the flap angle discrepancy $\Delta\delta$, gap width $\Delta g$ and the FFD control points $CP_3$, $CP_4$, $CP_5$, $CP_8$, $CP_9$, and $CP_{10}$.

The moment coefficient sensitivity derivatives show roughly the same behavior for the experimental inputs as well as the geometric inputs except for the angle of attack, see

sections 6.3 and 7.2.2. However, since the influence of the angle of attack on the lift coefficient is clear the angle of attack is regarded as an important variable.

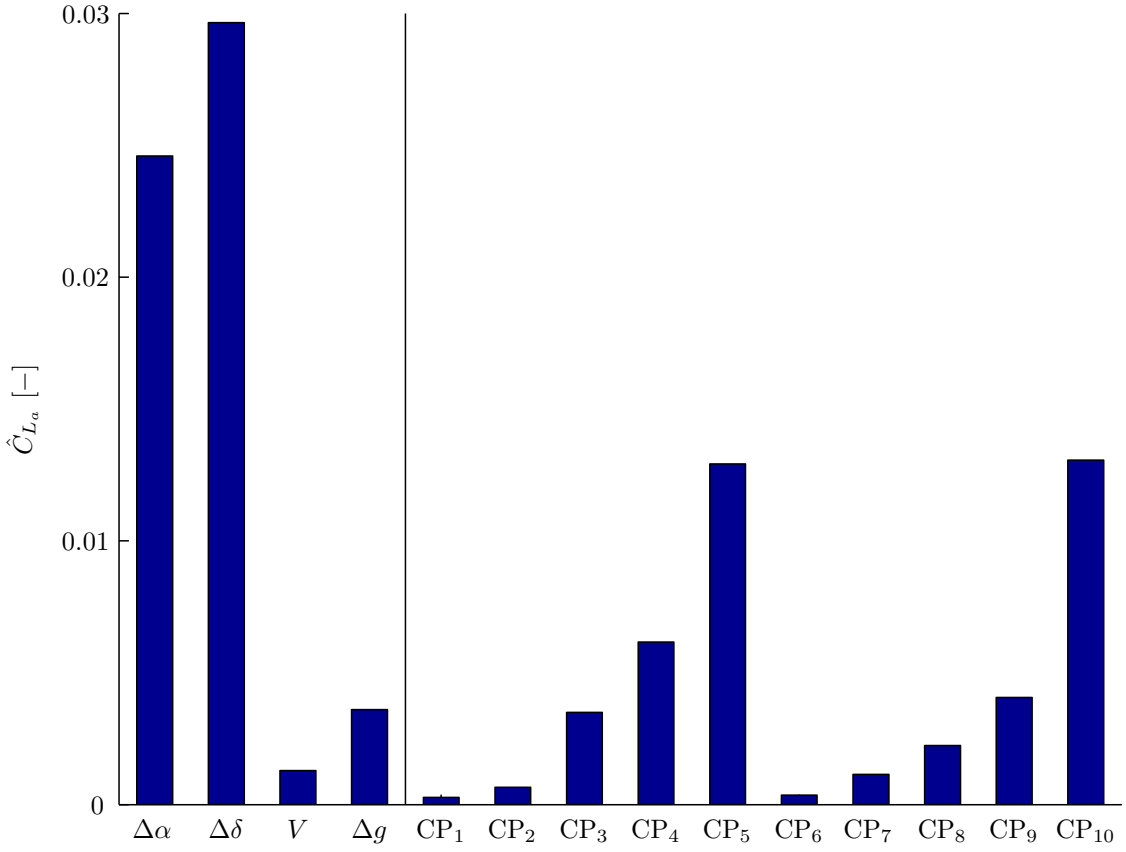


**Figure 8.1:** Scaled sensitivity derivatives of the uncertain experimental parameters and the uncertain geometric control points.

For the determination of the uncertainty in the flap angle the geometric uncertainty of the wing is included, see section 7.1.2. This uncertainty however is also included in the FFD coordinates. Therefore, to avoid including the geometric flap uncertainty twice, the contribution due to the uncertain geometry in the flap angle uncertainty is left out. According to Table 7.1 the flap angle uncertainty becomes $\sigma_\delta = 0.076°$. The uncertainty values of the other parameters are as determined in sections 6.2 and 7.1.

## 8.2 Uncertainty Analysis Approach

Input uncertainties are propagated to compute the lift and moment coefficient uncertainty. The difficulty with the set of important parameters is that both XFOIL and Tornado need to be used in order to investigate the influence of all the important variables. The geometric variables, i.e. the control points, need a very accurate representation of the geometry in the simulation program, which is provided by XFOIL. The gap width however cannot be included in XFOIL computations but needs three-dimensional Tornado computations.

Therefore the analysis is performed in multiple steps in order to be able to include all important uncertain parameters. First a Probabilistic Collocation surface is made using XFOIL computations. Secondly a kriging surface is obtained using Tornado calculations. Monte Carlo integration is performed on these surfaces to compute the lift coefficient uncertainty.

### 8.2.1 Probabilistic Collocation of XFOIL Computations

Probabilistic collocation is performed on the variables $\alpha$, $\delta$ and the selected control points $\mathrm{CP}_{3,4,5,8,9,10}$ according to section 4.4. The control points are dependent variables and have a multivariate normal distribution. In order to be able to calculate collocation points the distribution needs to be marginalized to obtain independent distributions for each control point. A PC surface of the lift and moment coefficient can be made using the independent distributions of $\alpha$, $\delta$ and the control points $\mathrm{CP}_{3,4,5,8,9,10}$.

The PC approximation order is determined by investigating the approximation error. In order to reduce computational efforts, only the input variables $\alpha$, $\delta$ and $\mathrm{CP}_{3,9,10}$ are used for the computation of the approximation error. This is based on the assumption that the control points that are not taken into account have the same effect on the approximation error as the control points that are taken into account. The approximation error of the PC order $p$ approximation is computed using the deterministic values of an order 4 PC approximation as a reference, according to Equation (4.20). The approximation error for order $P = 1, 2, 3$ approximations is shown in Figure 8.2. The approximation errors for an order 3 approximation are similar to an order 2 approximation. This could indicate that the coefficients are quadratic functions of the input variables. Increasing the polynomial order would not yield improved approximation results in that case. The error of the approximation order 1 is sufficiently small for the uncertainty analysis. Multiplication of the error with its normalization factor yields an average difference between approximation and deterministic runs of $2.8 \cdot 10^{-4}$ for $C_L$ and $0.5 \cdot 10^{-4}$ for $C_M$. This error is acceptable for the uncertainty analysis since the uncertainty in the coefficient is estimated to be of order higher than $10^{-2}$.

A PC approximation is obtained for each of the 15 experimental data points, see section 2.2.1. The total number of deterministic evaluations of XFOIL amounts to

$$\begin{aligned} N_{solves} &= (P+1)^{N_{vars}} \cdot N_d \\ &= (1+1)^8 \cdot 15 = 3840, \end{aligned}$$

where $P$ is the PC approximation order, $N_{vars}$ is the number of variables and $N_d$ is the amount of experimental design data points. The PC surface provides an approximation of $C_L$ as a function of $\alpha$, $\delta$ and $\mathrm{CP}_{3,4,5,8,9,10}$

$$C_L^{X,PC}\left(\alpha, \delta, \mathrm{CP}_{3,4,5,8,9,10}\right),$$

where $C_L^{X,PC}$ is the lift coefficient computed by XFOIL and approximated using probabilistic collocation.

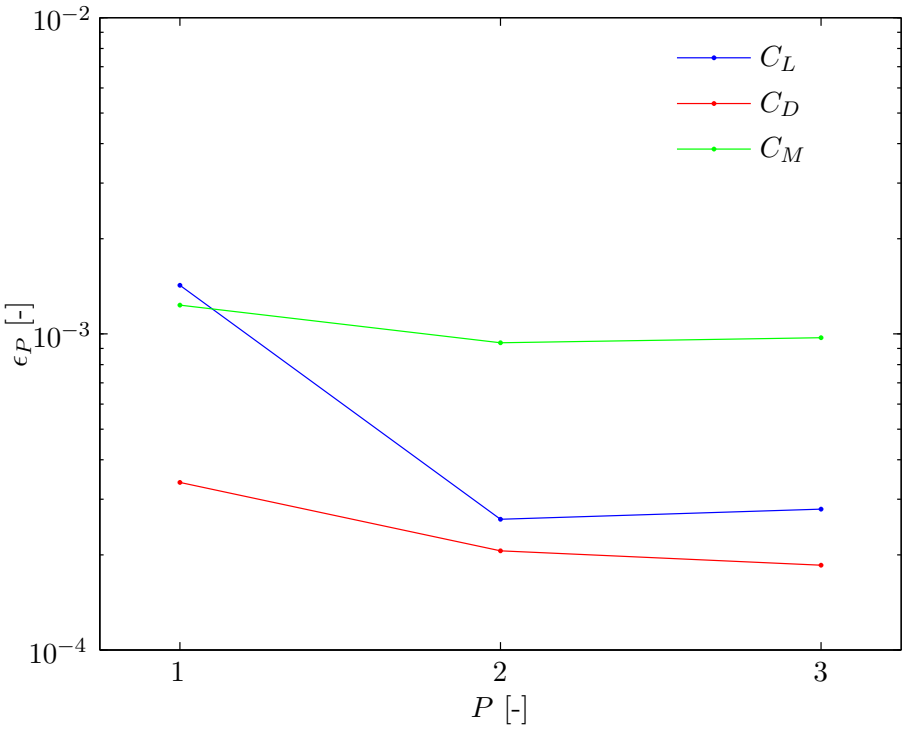


**Figure 8.2:** Error of the PC approximation for various orders $P$ with respect to a fourth order PC approximation.

### 8.2.2 Kriging on Tornado Computations

It is impossible to model the influence of the gap width on $C_L$ using XFOIL. Therefore, Tornado is used to obtain $C_L$ as a function of the gap width $\Delta g$. The assumption is made that the gap width is not directly correlated with $\alpha$, $\delta$ and $\mathrm{CP}_{3,4,5,8,9,10}$ but only indirectly via the lift coefficient. This assumption is made based on the fact that the flow field is mainly characterized by the lift coefficient.

The PC surface of XFOIL computations and the kriging surface of Tornado computations are integrated into one mathematical process to obtain the lift coefficient. A relation is required between the XFOIL computations and the Tornado computations in order to combine both computational results.

The Tornado computations are performed using a different angle of attack than used for the XFOIL computations. The Tornado equivalent angle of attack $\alpha^T$ is obtained from

$$C_L^T\left(\alpha^T, \Delta g_0\right) = C_L^{X,PC}\left(\alpha, \delta, \mathrm{CP}_{3,4,5,8,9,10}\right), \tag{8.1}$$

where $C_L^T$ is the Tornado computed lift coefficient and $\Delta g_0 = 0$ mm is the zero gap width. This transformation is based on the simplifying assumption that the zero gap width lift coefficient corresponds to the two-dimensional XFOIL results. Three-dimensional effects such as the presence of the side walls and the slits in the side walls are neglected for simplicity. This procedure is similar to the approach employed for the gap correction in section 3.3.1. The final lift coefficient including variations in the gap width can now be

obtained from

$$C_L^T\left(\alpha^T, \Delta g\right),$$

where $\Delta g$ is a variable gap width.

It is practically impossible to perform a Tornado computation for each $C_L^{X,PC}$ during the Monte Carlo simulation. Therefore a kriging surface is obtained according to section 4.3, using a limited amount of Tornado computations to model the gap width influence.

The transformation from $\alpha$, $\delta$ and $\mathrm{CP}_{3,4,5,8,9,10}$ to equivalent $\alpha^T$, Equation (8.1), is complicated to perform. Therefore a much simpler approach is applied to obtain a kriging surface of the gap width influence on $C_L$.

Deterministic runs of the Tornado code are required for the kriging surface. Initially a range of $\alpha^T$ inputs are chosen to obtain a broad range in the lift coefficient. This input range is evaluated for a range of gap sizes $\Delta g$. A lift coefficient discrepancy factor is obtained as

$$\delta C_L^T\left(\alpha^T, \Delta g\right) = C_L^T\left(\alpha^T, \Delta g\right) - C_L^T\left(\alpha^T, \Delta g_0\right),$$

where again $\Delta g_0 = 0$ is the zero gap width. Suppressing the input argument $\alpha^T$ this equation can be written as

$$\delta C_L^T\left(C_L^T\left(\Delta g_0\right), \Delta g\right) = C_L^T\left(\Delta g\right) - C_L^T\left(\Delta g_0\right),$$

where $C_L^T\left(\Delta g_0\right)$ is the zero gap width lift coefficient. The inputs for $\delta C_L^T$ are now not the transformed angle of attack $\alpha^T$, but only the zero gap width lift coefficient and the gap width. In this procedure the transformation from XFOIL angle of attack $\alpha$ to equivalent Tornado angle of attack $\alpha^T$ is performed implicitly.

The kriging surface for the discrepancy $\delta C_L^T$ as a function of zero gap width lift coefficient $C_L^T\left(\Delta g_0\right)$ and gap width $\Delta g$ is shown in Figure 8.3. The kriging prediction error is in the order of $5 \cdot 10^{-5}$ for both the lift coefficient and the moment coefficient.

### 8.2.3 Integration of PC and Kriging Surrogates

The PC surface outputs and the kriging prediction outputs are combined to compute the final simulation lift coefficient. Since the zero gap width lift coefficient $C_{L_{\Delta g=0}}^T$ agrees reasonably well with the two-dimensional XFOIL lift coefficient, the latter can now be used as an input for the lift coefficient discrepancy term. The final lift coefficient $C_L^F$ is computed as

$$\begin{aligned} C_L^F\left(\alpha, \delta, \mathrm{CP}_{3,4,5,8,9,10}, \Delta g\right) &= C_L^{X,PC}\left(\alpha, \delta, \mathrm{CP}_{3,4,5,8,9,10}\right) \\ &\quad + \delta C_L^T\left(C_L^{X,PC}\left(\alpha, \delta, \mathrm{CP}_{3,4,5,8,9,10}\right), \Delta g\right). \end{aligned}$$

This approach enables to compare the results of both programs. First, the two-dimensional lift coefficient as a function of $\alpha$, $\delta$ and $\mathrm{CP}_{3,4,5,8,9,10}$ is computed using the PC surface of XFOIL data. Second, the two-dimensional lift coefficient is used as an input for the kriging surface of Tornado data together with the gap width. The resulting lift coefficient is a function of all input variables and is essentially a three-dimensional computation. Wind tunnel corrections as well as the chord length correction are applied to this data in order to compare well with the experimental conditions. A schematic representation of the computation procedure is shown in Figure 8.4.

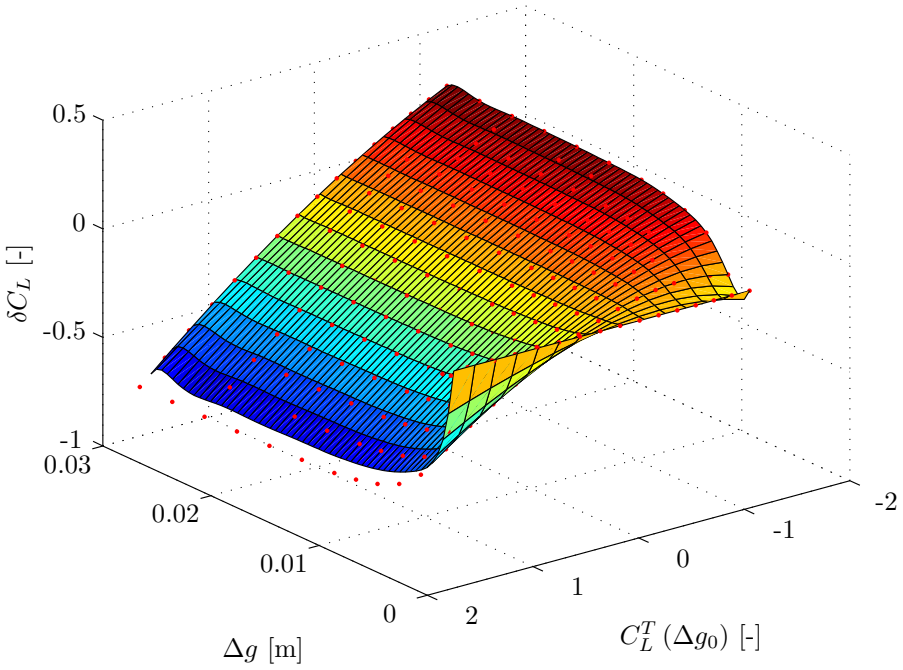


**Figure 8.3:** Kriging surface of the lift coefficient discrepancy $\delta C_L^T$ as a function of zero gap width lift coefficient $C_L^T(\Delta g_0)$ and gap width $\Delta g$.

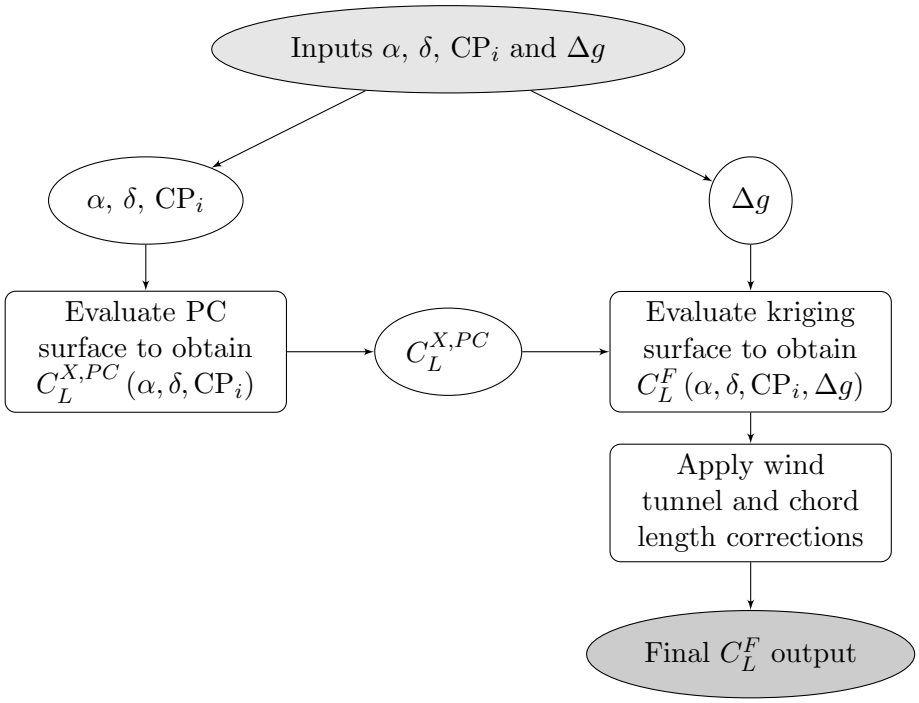


**Figure 8.4:** Flow diagram of the computation of the lift coefficient by combining XFOIL and Tornado computations via a PC surface and a kriging surrogate.

### 8.2.4 Monte Carlo Integration

Uncertainty results are obtained from Monte Carlo integration on the PC and kriging surfaces. From the input normal distributions of $\alpha$, $\delta$, $\Delta g$ and the multivariate normal distribution of the FFD coordinates $CP_{3,4,5,8,9,10}$, a large number of Monte Carlo samples is generated. An $N_{MC}$ amount of Monte Carlo $10^4$ samples yields a converged result.

The $N_{MC}$ samples of the input distributions are propagated using the PC surface and kriging surface as explained in Figure 8.4. The sample mean and standard deviation are obtained from all the samples of the lift coefficient $C_L^F$. During the experiment steady measurements are performed at 15 different angle of attack and flap angle input points, see chapter 2. For each of the 15 experimental input points the Monte Carlo procedure is performed separately. The same analysis is performed for the moment coefficient $C_M$.

## 8.3 Uncertainty Results

The input uncertainties, which are described in chapters 6 and 7, are propagated through PC and kriging surfaces of XFOIL and Tornado data to obtain uncertainties in the aerodynamic quantities. The uncertainty analysis is only performed for the lift and moment coefficients.

### 8.3.1 Uncertain Lift Coefficient

Figure 8.5 shows the results of the uncertainty analysis together with the experimental data for the lift coefficient. The shaded areas correspond to uncertainty intervals of 2 standard deviations, which correspond to approximately 95% of all possible outcomes. The standard deviation of the measurements is computed by adding two contributions, assuming normal distributions for the uncertain quantities. One contribution originates from the noise between the data samples that are recorded for 1 data point. The other contribution is caused by measurement equipment inaccuracies, which are reported in section 2.1.3.

The $C_L - \alpha$ and $C_L - \delta$ curves in Figure 8.5 show roughly a linear discrepancy between the simulation results and the observations. For $\alpha$ larger than -2 degrees even uncertainty intervals of 2 standard deviations do not show overlap. Between the $C_L - \delta$ curves no overlap is present for $\delta$ larger than 2 degrees.

The average standard deviation for the lift coefficient simulation results amounts to 0.025, which is equivalent to an uncertainty of 0.30 degrees in angle of attack. It means that the combined effect of all the input uncertainties taken into account in the uncertainty analysis are equivalent to an input uncertainty of 0.30 degrees in the angle of attack. This value is relatively low since it is only slightly larger than only the input standard deviation of the uncertain angle of attack, which is 0.263 degrees.

### 8.3.2 Uncertain Moment Coefficient

The uncertain moment coefficient data of the measurements and the simulations are shown in Figure 8.6. Again the shaded areas indicate uncertainty intervals corresponding to 2

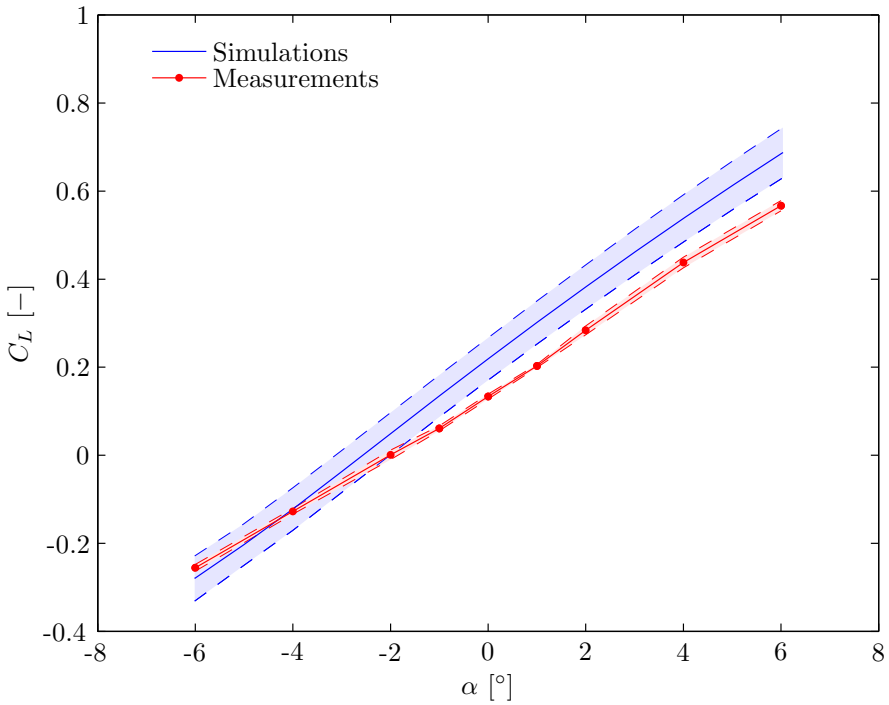


(a) $C_L - \alpha$ curves.

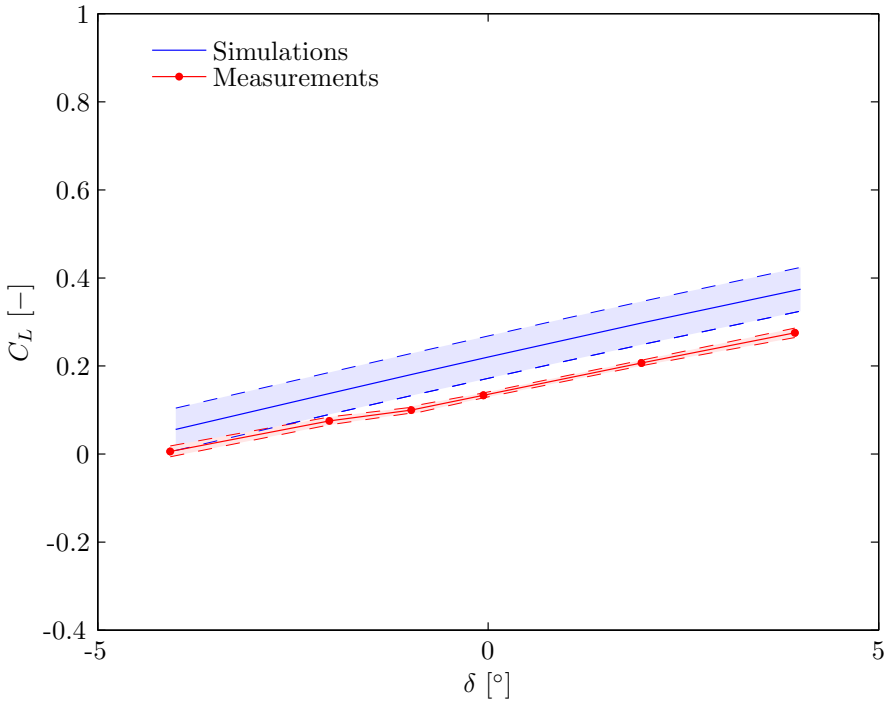


(b) $C_L - \delta$ curves.

**Figure 8.5:** The uncertain lift coefficient is compared with experimental lift coefficient data. The shaded areas between the dashed lines correspond to an uncertainty interval of 2 standard deviations.

standard deviations. The standard deviation of the measurements is computed similar to the uncertainty of the observed lift coefficient data.

The average standard deviation for the moment coefficient amounts to $2.3 \cdot 10^{-3} C_M$, which is equivalent to a flap angle standard deviation of 0.28 degrees. This value is considerably higher than the input flap angle uncertainty of 0.076 degrees because it corresponds to the uncertainties of the experimental as well as the geometric input parameters. However, it is only half the flap angle uncertainty estimated in section 7.1, which is 0.585 degrees. In this section the flap angle uncertainty due to the geometry was estimated to be 0.58 degrees. The uncertainty analysis has revealed that the total $C_M$ uncertainty corresponds to a flap angle uncertainty smaller than 0.58 degrees. Therefore the initial estimate was too conservative.

The $C_M - \alpha$ as well as the $C_M - \delta$ curve show clearly discrepancies between the simulation results and the observational data. Similar to the lift coefficient data the simulation results for $\alpha$ smaller than -2 degrees correspond better to the observations than for $\alpha$ larger than -2 degrees. The discrepancy between simulation results and observation is approximately linear in $\alpha$ and also linear in $\delta$.

### 8.3.3 Discrepancies between Simulations and Observations

The discrepancy between observations and simulations can either be caused by model inadequacy or by improper input uncertainty estimates. Because of the fact that the discrepancy is large it is highly likely that it is caused by model inadequacy.

Within the model employed to obtain the simulation lift coefficients inadequacy can be introduced by XFOIL, by Tornado or by the gap correction. A source of the inadequacy in XFOIL that can be deducted from analysis in this thesis is related to the boundary layer computations. The determination of the tripping location in section 3.1.2 shows that the lift and moment coefficients are sensitive to the location of tripping.

Model inadequacy furthermore is likely to be introduced in the gap correction. The gap correction is obtained from inviscid computations and applied to viscous computations. This fundamental difference inevitably causes errors. Furthermore, the estimate of the mean gap width of 4 mm can deviate from the true input value and consequently cause considerable discrepancies. The gap width influence is obtained from Tornado computations with a large range of angle of attack. This limits the accuracy as well since VLM computations are based on the assumption of small angles. And finally, simulation codes will never represent reality exactly but there will be always discrepancies present.

The errors introduced by the PC approximation are unimportant since they are approximately a factor of $1/100^{\text{th}}$ smaller than the lift and moment coefficient uncertainties. The kriging prediction error is even smaller than the PC approximation error and will therefore also have negligible influence. Since the finest grids are used for the XFOIL and Tornado computations the small discretization errors apply to the uncertainty results.

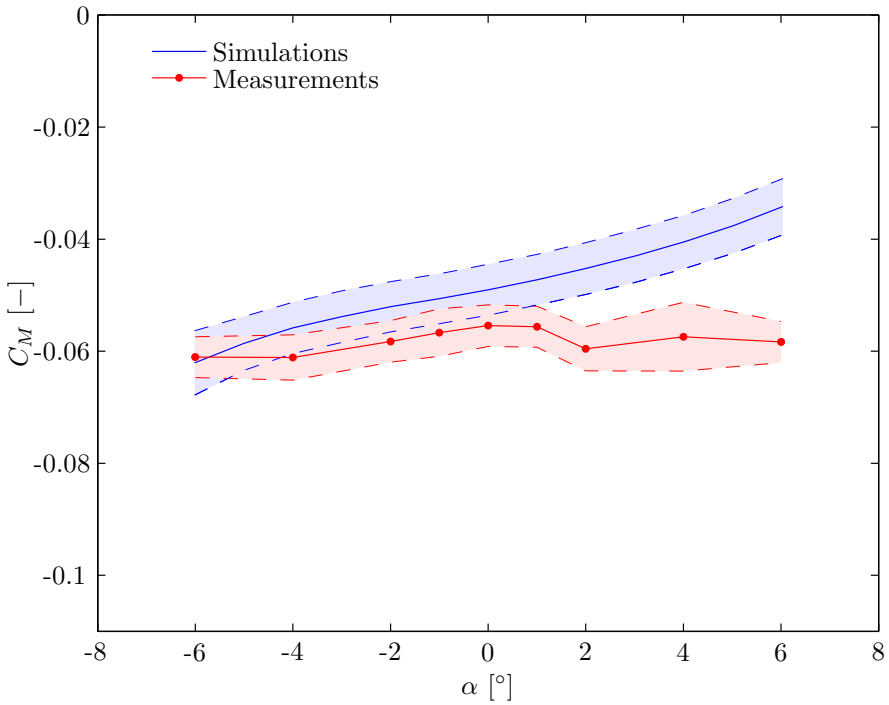


(a) $C_M - \alpha$ curves.

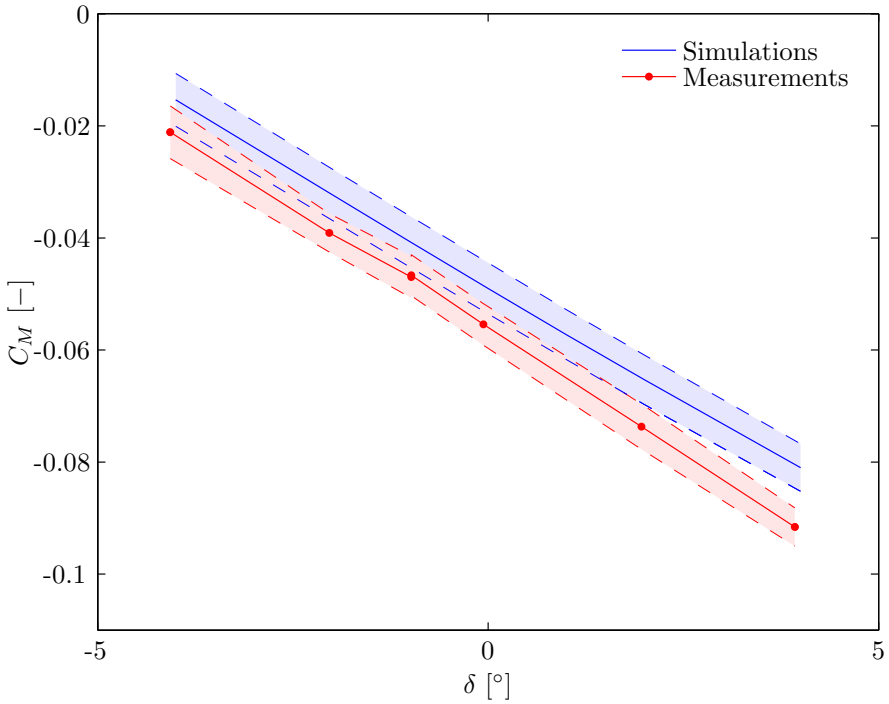


(b) $C_M - \delta$ curves.

**Figure 8.6:** Comparison of the uncertain moment coefficient with experimental moment coefficient data. The shaded areas between the dashed lines correspond to an uncertainty interval of 2 standard deviations.

## 8.4 Implications of the Uncertainty Results

It must be concluded that the computed output uncertainties do not represent the total error between simulations and observations since only little overlap is present between the uncertainty intervals of the simulations and observations. This can be caused by underestimation of the input parametric uncertainties, by having missed certain input parameters or by the exclusion of model inadequacy errors from the uncertainty analysis. The latter reason is most probable since really systematic discrepancies are present between the curves and the simulated $C_M - \alpha$ curve shows a very different behavior than the observations curve.

Although the fact that the output uncertainties do not represent the total error, the uncertainty estimates are still suitable for validation purposes. A reasonable assumption is that the model inadequacy causes mainly a constant discrepancy in the results and has minor influence on output variations and thus on the uncertainty estimates. This assumption justifies to add the simulation output uncertainty to the measurement error distributions to obtain a proper estimate of the uncertainty of the experimental results. The experimental results uncertainty estimates include measurement uncertainties as well as input uncertainties and are a valuable input for the validation of computer codes with respect to the uncertain observations.

Inferences about the uncertainties in the fluid-structure interaction experiment can be made using the output uncertainties on the lift and moment coefficient around zero angle of attack and zero flap angle. The applicability of these results is limited by the fact that the flow is changed for this case from steady to unsteady. Furthermore, additional uncertain inputs are present in the experiment, such as the flap deflection amplitude and the period of the oscillation cycles. These facts introduce additional uncertainties in the experiment yielding probably larger output uncertainties than estimated for the steady case.

# Chapter 9

# Calibrated Prediction

The uncertainty characteristics of the experimental outputs have been obtained from uncertainty analysis. By combining the experimental observations with the simulation model inferences can be made about the uncertain input variables. Reducing input uncertainties by using observations is known as the inverse problem. The inverse problem is investigated using a Bayesian calibration technique.

The calibration framework is based on the use of Gaussian processes, as explained in section 9.1. The specific approach required to solve the calibration problem is outlined in section 9.2. The results of the calibration are presented and discussed in section 9.3.

The steady experiment has provided relatively accurate lift and moment coefficient data. The drag however has been measured with strain gauges that are subject to large measurement errors. Therefore, predictions of the drag coefficient are made using computer codes with the calibration estimates as inputs, as discussed in section 9.4.

## 9.1 Calibration Framework

Prior to the prediction of the drag coefficient, the computer code inputs are calibrated using observational data for $C_L$ and $C_M$. The calibration framework employed in this chapter is based on work of Kennedy & O'Hagan [2001a] and Kennedy & O'Hagan [2001b].

### 9.1.1 Statistical Model

Calibration refers to estimating unknown or uncertain code input parameters such that the observational data $z_i$ fit the code outputs as closely as possible. The relationship between the observations $z_i$, the true process $\zeta$ and the computer model output $\eta$ is represented by

$$z_i = \zeta(\boldsymbol{x}_i) + e_i = \eta(\boldsymbol{x}_i, \boldsymbol{\theta}) + \kappa(\boldsymbol{x}_i) + \epsilon_i, \tag{9.1}$$

where $e_i$ is the observation error for the $i^{\text{th}}$ observation. The observation error is assumed to be normally distributed with zero mean and standard deviation $\lambda$, i.e. $e_i \sim N(0, \lambda)$. Discrepancies between real process and computer model are accounted for by the discrepancy term $\kappa$. Furthermore, the simulations residual variation is denoted by $\epsilon_i$. A distinction is made between the variable inputs $\boldsymbol{x}_i$ and the calibration parameters $\boldsymbol{\theta}$, i.e. the input parameters to be calibrated. The true calibration parameters $\boldsymbol{\theta}$ provide the best fit of the simulation data to the observations according to the error structure of the statistical model.

Models are never perfect and represent reality never exactly. Therefore usually the discrepancy term $\kappa$ is included in the statistical model. The discrepancy term is modeled as a function of the variable inputs $\boldsymbol{x}_i$ using Gaussian processes. It is estimated based on the observational data. In certain cases it may be difficult or impossible to model the discrepancy term, e.g. due to the fact that little observational data at uncorrelated inputs is available. In that case the discrepancy term is simply left out, implying that the calibrated inputs will be subject to errors due to model inadequacy.

Because of the fact that computer model output $\eta$ is relatively expensive to acquire, a surrogate is obtained using kriging, as described in section 4.3.

The uncertain or unknown calibration parameters can either be physical quantities that are present in both the experiment and the computer code or code input parameters that are not present in the experiment. In case the computer model represents reality very accurately the calibrated parameters can be said to correspond to the true experimental input parameters for physical input parameters. Input parameters that only occur in the computer code are model specific parameters. Those inputs exist for example as constants in turbulence modeling methods.

### 9.1.2 Posterior Distribution

The mathematical framework for calibration is very similar to the cokriging framework described in section 4.3.2. In fact the simulation outputs are equivalent to the low fidelity dataset and the observations to the high fidelity dataset. The main difference with cokriging is that the important output for calibration is he likelihood function instead of cokriging predictions.

#### Data Distribution

The calibration inputs are estimated using a Markov chain Monte Carlo approach on the posterior distribution of the calibration parameters, according to section 4.5. The posterior distribution is derived in a Bayesian way using the data likelihood function. The full data vector $\boldsymbol{d}$ is modeled as a Gaussian process conditional on the calibration parameters $\boldsymbol{\theta}$ and the hyperparameters $\phi$.

The set of points at which the code outputs $\boldsymbol{y}$ are computed is denoted by the input data vector $D_1 = \{(\boldsymbol{x}_1^*, \boldsymbol{t}_1), \ldots, (\boldsymbol{x}_N^*, \boldsymbol{t}_N)\}$, where $N$ refers to the number of simulation outputs. The set of inputs for the observations $\boldsymbol{z}$ is denoted by $D_2 = \{\boldsymbol{x}_1, \ldots, \boldsymbol{x}_n\}$, where $n$ refers to the number of observations. The set of observation inputs can be augmented with the

calibration parameters $\boldsymbol{\theta}$ yielding the augmented dataset $D_2(\boldsymbol{\theta}) = \{(\boldsymbol{x}_1, \boldsymbol{\theta}), \ldots, (\boldsymbol{x}_n, \boldsymbol{\theta})\}$. The expectation of the full data vector $\boldsymbol{d}$ is given by

$$E(\boldsymbol{d}|\boldsymbol{\theta}, \boldsymbol{\beta}, \boldsymbol{\phi}) = \boldsymbol{m}_d(\boldsymbol{\theta}) = \boldsymbol{H}(\boldsymbol{\theta})\boldsymbol{\beta}, \tag{9.2}$$

where

$$\boldsymbol{H}(\boldsymbol{\theta}) = \begin{pmatrix} \boldsymbol{H}_1(D_1) & \boldsymbol{0} \\ \boldsymbol{H}_1(D_2(\boldsymbol{\theta})) & \boldsymbol{H}_2(D_2) \end{pmatrix}. \tag{9.3}$$

In these equations the rows of the $\boldsymbol{H}_i$ matrices are formed by $\boldsymbol{h}_i(\boldsymbol{x}_1^*, \boldsymbol{t}_1), \ldots, \boldsymbol{h}_i(\boldsymbol{x}_N^*, \boldsymbol{t}_N)$, where $\boldsymbol{h}_i$ is a vector of regression functions.

The variance matrix $\boldsymbol{V_d}$ of the distribution of the full data vector $\boldsymbol{d}$ is defined by

$$\begin{aligned} \operatorname{var}(\boldsymbol{d}|\boldsymbol{\theta}, \boldsymbol{\beta}, \boldsymbol{\phi}) &= \boldsymbol{V_d}(\boldsymbol{\theta}) \\ &= \begin{pmatrix} \sigma_1^2 A_1(D_1, D_1) + \epsilon I_N & \sigma_1^2 A_1(D_1, D_2(\boldsymbol{\theta})) \\ \sigma_1^2 A_1(D_2(\boldsymbol{\theta}), D_1) & \sigma_1^2 A_1(D_2(\boldsymbol{\theta}), D_2(\boldsymbol{\theta})) + \sigma_2^2 A_2(D_2, D_2) + \lambda I_n \end{pmatrix}, \end{aligned} \tag{9.4}$$

where $\boldsymbol{I}_n$ is the $n \times n$ identity matrix. The element $i, j$ of the matrix of correlations $A_t(D_k, D_l)$ between data sets $D_k$ and $D_l$ is given by

$$A_t\left(x_i^{(k)}, x_j^{(l)}\right) = \exp\left\{-\sum_m \frac{1}{2b_{tm}^2}\left(x_{im}^{(k)} - x_{jm}^{(l)}\right)^2\right\}$$

for all $x_i^{(k)} \in D_k$ and $x_j^{(l)} \in D_l$, where $b_{tm}$ are the correlation parameters and $t = 1, 2$.

In case the model discrepancy term $\kappa$ is left out from the statistical model, Equation (9.1), the $\boldsymbol{H}$ matrix and the variance matrix $\boldsymbol{V_d}$ change to

$$\boldsymbol{H}(\boldsymbol{\theta}) = \begin{pmatrix} \boldsymbol{H}_1(D_1) \\ \boldsymbol{H}_1(D_2(\boldsymbol{\theta})) \end{pmatrix}, \tag{9.5}$$

$$\boldsymbol{V_d}(\boldsymbol{\theta}) = \begin{pmatrix} \sigma_1^2 A_1(D_1, D_1) + \epsilon I_N & \sigma_1^2 A_1(D_1, D_2(\boldsymbol{\theta})) \\ \sigma_1^2 A_1(D_2(\boldsymbol{\theta}), D_1) & \sigma_1^2 A_1(D_2(\boldsymbol{\theta}), D_2(\boldsymbol{\theta})) + \lambda I_n \end{pmatrix}. \tag{9.6}$$

Because no discrepancy term is included the calibration tries to find the best fit of the simulation outputs to the observations without discrepancy, taking into account only the residual variation $\epsilon_i$ and the observation error $e_i$.

### Joint Posterior Distribution

The full joint posterior distribution is obtained from the likelihood function and the prior distributions as

$$p(\boldsymbol{\theta}, \boldsymbol{\beta}, \boldsymbol{\phi}|\boldsymbol{d}) \propto L\{\boldsymbol{d}; \boldsymbol{m_d}(\boldsymbol{\theta}), \boldsymbol{V_d}(\boldsymbol{\theta})\} p(\boldsymbol{\theta}) p(\boldsymbol{\beta}) p(\boldsymbol{\phi}), \tag{9.7}$$

where the likelihood function $L\{\boldsymbol{d}; \boldsymbol{m_d}(\boldsymbol{\theta}), \boldsymbol{V_d}(\boldsymbol{\theta})\}$ is the $N\{\boldsymbol{m_d}(\boldsymbol{\theta}), \boldsymbol{V_d}(\boldsymbol{\theta})\}$ density function and $p(\boldsymbol{\theta})$ is the prior distribution for the calibration parameters. Furthermore $p(\boldsymbol{\beta})$ and $p(\boldsymbol{\phi})$ are priors for the hyperparameters $\boldsymbol{\beta}$ and $\boldsymbol{\phi}$. Markov chain Monte Carlo integration is applied to Equation (9.7) to obtain calibration parameter estimates.

#### Estimation of Regression Parameters and Hyperparameters

The regression parameters $\boldsymbol{\beta}$ can be obtained from completing the square in the exponent of the likelihood function as

$$\begin{aligned} \hat{\beta}(\boldsymbol{\theta}) &= \boldsymbol{W}(\boldsymbol{\theta})\,\boldsymbol{H}(\boldsymbol{\theta})\,\boldsymbol{V_d}(\boldsymbol{\theta})^{-1}\,\boldsymbol{d}, \\ \boldsymbol{W}(\boldsymbol{\theta}) &= \left(\boldsymbol{H}(\boldsymbol{\theta})^T\,\boldsymbol{V}(\boldsymbol{\theta})_{\boldsymbol{d}}^{-1}\,\boldsymbol{H}(\boldsymbol{\theta})\right)^{-1}. \end{aligned} \tag{9.8}$$

Integrating out $\boldsymbol{\beta}$ yields an extra term $\boldsymbol{W}(\boldsymbol{\theta})$ in the data likelihood function, which is given by

$$L(\boldsymbol{d}|\boldsymbol{\theta}) \propto |\boldsymbol{V_d}(\boldsymbol{\theta})|^{-1/2}\,|\boldsymbol{W}(\boldsymbol{\theta})|^{1/2} \exp\left\{\left(\boldsymbol{d}-\boldsymbol{H}(\boldsymbol{\theta})\,\hat{\boldsymbol{\beta}}\right)^T \boldsymbol{V_d}(\boldsymbol{\theta})^{-1}\left(\boldsymbol{d}-\boldsymbol{H}(\boldsymbol{\theta})\,\hat{\boldsymbol{\beta}}\right)\right\}.$$

In order to reduce the amount of parameters to be estimated, the hyperparameters $\boldsymbol{\phi}$ for the observations are estimated prior to the McMC simulation. The procedure to estimate the hyperparameters is similar to the procedure employed for the estimation of cokriging hyperparameters, see section 4.3.2.

Since the regression parameters $\boldsymbol{\beta}$ and the hyperparameters $\boldsymbol{\phi}$ are excluded from the McMC simulation, their prior distributions $p(\boldsymbol{\beta})$ and $p(\boldsymbol{\phi})$ are left out from the joint posterior distribution, Equation (9.7).

## 9.2 Calibration Approach

The calibration approach can be broken down into various aspects. Initially a clear definition of the variable inputs and calibration parameters is necessary, as discussed in section 9.2.1. Section 9.2.2 describes the process of acquiring simulation data. A discussion of the statistical model and the posterior distribution is given in sections 9.2.3 and 9.2.5 respectively.

### 9.2.1 Calibration Inputs

In the calibration process a clear distinction needs to be made between the variable inputs $\boldsymbol{x}$ and the calibration parameters $\boldsymbol{\theta}$. The full set of inputs that are used for the uncertainty analysis in chapter 8 are taken as the set of available inputs for calibration. In section 8.1 it is concluded that the most important parameters are the angle of attack $\alpha$, the flap angle $\delta$, the gap width $\Delta g$ and a number of the FFD control points $\mathrm{CP}_i$. In order to reduce the amount of calibration parameters, the assumption is made that the geometric variation as modeled by the FFD control points can be approximated by variations in $\alpha$ and $\delta$. The variables that remain are the angle of attack, flap angle and the gap width. The downward flap deflection direction is defined as positive.

During the experiment, for each measurement point the angle of attack and flap angle are set according to the procedure specified in section 2.1.3. Because the procedure and measurement equipment are similar for all measurement points it is assumed that the

uncertainty in the angle of attack and the flap angle is mainly caused by a constant offset $\Delta\alpha$ and $\Delta\delta$. Since the gap width is not measured during the experiment it is treated as an unknown calibration input. The calibration input vector consists of $\boldsymbol{\theta} = \{\Delta\alpha, \Delta\delta, g\}$.

The variable inputs are formed by the values of the angle of attack and flap angle that are set during the experiment. The experimental design input values for the angle of attack and flap angle are denoted by $\alpha_0$ and $\delta_0$ respectively. The variable input vector therefore is given by $\boldsymbol{x} = \{\alpha, \delta\}$. Note that the calibration inputs and the variable inputs are related to each other via

$$\begin{aligned} \alpha &= \alpha_0 + \Delta\alpha, \\ \delta &= \delta_0 + \Delta\delta. \end{aligned}$$

As explained later this relationship will cause problems for the discrepancy term in the statistical model.

### 9.2.2 Generation of Simulation Data

Simulation data are generated in a similar way as is done during the uncertainty analysis, see section 8.2. XFOIL computations are performed for a range of angle of attack and flap angle. Using the kriging model of the lift and moment coefficient discrepancy terms, see section 8.2.2, the influence of the gap width is included for $\Delta g = 0 \ldots 30$ mm. The wind tunnel and chord length corrections are applied to the resulting aerodynamic coefficients and the angle of attack, according to section 3.3. In order to be able to model the lift coefficient as a function of the variable inputs and calibration parameters the following relation is applied

$$C_L^S\left(\alpha_0, \delta_0, \Delta\alpha, \Delta\delta, \Delta g\right) = C_L^F\left(\alpha_0 + \Delta\alpha, \delta_0 + \Delta\delta, \Delta g\right),$$

where $C_L^F$ is computed as explained in section 8.2 and $C_L^S$ is the simulation lift coefficient used for calibration. The same is applied to obtain the moment coefficient simulation data. Finally kriging is applied to the lift coefficient and moment coefficient data as a function of $\alpha_0$, $\delta_0$, $\Delta\alpha$, $\Delta\delta$ and $\Delta g$.

The input airfoil for the XFOIL computations is the DU96W180 airfoil. This airfoil is selected based on the assumption that geometric variations can be translated into variations in angle of attack and flap angle. The calibration will provide calibrated inputs where the geometric uncertainty is taken into account as an equivalent angle of attack and flap angle.

### 9.2.3 Discrepancy Modeling

The comparison of the experimental observations and the simulation data in section 8.3 has shown that, even taking into account input parametric uncertainties, there are clearly discrepancies present between the observational data and the simulations. The discrepancy between simulations and observations shows roughly a linear behavior in angle of attack for the lift coefficient data as well as the moment coefficient data. The discrepancy

term can be modeled as a function of the variable inputs using regression functions that are linear in $\alpha_0$ and independent of $\delta_0$.

This approach of modeling the discrepancy will yield bad results since variations in the variable inputs $\alpha_0$ and $\delta_0$ are interchangeable with variations in the calibration parameters $\Delta\alpha$ and $\Delta\delta$. Modeling the discrepancy as a function of $\alpha_0$ makes it impossible to calibrate for systematic uncertainties in $\Delta\alpha$. Furthermore, the calibration will not yield the best fit of the simulation data to the observational data for the lift coefficient and moment coefficient as a function of angle of attack and flap angle. A considerable discrepancy will always exist since it has been modeled explicitly in the statistical model.

The approach followed here to handle this discrepancy related problem is to leave the discrepancy term completely out, in order to be able to calibrate for $\Delta\alpha$ and $\Delta\delta$ and obtain the best fit of the simulations to the observations. Note that the estimates for the calibration parameters will also include model inadequacy errors due to the fact that no model inadequacy discrepancy has been modeled. Therefore, when assessing the calibration results it should be taken into account that the calibrated parameters do not represent physical quantities.

### 9.2.4 Prior and Proposal Distributions

In section 8.3 it has been concluded that even taking into account uncertainties the simulation data do not resemble the observational data. Therefore, the existing uncertainty levels that are used for the uncertainty analysis are unsuitable for a Bayesian prior. The uncertainty estimates in section 7.1 are increased to be included in the prior distributions for the Bayesian calibration.

Normal priors are used for $\Delta\alpha$ and $\Delta\delta$ with

$$\begin{aligned} \Delta\alpha &\sim N\left(0, 1^2\right), \\ \Delta\delta &\sim N\left(0, 1^2\right). \end{aligned}$$

An inverse gamma distribution is used for the prior distribution of the gap width $\Delta g$. The inverse gamma distribution is given by

$$f\left(x; \gamma, \beta\right) = \frac{\beta^{\gamma}}{\Gamma\left(\gamma\right)} \left(x\right)^{-\gamma-1} \exp\left(-\frac{\beta}{x}\right) \tag{9.9}$$

with shape parameter $\gamma$ and scale parameter $\beta$, where $\Gamma\left(\gamma\right) = \left(\gamma - 1\right)!$. There exist closed form expressions for the expectation and variance of the inverse gamma distribution in terms of the shape parameters. Since the mean and variance are convenient in use the shape and scale parameters are expressed as a function of the mean and square root of the variance, which are denoted by $\mu_{IG}$ and $\sigma_{IG}$ respectively. The relationship between the parameters is given by

$$\begin{aligned} \gamma &= \left(\frac{\mu_{IG}}{\sigma_{IG}}\right)^2 + 2, \\ \beta &= \mu_{IG}\left(\left(\frac{\mu_{IG}}{\sigma_{IG}}\right)^2 + 1\right). \end{aligned}$$

Employing these parameters the inverse gamma distribution is formulated as

$$IG\left(\mu_{IG}, \sigma_{IG}\right) = f\left(x; \gamma, \beta\right).$$

Using this formulation of the inverse gamma distribution the gap width is distributed as

$$\Delta g \sim IG\left(0.004, 0.005\right).$$

The proposal distributions for $\Delta\alpha$ and $\Delta\delta$ are independent normal distributions with constant standard deviations. The proposal distribution for the gap width $\Delta g$ is chosen to be an inverse gamma distribution, also with constant $\sigma_{IG}$. The inverse gamma distribution has the advantage of preventing unrealistic negative samples for the gap width. Due to the fact that the kriging surfaces are only made for a certain range of the input variables, the proposal samples are prevented to exceed this range.

### 9.2.5 McMC Simulation on the Posterior Distribution

observational data is available for the lift coefficient and moment coefficient. For each coefficient a different kriging model is obtained. Furthermore, no discrepancy is taken into account for the $C_L$ and $C_M$ data.

The likelihood function of the lift coefficient data reads

$$\begin{aligned} L\left(\boldsymbol{d}_{C_L}|\boldsymbol{\theta}\right) \quad \propto \quad & \left|\boldsymbol{V}_{\boldsymbol{d}_{C_L}}\left(\boldsymbol{\theta}\right)\right|^{-1/2} \left|\boldsymbol{W}\left(\boldsymbol{\theta}\right)\right|^{1/2} \\ & \exp\left\{\left(\boldsymbol{d}_{C_L} - \boldsymbol{H}\left(\boldsymbol{\theta}\right)\boldsymbol{\beta}\right)^T \boldsymbol{V}_{\boldsymbol{d}_{C_L}}\left(\boldsymbol{\theta}\right)^{-1}\left(\boldsymbol{d}_{C_L} - \boldsymbol{H}\left(\boldsymbol{\theta}\right)\boldsymbol{\beta}\right)\right\}, \end{aligned}$$

where $\boldsymbol{H}\left(\boldsymbol{\theta}\right)$ and $\boldsymbol{V}_{\boldsymbol{d}_{C_L}}\left(\boldsymbol{\theta}\right)$ are according to Equations (9.5) and (9.6) respectively. Since the discrepancy term is excluded from the statistical model, no additional regression parameters and hyperparameters need to be estimated. A similar likelihood function is obtained for the moment coefficient data.

The full joint posterior distribution is given by

$$p\left(\boldsymbol{\theta}|\boldsymbol{d}_{C_L}, \boldsymbol{d}_{C_M}\right) \propto L\left(\boldsymbol{d}_{C_L}|\boldsymbol{\theta}\right) L\left(\boldsymbol{d}_{C_M}|\boldsymbol{\theta}\right) p\left(\boldsymbol{\theta}\right), \tag{9.10}$$

where $p\left(\boldsymbol{\theta}\right)$ is the prior distribution on the calibration parameters.

Markov chain Monte Carlo simulation is performed on the joint posterior distribution. The burn in size is determined by investigating the curves of the calibration parameter values in the Markov chain. Convergence is checked by performing various runs with different starting samples and various chain size.

## 9.3 Calibration Results

Before presenting the results of the Bayesian calibration the likelihood functions are examined to provide insight in the relation between observational data and calibration parameters, see section 9.3.1. The actual results for the calibration parameters are presented in section 9.3.2. Finally, in section 9.3.3 the uncalibrated and calibrated simulations are compared with the observations to show the implications of the calibration on the simulations.

### 9.3.1 Features of the Log-likelihood Functions

Investigation of the likelihood functions of the lift and moment coefficients provides information about the estimates of the calibration parameters. Figure 9.1 shows contour graphs of the logarithms of the likelihood functions of $C_L$ and $C_M$ separately and of the sum of both likelihood functions. The maximum values correspond to the best estimate of the calibration parameters. Only the angle of attack discrepancy $\Delta\alpha$ and flap angle discrepancy $\Delta\delta$ are investigated here.

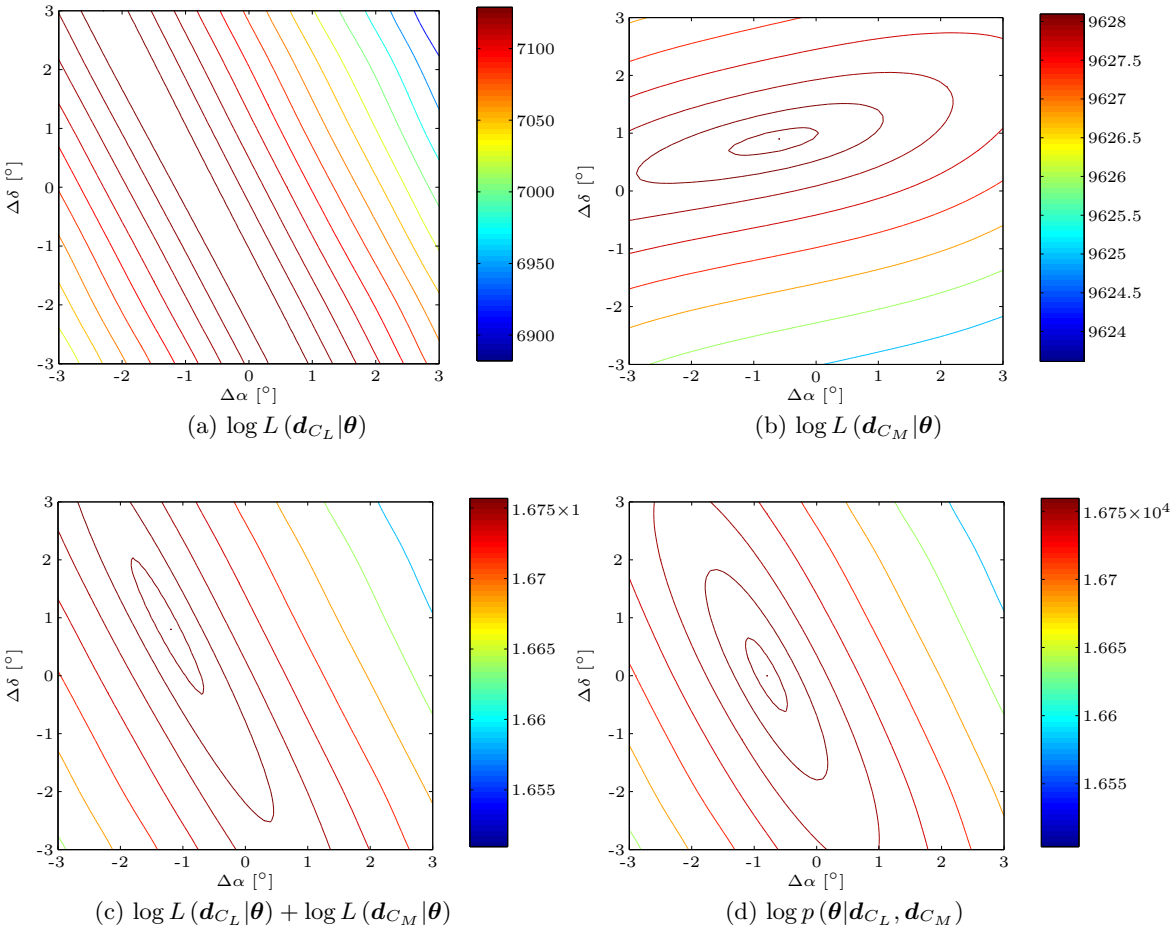


(a) $\log L\left(\boldsymbol{d}_{C_L}|\boldsymbol{\theta}\right)$ (b) $\log L\left(\boldsymbol{d}_{C_M}|\boldsymbol{\theta}\right)$

(c) $\log L\left(\boldsymbol{d}_{C_L}|\boldsymbol{\theta}\right) + \log L\left(\boldsymbol{d}_{C_M}|\boldsymbol{\theta}\right)$ (d) $\log p\left(\boldsymbol{\theta}|\boldsymbol{d}_{C_L}, \boldsymbol{d}_{C_M}\right)$

**Figure 9.1:** Contour plots of the log-likelihood functions versus the angle of attack discrepancy $\Delta\alpha$ and the flap angle discrepancy $\Delta\delta$. The characteristics of the log-likelihood function of the lift coefficient $\log L\left(\boldsymbol{d}_{C_L}|\boldsymbol{\theta}\right)$ are shown separately from the characteristics of the log-likelihood function of the moment coefficient $\log L\left(\boldsymbol{d}_{C_M}|\boldsymbol{\theta}\right)$. Subfigure (c) presents the contour plot of the sum of the log-likelihood functions of $C_L$ and $C_M$ and subfigure (d) the contour plot of the logarithm of the full joint posterior distribution.

Investigating the log-likelihood function of $C_L$ in Figure 9.1a yields the observation that the best estimates of the calibration parameters lie on a line in the $\Delta\alpha - \Delta\delta$ plane, when taking only into account the $C_L$ observational data. The fact that the best estimates lie on a line indicates that the calibration parameters $\Delta\alpha$ and $\Delta\delta$ are interchangeable for the

lift coefficient. The gradient of the line is approximately equal to -2. This corresponds to the conclusion from the sensitivity derivatives that the lift coefficient is twice as sensitive to variations in angle of attack than to variations in flap angle.

The contour plot of the log-likelihood function of $C_M$ shows that the moment coefficient observations do not provide much information about the best estimate for $\Delta\alpha$. This can be concluded from the fact that the major axis of the ellipse is nearly aligned with the $\Delta\alpha$-axis. The moment coefficient observations however provide clear information about the best estimate for $\Delta\delta$.

The contour plot of the sum of log-likelihood functions in Figure 9.1c shows that the joint posterior distribution will be dominated by the lift coefficient observations. This is partly caused by the fact that the discrepancy between simulations and observations for the moment coefficient is clearly more severe than for the lift coefficient. The joint posterior distribution is obtained from adding the prior distribution to the sum of log-likelihood functions.

### 9.3.2 Estimates of the Calibration Parameters

Calibration is performed using the joint posterior distribution, Equation (9.10). Convergence of the McMC simulation is checked by performing multiple runs with various chain size and starting points. A chain size of $10^5$ samples yields converged results for the calibration estimates. The sample mean and the covariance of the chain are computed yielding the calibration results presented in Table 9.1. In this table the standard deviation denotes the square root of the diagonal elements of the covariance matrix of the calibration parameters.

| | Mean | Standard deviation |
|---|---|---|
| $\Delta\alpha$ [°] | -0.84 | 0.42 |
| $\Delta\delta$ [°] | 0.03 | 0.76 |
| $\Delta g$ [mm] | 7.95 | 3.76 |

**Table 9.1:** Calibration estimates for the parameters angle of attack discrepancy $\Delta\alpha$, flap angle discrepancy $\Delta\delta$ and gap width $\Delta g$.

The resulting calibration estimates are the values of the calibration parameters that yield the best fit of the simulations to the observational data, given the error structure of the statistical model. The calibration estimate of the angle of attack discrepancy $\Delta\alpha$ amounts to -0.84 degrees and the uncertainty expressed in the standard deviation amounts to 0.42 degrees. Furthermore, the calibration estimate of the flap angle discrepancy $\Delta\delta$ amounts to 0.03 degrees and the uncertainty amounts to 0.76 degrees.

Notice that the estimates of $\Delta\alpha$ and $\Delta\delta$ deviates from the maximum of the log-likelihood functions visible in Figure 9.1c. This is caused by influence of the prior distributions on the joint posterior distribution. The fact that the standard deviations are rather large is mainly caused by the interchangeability of both parameters for the calibration of the lift coefficient data. Note that the calibration estimate of $\Delta\alpha$ lies outside the estimated input uncertainty range of 0.263 for the angle of attack, see Table 7.1. This is mainly

caused by the fact that the discrepancy between simulations and observational data has not been modeled explicitly by a discrepancy function.

The calibration estimate for the gap width $\Delta g$ amounts to 7.95 mm. It is considerably larger than the prior estimate of 4 mm. Furthermore, after the analysis the gap width is measured manually in the experimental setup and amounts approximately to 2 mm. The difference between the true physical gap width and the calibration estimate originates from the fact that the estimate of the gap width accounts for model inadequacy as well. The large standard deviation is mainly caused by the fact that variations of the lift and moment coefficient due to the gap width are very small for large gap width.

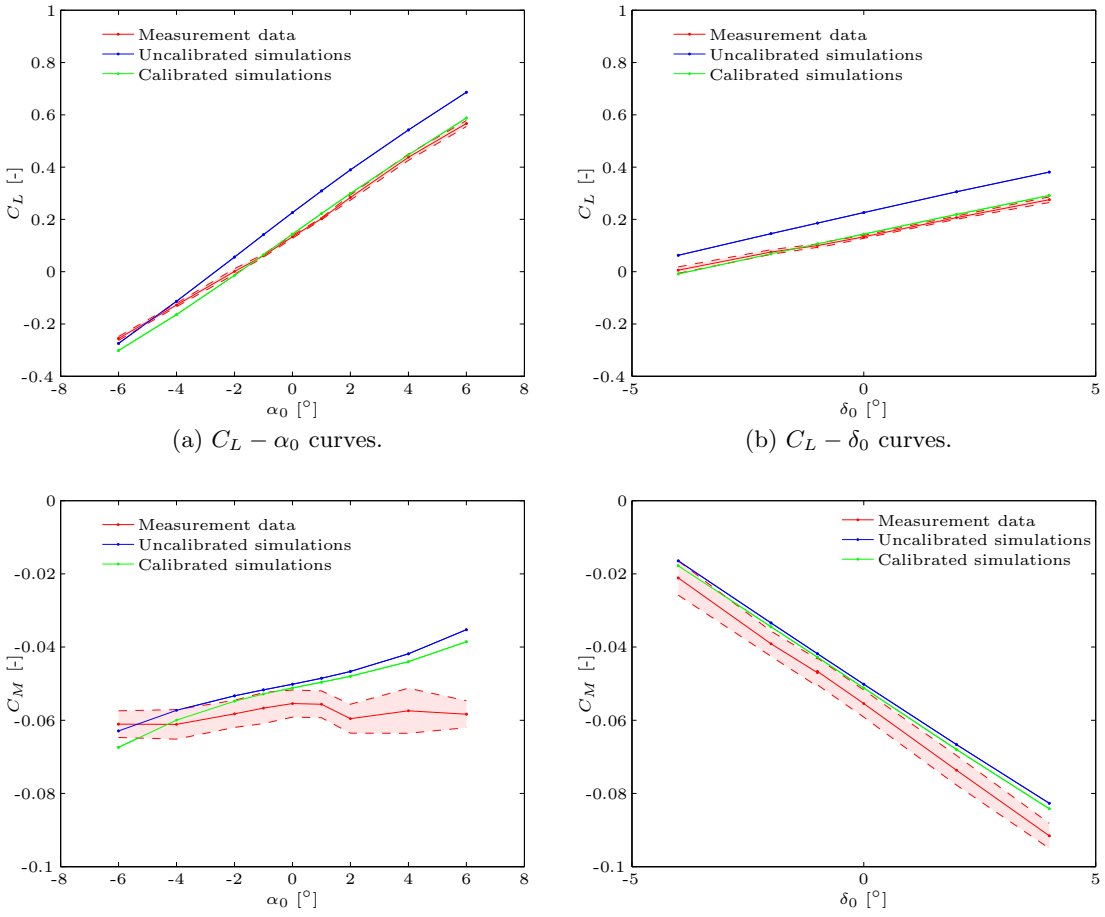


(a) $C_L - \alpha_0$ curves.

(b) $C_L - \delta_0$ curves.

(c) $C_M - \alpha_0$ curves.

(d) $C_M - \delta_0$ curves.

**Figure 9.2:** Simulated lift and moment coefficient data for uncalibrated and calibrated inputs compared with the observational data. The shaded areas indicate a measurement uncertainty of 2 standard deviations.

### 9.3.3 Calibrated Simulations

The effect of the calibrated parameters on the simulations is shown in Figure 9.2. The lift and moment coefficient data are shown as a function of the variable inputs $\alpha_0$ and $\delta_0$. The

calibrated lift coefficient data shows good agreement with the observational data. The agreement in the moment coefficient data is improved, however it is not as good as the agreement in lift coefficient data. This is caused by the fact that the posterior distribution is dominated by the lift coefficient observations, as explained in section 9.3.1. The low influence of the moment coefficient data on the calibration results flows mainly from the fact that the measurement error is relatively large with respect to the data range, see Figures 9.2c and 9.2d. For the lift coefficient the measurement error is small with respect to the data range, therefore the log-likelihood function of the lift coefficient has a sharp maximum.

The correlations between the calibration parameters $\Delta\alpha$ and $\Delta\delta$ can be extracted from Figure 9.2 as well. The interchangeability of both parameters for the lift coefficient data is clearly visible. An increase in either the angles of attack or the flap angles would yield the same agreement of simulation data with the observations. The moment coefficient curves indicate that changing the angles of attack does not especially yield better agreement, whereas changes in the flap angles would yield better agreement.

## 9.4 Prediction of the Drag Coefficient

During the experiment no trustworthy results for the drag coefficient are obtained. Therefore drag coefficient data is obtained from the simulation codes. A kriging surface of the drag coefficient is made in a similar way as the kriging surfaces of the lift and moment coefficient. The kriging surface is based on simulation data from XFOIL where the gap width influence is introduced according to Tornado computations. The simulation data has been corrected for wind tunnel effects and the chord length discrepancy according to section 3.3.

From the multivariate distribution of the calibration parameters, $10^4$ samples are generated. The drag coefficient is computed for each input sample using the kriging surface. The sample mean and standard deviation are computed for the collection of all drag coefficient samples. This procedure is performed for each experimental data point yielding the $C_D - \alpha$ and $C_D - \delta$ curves shown in Figure 9.3.

The standard deviation varies with angle of attack and flap angle. The minimum in the $C_D - \alpha$ curve is predicted at $\alpha \approx -2$. Figure 9.3b shows that the flap deflection angle is less influential for the drag coefficient than the angle of attack. This is partly caused by the fact that the lift coefficient, and thereby the induced drag, is less sensitive to the flap angle than to the angle of attack. Furthermore, the angle of attack is more influential for the front area of the wing that influences the pressure drag. Also the transition location and thereby the skin friction are sensitive to the angle of attack, and less sensitive to the flap angle.

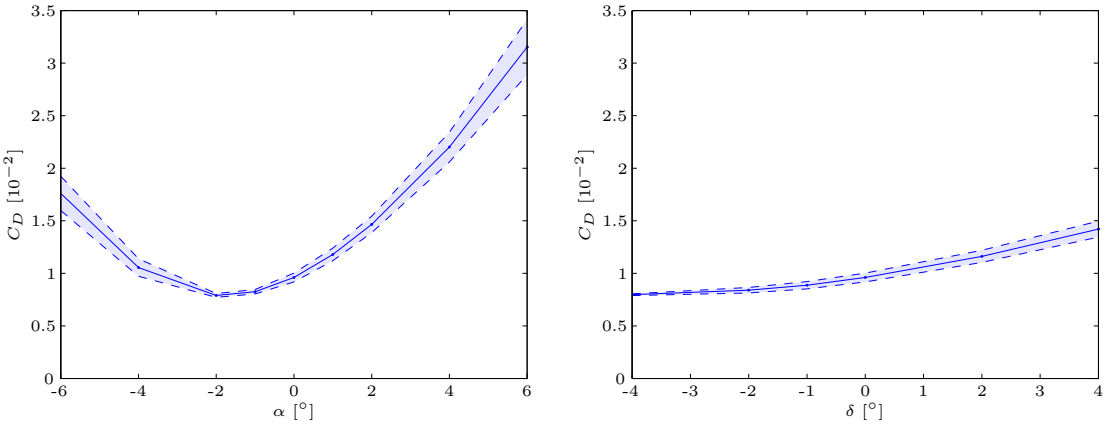


(a) $C_D - \alpha$ curve.

(b) $C_D - \delta$ curve.

**Figure 9.3:** Predictions of drag coefficient data for the calibrated input parameters. The shaded areas correspond to uncertainty intervals of one standard deviation.

# Chapter 10

# Conclusions and Recommendations

This chapter summarizes the most important conclusions of this thesis and presents recommendations for future research.

## 10.1 Conclusions

The fluid-structure interaction experiment in this thesis was meant to provide two-dimensional data ideally. Three-dimensional features are tried to be excluded using side walls. However, investigating the influence of the gap width on the lift coefficient yields the observation that a small increase in gap width from 0 to 10 mm reduces the lift coefficient considerably.

An accurate geometric model is obtained by applying cokriging to CMM measurements and photogrammetry measurements of the wing geometry. The investigation of the wing geometry has revealed that geometric deviations from the design airfoil DU96W180 are mainly present in the middle chord region and the flap region. The measured wing geometry is approximated by deforming the design airfoil using a Free Form Deformation parameterization. Sensitivity analysis of the FFD parameters has revealed that the lift coefficient is most sensitive to geometric changes in the flap region. Combining the geometric uncertainty information with the sensitivity derivatives yields the result that the most important FFD parameters are the ones located near the trailing edge. The importance of the parameters decreases when moving forward towards the leading edge.

The influence on the lift coefficient of the uncertain parameters angle of attack, flap angle, free stream velocity and gap width has been investigated. The sensitivity derivatives of the parameters show that the lift coefficient is twice as sensitive to variations in the angle of attack than to variations in the flap angle. Furthermore, the sensitivity derivative of the gap width is very high due to the fact that increasing the gap width from 0 to 10 mm induces a considerable decrease in lift coefficient due to the emergence of tip vortices. From the scaled sensitivity derivatives it can be concluded that the flap angle is the most

important input variable, followed by the angle of attack. The gap width and the free stream velocity are relatively unimportant.

The most important uncertain input variables are used for the uncertainty analysis. The uncertainty of the lift coefficient and moment coefficient due to input uncertainties is quantified using a probabilistic collocation approximation of XFOIL simulations and a kriging surrogate of Tornado simulations. Large discrepancies between the simulations and observations indicate that the model does not represent the observations given the uncertainties and measurement errors. The disagreement between simulations model and observations is believed to be mainly caused by model inadequacy errors, which have not been taken into account in the uncertainty analysis.

The uncertainty analysis results show clearly the presence of discrepancies between simulations and observations. These discrepancies are partly caused by systematic uncertainties in the input parameters. Bayesian calibration is performed to estimate the constant offset in angle of attack and flap angle due to systematic uncertainties. Furthermore, the gap width is included as a calibration parameter as well because it has not been measured during the experiment. The resulting calibration estimates yield a good fit of the lift coefficient simulations to the observations. Due to the fact that the measurement error of the moment coefficient observations is large with respect to the data range the calibrated moment coefficient simulations show less agreement with the observations. Due to the fact that the discrepancy between simulations and observations due to model inadequacy has not been taken into account, the calibration estimates account for model inadequacy errors as well as input parametric uncertainties.

Combining the uncertainty characteristics with the observational data yields the required inputs for the validation of computer codes. Validation using the predicted drag coefficient will be problematic due to the discrepancy introduced by model inadequacy.

## 10.2 Recommendations

The recommendations for future research that are discussed here are related to the experiment and various parts of the uncertainty quantification.

Regarding the experiment several improvements are proposed to reduce uncertainties. Since only a small gap width is sufficient for the development of wing tip vortices, it might be beneficial to attach side plates to the wing ends. This prevents the formation of wing tip vortices and makes the flow two-dimensional. The uncertain wing geometry has proven to be one of the major causes of output uncertainties. Therefore care must be taken when manufacturing the wing. Reduction of the uncertainties in the angle of attack and flap angle can be achieved by making a new mold based on the geometric model that is obtained in this thesis. These measures are likely to reduce the uncertainty of the observations.

The determination of the control weight distribution is performed using a simple least squares approach. Results can possibly be improved by employing Bayesian regression or Bayesian calibration techniques. Furthermore three-dimensional computations on the cokriging wing model can yield improved estimates with respect to the two-dimensional computations. Since XFOIL can only perform two-dimensional computations in this

thesis the three-dimensional wing is transformed into a two-dimensional profile adding the variation in the span wise direction as uncertainty on the two-dimensional profile. This is a simplification that adds uncertainty to the computations, which can be avoided by performing three-dimensional computations.

The results of the sensitivity analysis and uncertainty analysis can be improved by using more accurate simulation codes. The choice for the codes employed in this thesis was mainly based on the requirement of low computation time. Combining many runs of the cheap codes with few runs of accurate and expensive CFD codes using cokriging improves the accuracy. This can reduce the discrepancy due to model inadequacy and can yield improved uncertainty estimates.

Improved estimates of the uncertain input parameters can be obtained by introducing changes in the Bayesian calibration approach. Generating more observational data, for example at different Mach numbers, would enable to model the discrepancy due to model inadequacy. This would greatly improve the calibration estimates. In case it is impossible to generate more observational data it might be possible to model the discrepancy due to model inadequacy outside the calibration procedure by assuming an analytic discrepancy function on the simulation data. This analytic expression should be based on expert knowledge about the performance of the simulation codes and the discrepancies that exist between the codes and other experiments.

The angle of attack discrepancy and flap angle discrepancy are intrinsic parameters in the angle of attack and flap angle. This enables to apply kriging to lift coefficient data as a function of only three variables, the angle of attack, the flap angle and the gap width. Calibration on a kriging surface of only three variables instead of a kriging surface of five variables will requires less computational efforts. It is recommended to investigate possibilities to improve on the Bayesian calibration method when calibration parameters are in fact intrinsic in the variable inputs.

It is recommended to improve on the prediction of the drag coefficient by including accurate simulations of expensive codes. Cokriging provides excellent possibilities to combine the low fidelity data with few accurate simulations.

# References


Boon, D. J. (2011). *Data Assimilation of a Fluid-Structure Interaction Problem - Literature Review Report.* Delft University of Technology.

Brooks, T. F., Marcolini, M. A., & Pope, D. S. (1984, October). *Airfoil Trailing Edge Flow Measurements and Comparison with Theory Incorporating Open Wind tunnel Corrections* (No. AIAA-84-2266). AIAA/NASA 9th Aeroacoustic Conference.

Chassaing, J. C., & Lucor, D. (2010). Stochastic Investigation of Flows About Airfoils at Transonic Speeds. *AIAA Journal*, *Vol.128*, pp. 1852 – 1867.

Drela, M. (2011, September 2). *XFOIL homepage.* http://web.mit.edu/drela/Public/web/xfoil/.

Duvigneau, R. (2006, July). *Adaptive Parametrization using Free-From Deformation for Aerodynamic Shape Optimization* (No. INRIA RR5949). Unit de recherche INRIA Sophia Antipolis.

Forrester, A. I. J., Sóbester, A., & Keane, A. J. (2007). Multi-fidelity optimization via surrogate modelling. *Proceedings of the Royal Society A*, *Vol.463*, pp. 3251 – 3269.

Golub, G. H., & Welsch, J. H. (1969). Calculation of Gauss Quadrature Rules. *Mathematics of Computation*, *Vol.23(106)*, pp. 221 – 230.

Hastings, W. K. (1970). Monte Carlo sampling methods using Markov chains and their applications. *Biometrika*, *Vol.57*, pp. 97 – 109.

Kennedy, M. C., & O'Hagan, A. (2000). Predicting the output from a complex computer code when fast approximations are available. *Biometrika*, *Vol.87*, pp. 1 – 13.

Kennedy, M. C., & O'Hagan, A. (2001a). Bayesian calibration of computer models. *Journal of the Royal Statistical Society B*, *Vol.63*, pp. 425 – 464.

Kennedy, M. C., & O'Hagan, A. (2001b). *Supplementary details on Bayesian Calibration of Computer Models* (No. Internal report). University of Sheffield.

Liang, F., Liu, C., & Carroll, R. J. (2010). *Advanced Markov Chain Monte Carlo Methods: learning from past samples*. Chichester, West Sussex, UK: John Wiley & Sons Ltd.

Loeven, G. J. A. (2010). *Efficient uncertainty quantification in computational fluid dynamics*. Ph.D. Thesis, Delft University of Technology, Delft, The Netherlands.

Loeven, G. J. A., & Bijl, H. (2008). Probabilistic Collocation used in a Two-Step approach for efficient uncertainty quantification in computational fluid dynamics. *Computer Modeling in Engineering & Science*, *Vol.36*, pp. 193 – 121.

Melin, T. (2000). *A Vortex Lattice MATLAB Implementation for Linear Aerodynamic Wing Applications*. MSc. Thesis, Royal Institute of Technology (KTH), Stockholm, Sweden.

Metropolis, N., RosenBluth, A. W., Rosenbluth, M. N., Teller, A. H., & Teller, E. (1953). Equations of state calculations by fast computing machine. *Journal of Chemical Physics*, *Vol.21*, pp. 1087 – 1091.

Pearson, K. (1901). On Lines and Planes of Closest Fit to Systems of Points in Space. *Philosophical Magazine*, *Vol.2(6)*, pp. 559 – 572.

Sederberg, T. W., & Parry, S. R. (1986, August). Free-form deformation of solid geometric models. In *Proceedings of the 13th annual conference on computer graphics and interactive techniques* (Vol. 20, pp. 151–160). New York, NY, USA.

Wang, S., Chen, W., & Tsui, K. L. (2009). Bayesian Validation of Computer Models. *Technometrics*, *Vol.51*, pp. 439 – 451.

Wikle, C. K., & Berliner, L. M. (2006). A Bayesian tutorial for data assimilation. *Physica D*, *Vol.230*, pp. 1 – 16.